Aqueous Electrochemical CO_2 Reduction on Copper-based Catalysts in Flow Cell System



Yifei Wang

Inorganic Chemistry Laboratory, Department of Chemistry

New College

A thesis submitted for the degree of

Doctor of Philosophy in Inorganic Chemistry

Trinity 2023

Table of Contents

Table of Contents.....i
Declaration.....iv
Acknowledgements.....v
Abstract.....vii
List of Abbreviations.....viii
List of Publications and Conferences.....x
Chapter 1 Introduction.....1
1.1 Motivation.....1
1.2 Electrochemical CO_2 Reduction.....2
1.2.1 Reaction Conditions.....3
1.2.2 C_1 Products and Mechanisms.....6
1.2.3 C_{2+} Products and Mechanisms.....8
1.2.4 Selectivity and Faradaic Efficiency.....10
1.3 Development of ECR Catalysts.....11
1.3.1 Non-copper Electrocatalysts: towards CO and $HCOOH/HCOO^-$.....11
1.3.2 Copper-based Electrocatalysts.....15
1.4 Electrolysers Configuration of ECR.....20
1.4.1 H-cell.....21
1.4.2 Liquid-phase Flow Cell.....22
1.4.3 Membrane Electrode Assembly (MEA).....25
1.4.4 Ion-exchange Membranes.....26
1.5 Aims and Objectives.....30
1.6 Thesis Overview.....31
1.7 References.....32
Chapter 2 Characterisation Techniques and Experimental Methods.....44
2.1 Introduction.....44
2.2 Characterisation Techniques.....44
2.2.1 X-ray Diffraction.....44
2.2.2 Transmission Electron Microscopy.....46
2.2.3 X-ray Absorption Spectroscopy.....48
2.2.4 Raman Spectroscopy.....50
2.2.5 Electrochemical Techniques.....51
2.2.6 Gas Chromatography.....56

2.2.7 Mass Spectrometry....56
2.2.8 X-ray Photoelectron Spectroscopy....58
2.3 Experimental Methods....59
2.3.1 Chemicals....59
2.3.2 Synthesis of Single-layer MoS_2 and Cu Exchange....59
2.3.3 Preparation of $Mg(OH)_2$ Substrates....60
2.3.4 Cu loading on $MgO/Mg(OH)_2$ Substrates....61
2.3.5 Synthesis of Cu Nanoparticles....61
2.3.6 Synthesis of CuO_x....62
2.3.7 Synthesis of CuPd Nanoparticles....62
2.3.8 Electrode Fabrication Process....63
2.3.9 Electrochemical Measurements....63
2.3.10 EIS Measurements....64
2.3.11 Calculations of Faradaic Efficiency....64
2.3.12 XRD Measurements....65
2.3.13 SEM Measurements....65
2.3.14 TEM Measurements....65
2.3.15 XPS measurements....66
2.3.16 *In-situ* Raman Measurements....66
2.3.17 XAS Measurements....67
2.3.18 Operando PTR-TOF-MS Measurements....67
2.4 Reference....68
Chapter 3 Cu on Proton-conductive Supports for Methane Production....72
3.1 Introduction....72
3.2 Results and Discussion....74
3.2.1 Cu on supports in PEM Electrolyser....74
3.2.1.1 Cu on few-layer MoS_2....74
3.2.1.2 Cu on $Mg(OH)_2$ support....77
3.2.2 Cu on $Mg(OH)_2$ support in AEM-MEA Electrolyser....80
3.2.3 Cu on MgO support in AEM flow cell....82
3.2.4 EPR of Copper on MgO Supports....86
3.2.5 *In-situ* Raman Spectroscopy....87
3.2.6 *In-situ* XAS Studies....89
3.3 Conclusion....92
3.4 References....92
Chapter 4 Behaviours of Cu Nanoparticles in Alkaline and Neutral Electrolytes....97
4.1. Introduction....97

4.2. Results and Discussion.....99
4.2.1. XRD.....99
4.2.2. TEM.....101
4.2.3. Electrode Morphologies.....103
4.2.4. ECR Performance.....103
4.2.5. EIS Scans.....104
4.2.6. Cu Coordination Environment.....108
4.3. Conclusion.....110
4.4. References.....111
Chapter 5 Ethylene Production in Neutral Electrolyte on Pd-doped Cu.....115
5.1 Introduction.....115
5.2 Results and Discussion.....117
5.2.1 CuPd Catalysts Properties.....117
5.2.1.1 TEM.....117
5.2.1.2 XRD.....118
5.2.1.3 XPS.....119
5.2.2 Electrochemical Performance.....121
5.2.3 EIS Studies.....122
5.2.4 XAS.....125
5.2.4.1 *Ex-situ* XAS on GDE.....125
5.2.4.2 *In-situ* XAS in Neutral Electrolyte.....128
5.2.5 Operando PTR-TOF-MS.....132
5.3 Conclusion.....137
5.4 Reference.....138
Chapter 6 Conclusions and Outlook.....143
6.1 Conclusions.....143
6.2 Outlook.....146
6.3 Reference.....147
Appendix.....149
I. Appendix Tables.....149
II. Appendix Figures.....150
III. Reference.....155

Declaration

All research works reported in this thesis have not previously been accepted in substance for any degree and is not being concurrently submitted in candidature for any degree. This thesis is conducted by the author unless stated otherwise. All materials from other sources have been properly and fully acknowledged.

Yifei Wang

Acknowledgements

First and foremost, I would like to express my gratitude to my supervisor Professor Edman Tsang for giving me the opportunity to work in his group over the last four years and the freedom of choosing research topics based on my own interest. I would also like to thank him and the China Scholarship Council-PAG Oxford Scholarship for the funding that allowed me to accomplish my DPhil projects and write up this thesis.

The research presented in this thesis would not have been possible without the assistance I received from all members of the Tsang group. The kind and inclusive atmosphere made it a joy to work in this lab. Particularly, I would like to thank Dr. Tuğçe Ayvalı, Dr. Pu Zhao and Prof. Jianwei Zheng for their support at the beginning of my DPhil project. In addition, many thanks are given to Prof. Huihuang Fang and Dr. Tianyi Chen for their friendship that lit up my days during the gloomy COVID-19 lockdowns.

Throughout my DPhil studies, I have received numerous supports from the Tsang group, research collaborators and administrative staffs from the Department of Chemistry. Therefore, I would like to express my appreciation to:

Dr. Hangjuan Ren, Xuelei Pan and Dr. Jiaying Mo for their support and insightful discussions on electrochemistry;

Dr. Xiaojie She and Prof. Shu-Ping Lau (Hong Kong Polytechnic University) for their professional discussions and advice on MEA cell setup;

Dr. Tuğçe Ayvalı and Prof. Jianwei Zheng for their assistance on GC setup;

Dr. Tai-sing Wu (NSRRC Taiwan), Xuelei Pan, Wentian Niu and Bryan Ng for acquiring XAS data and assistance on data analysis;

Dr. Tianyi Chen, Baron Ho, Yi Yuang, Prof. Alex W Robertson (Oxford Materials) and Prof. Huihuang Fang (Fuzhou University) for acquiring TEM and SEM images;

Dr. Shaoliang Guan (HarwellXPS) and Wentian Niu for acquiring XPS data and assistance on analysis;

Prof. Yunlong Zhao, Dr. Manman Wang, Dr. Stephen Downes (Surrey University) and Xuelei Pan for *in-situ* Raman measurements and advice on data analysis;

Dr. William Myers, Dr. Yiyang Li and Wentian Niu on EPR spectroscopy;

Dr. Crina Corbos, Dr. Sauravchandra Sarma (Johnson Matthey), Dr. Baran Sahin (Siemens Energy) and Dr. Filippi Michael (Technische Universität Berlin) for the insightful discussions in Ecofuel meetings.

I would also like to thank the examiners of my DPhil viva, Prof. Richard Compton and Prof. Frank Marken, for the inspiring questions and fruitful discussions.

Finally, my deepest gratitude is given to my parents and all my family members for their love and support that help me overcome those difficulties. Most importantly, I need to thank Wentian for your continual encouragement, patience, and unwavering love, who has made my time in Oxford worth treasuring.

Abstract

Carbon dioxide emission has exacerbated over the years ever since the usage of fossil fuels in human society. Development of electrochemistry can enable a green conversion of CO_2 into valuable chemicals such as methane and ethylene under mild conditions. Electrocatalysts and electrolysers are likely to be the keys to achieve the process more efficiently to fulfil the zero-emission goal.

Under such context, this thesis explores various copper-based materials targeting at hydrocarbons. Modifications on the surface and interface of the Cu catalysts are made, and in-depth catalytical performance is studied to illustrate its response to potentials and current. A Cu/MgO supported catalyst was found to be selective to methane up to 50%. Relations between the selectivity and structure are obtained through surface characterisations and spectroscopies. *In-situ* characterisations were also conducted to understand the structural evolution during the electrochemical reactions.

Meanwhile, influence from the electrolytes was demonstrated on a model Cu GDE. A sharp contrast on the products distribution was shown with the alkaline solution favouring ethylene and the neutral one methane. A Pd-doped Cu catalyst was then developed to alleviate the need of high pH environment essential for ethylene production, and a comparable efficiency was achieved under neutral electrolyte. Comprehensive studies on the electrodes were carried including EIS and PTR-TOF-MS which revealed that C-C coupling is not the rate-determine step of CO_2-to-C_{2+} conversion. Introducing an exotic element to copper was, therefore, proved to be an effective strategy to alter the preference to the adsorption of carbon intermediates.

List of Abbreviations

AEM	Anion Exchange Membrane
AI	Artificial Intelligence
BID	Dielectric-Barrier Discharge Ionization Detector
BPM	Bipolar Membrane
CB	Carbon Black
CE	Counter Electrode
CEM	Cation Exchange Membrane
CN	Coordination Number
CPE	Constant Phase Element
CV	Cyclic Voltammetry
DFT	Density Functional Theory
DI	Deionised
ECR	Electrochemical CO_2 Reduction
EDX	Energy-dispersive X-ray Spectroscopy
EI	Electron Ioniser
EIS	Electrochemical Impedance Spectroscopy
EXAFS	Extended X-ray Absorption Fine Structure
FE	Faradaic Efficiency
FID	Flame Ionization Detector
GC	Gas Chromatography
GDE	Gas Diffusion Electrode
HER	Hydrogen Evolution Reaction
LSV	Linear Sweep Voltammetry
MEA	Membrane Electrode Assembly

MFC	Mass Flow Controller
MS	Mass Spectroscopy
n-BuLi	*n*-Butyllithium
NP	Nanoparticle
OA	Oleylamine
OCP	Open Circuit Potential
PEM	Proton Exchange Membrane
PSE	Porous Solid Electrolyte
PTFE	Polytetrafluoroethylene
PTR	Proton Transfer Reaction
RE	Reference Electrode
RDS	Rate Determine Step
SAC	Single-atom Catalysts
SEM	Scanning Electron Microscope
SOEC	Solid Oxide Electrolyser Cell
SHE	Standard Hydrogen Electrode
TCD	Thermal Conductivity Detector
TEM	Transmission Electron Microscopy
TOF	Time-of-Flight
V_O	Oxygen Vacancy
WE	Working Electrode
XANES	X-ray Absorption Near-edge Structure
XAS	X-ray Absorption Spectroscopy
XPS	X-ray Photoelectron Spectroscopy
XRD	X-ray Diffraction
Z	Impedance

List of Publications and Conferences

1. Yifei Wang, Xuelei Pan, Shik Chi Edman Tsang MgO Support with Cu for Methane Production from Electrochemical CO_2 Reduction, *In preparation.*

2. Yifei Wang, Hangjuan Ren, Xuelei Pan, Wentian Niu, Shik Chi Edman Tsang Altering selectivities of electrochemical CO_2 reduction in neutral electrolyte, *In preparation*.

3. She Xiaojie, Lingling Zhai, Yifei Wang *et al.*, (2023) Pure-water-fed Electrocatalytic CO_2 Reduction to C_2H_4 beyond 1000 h Stability at 10 A, ***Nat. Energy*** *Accepted*. (co-first author)

4. She Xiaojie, Yifei Wang *et al.*, (2022) Challenges and Opportunities of Electrocatalytic CO_2 Reduction to Chemicals and Fuels, ***Angew. Chem.*** 134, e202211396. (*Review*)

5. Oral Presentation**,** Electrochemical CO_2 reduction with MgO support for methane production. Spring Meeting of the European Materials Research Society (**E-MRS**) May. 2023. (*Conference*)

Chapter 1 Introduction

1.1 Motivation

Carbon dioxide (CO_2) is one of the primary greenhouse gases that contribute to global warming and climate change. In recent years, there has been a growing global consensus on the need to reduce carbon emissions to mitigate the impacts of greenhouse gas emission. Policies and regulations have been implemented to achieve this goal including carbon pricing and energy efficiency standards. For example, in Canada and France, the carbon tax in 2022 reached \$50 t^{-1} CO_2 and €90 t^{-1} CO_2, respectively[1, 2]. The European Union has committed to achieving net-zero greenhouse gas emission by 2050[3], and China has set a target to reach peak carbon emission by 2030 and carbon neutrality by 2060[4].

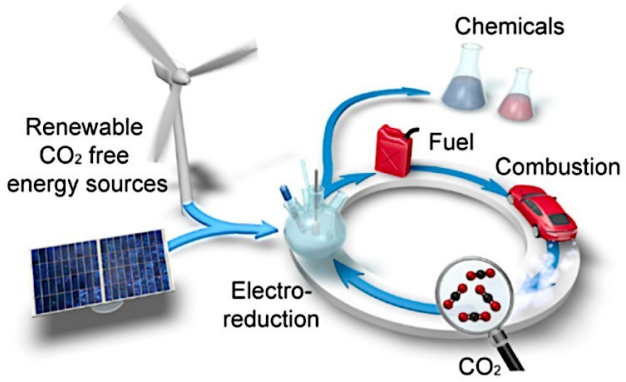


Figure 1.1 An illustration of carbon cycle with electrochemical reactions driven by renewable energy. Reprinted with permission from reference[5]. Copyright 2014 American Chemical Society.

As a chemistry researcher, one could hardly find a better way to contribute to building a low-carbon society by converting CO_2 into value-added products via an energy-effective route. Electrochemical reduction of CO_2 (ECR) technology targets at producing high-value chemicals and fuels such as syngas (CO and H_2 mixture), methane (CH_4), and ethylene (C_2H_4)[6]. It could meet the needs of zero carbon emissions when powered by

electricity generated from solar and wind (**Fig. 1.1**). In light of this, the priority is to understand the reaction mechanism and develop electrocatalysts/electrolysers according to target products.

However, limitation exists in the fundamental research of designing ECR catalysts and electrolysers. The applying of deep reducing potentials gradually deteriorates the electrode and results in the blockage of electrode surface by liquid layers, also known as flooding[7]. The adsorption of CO_2 by the aqueous solution and formation of carbonates could cause the unstable operational voltage and fast increasing of unwanted H_2 production from water splitting[8]. Phase changing of catalytic materials during the reduction reactions is one of the reasons that usually lead to deactivation and decrement of efficiency[9-11]. There are core issues related to the application of ECR at a larger scale, which will be elaborated further in section 1.2 and 1.4.

The solutions to short lifetime and low efficiency of ECR are not only limited by the rational design of catalysts but also involve the analysis of real application scene. For carbon monoxide (CO)[12-14] and formic acid (HCOOH)[15, 16] production, the selectivity and efficiency are well-optimized in the laboratory up to nearly 100% and the focusing should be changed to the electrolyser stacks and elongation of stability, whereas for multi-carbon molecules (C_{2+})[17, 18], the efficiency improvement worth further studying and digging into.

In this thesis, the development of ECR catalysts targeting at methane and ethylene production will be demonstrated. The thesis is not only confined to the engineering of novel materials and advanced characterisation methods but will also include the optimization of electrolyte environment and electrolysers that are closely related to industrial requirements. Therefore, a comprehensive understanding of ECR to fuels will assist its potential application in the industry.

1.2 Electrochemical CO_2 Reduction

Carbon dioxide (CO_2) molecule is chemically inert and hardly participates in reactions unless under harsh conditions including elevated temperatures and pressures. Driven by electricity, the only energy input into an ECR system, it becomes possible to produce chemicals from CO_2 for industry including fuels or raw materials with the assistance of appropriate electrocatalysts. The common products of ECR are usually carbon monoxide (CO), formic acid (HCOOH), methane (CH_4), ethylene (C_2H_4) and ethanol (C_2H_5OH).

1.2.1 Reaction Conditions

Compared to the traditional heterogeneous catalysis of CO_2 hydrogenation, ECR has its intrinsic advantages, one of which is the compatibility with electrical output of renewable energy including solar and wind power, as shown in **Fig. 1.1**. This results from the properties of electrolysis in which the reactions take place on the electrodes and electrolyte interface. Instead of a solid-gas interface, the electrolysis of CO_2 happens on the three-phase interface which consists of electrolyte (liquid), electrocatalysts (solid) and reactant CO_2 (gas)[19]. However, a more complicated reaction interface raises a higher demand on reactor design which will be introduced in section 1.4.

The temperature required for ECR is usually lower than 80 °C. Unlike heterogeneous catalysis, a raise in the reaction temperature causes severe issues to an ECR system. The electrolyte, usually an aqueous solution, will evaporate drastically resulting in high vapor pressure in the gas flow[20] and the precipitation of carbonates on the electrode and membrane. And the membrane for ion-exchanging will suffer from reduced mechanical strengthen leading to a shorter cell operation lifetime[21] or even worse, short circuit of the cell.

The pressure of ECR electrolysers is close to atmospheric pressure which requires fine control particularly in a flow cell. To allow the reaction proceeding on a three-phase interface, the pressure in the system needs to be balanced in each reaction chamber separated by the membrane and electrode. A higher pressure worsens the electrode contact with the electrolyte causing an increased potential or higher resistance; and a lower pressure leads to the flooding of electrolyte onto the electrode surface cutting off the supply of reactant CO_2.

The potential applied to the cell is one of the most important conditions when operating an ECR electrolyser. Hydrogen evolution reaction (HER) from water splitting is the reaction that happens simultaneously on the electrode as ECR takes place. HER is usually believed to be the side reaction of ECR, since the production of hydrogen from proton is consuming the electrons that could have been used to reduce CO_2. Rather than being treated as a side reaction, HER provides activated protons, thus avoiding the direct transport and consumption of high purity hydrogen gas supply[22]. Competitions between HER and ECR are reflected on the similar standard electrode potentials (**Eq. 1.1-1.7**). The theoretical reduction potential difference between hydrogen production from protons and carbon products (CO, HCOOH, CH_4, C_2H_4 and C_2H_5OH) from CO_2 is less than 300 mV[23]. This is a relatively small value compared to the overpotentials of most CO_2 reduction reactions, especially for C_2 products (larger than 500 mV). Therefore, the selectivity of ECR in terms of thermodynamics is a challenge to deal with. Moreover, CO_2 reduction requires a large amount of energy to activate the molecule[24] (**Eq. 1.8**) from linear to bent radical anion to trigger the reaction[25]. It is always challenging to convert inert molecules such as CO_2 into desired products.

$$2H^+ + 2e^- \rightarrow H_2 \qquad E° = -0.42\ V^a \qquad \textbf{(Equation 1.1)}$$

$$CO_2 + 2H^+ + 2e^- \rightarrow CO + H_2O \qquad E° = -0.52\ V \qquad \textbf{(Equation 1.2)}$$

$$CO_2 + 2H^+ + 2e^- \rightarrow HCOOH \quad E° = -0.61\ V \quad \textbf{(Equation 1.3)}$$

$$CO_2 + 4H^+ + 4e^- \rightarrow HCHO + H_2O \quad E° = -0.48\ V \quad \textbf{(Equation 1.4)}$$

$$CO_2 + 8H^+ + 8e^- \rightarrow CH_4 + 2H_2O \quad E° = -0.24\ V \quad \textbf{(Equation 1.5)}$$

$$2CO_2 + 12H^+ + 12e^- \rightarrow C_2H_4 + 4H_2O \quad E° = -0.34\ V \quad \textbf{(Equation 1.6)}$$

$$2CO_2 + 12H^+ + 12e^- \rightarrow C_2H_5OH + 3H_2O \quad E° = -0.33\ V \quad \textbf{(Equation 1.7)}$$

$$CO_2 + e^- \rightarrow CO_2^{\bullet -} \quad E° = -1.90\ V^{b} \quad \textbf{(Equation 1.8)}$$

[a] Values of E° in equation 1 to 6 are referred to standard hydrogen electrode (SHE) in an aqueous solution (pH=7) with electrolyte concentration as 1 mol, at room temperature (25 °C) and 1 atm.

[b] Value measured in a dimethylformamide solution versus SHE.

Influence of pH should be considered in two aspects: the bulk pH of electrolyte and the local pH near the electrode surface. As ECR taking place, protons are consumed leading to a higher pH at the electrode-interface than the bulk. Gradient of pH, therefore, exists near the electrode surface. The thickness of diffusion layer is affected by the current density on the electrode (the consumption rate of protons) as well as the properties of bulk electrolyte. For instance, a switch from neutral electrolyte to alkaline electrolyte increases the pH and suppress the selectivity of CH_4 and H_2, as both involve proton transfer step(s) which are pH dependent[26, 27]. Interestingly, with a high pH electrolyte such as KOH, the OH^- concentration should have been sufficient to maintain a high pH near the interface, yet it was found that the reaction between CO_2 and KOH consumed a large amount of OH^- ions resulting in a near-neutral pH at the electrode surface[28]. Localised surface environment is, therefore, playing a vital role in activating CO_2 and the following charge transfer steps. The applying of catalysts with defects (oxygen vacancies, steps, doping, *etc.*) could increase the binding energy of *CO which benefits C-C coupling[29] and an alkaline environment with highly concentrated hydroxide ions (up to 10 M KOH) is

believed to assist the formation of hydrocarbons by supressing the HER. Charge imbalance between carbon atoms could be increased in the *OCCO intermediates according to density functional theory (DFT) calculations and lower the energy barrier of C-C coupling with condensed OH^- ions[30]. The efficiency of C_{2+} in alkaline conditions could, therefore, be boosted to around 80% as reported in some recent publications[31-36].

1.2.2 C_1 Products and Mechanisms

Since ECR is a complicated reaction that involves multiple steps to reach the final products, it would be easier to study the mechanism from the relatively simple C_1 products. In this section, 2-electron (2e) transferring reactions to CO and $HCOOH/HCOO^-$ will be first introduced followed by the multiple-protonation reactions to CH_4 and CH_3OH.

Production of $HCOOH/HCOO^-$ is a one-step protonation of CO_2 molecules. Like the HER that can be divided into the Volmer-Tafel and Volmer-Heyrovsky mechanisms[37], there are two possible pathways for the ECR to HCOOH reaction. Considering the kinetically unfavoured CO_2 activation step, it is believed that the ECR begins only when the CO_2 is bent and chemically adsorbed onto the catalyst surface forming with either the O-binding (C^*O_2, where * represents the adsorption site) or C-binding ($^*CO_2$) intermediates. The next protonation step (**Fig. 1.2a**) could take place with the either proton abstracted to a surface site like the Tafel step in HER, or the solvated proton like the Heyrovsky step. The final intermediate *OCHO or *COOH might seem plausible for further protonation steps, but there will not be any related products in an ECR system. It has been calculated that the protonation of *OCHO to $^*OCH_2O$ has an extremely high energy barrier up to 1.6eV that is almost impossible to overcome[38].

The formation of CO has a clearer route and more solid evidence from the spectroscopy. The adsorbate generated after the deoxygenation of CO_2 is one of the most studied *CO intermediates (**Fig. 1.2b**, dashed box). CO is formed when this key intermediate desorbed from the surface immediately without any further protonation steps. From Raman spectra, the adsorption of *CO on Cu surface is observed usually at 276-290 cm^{-1} for Cu-CO rotation and 354-370 cm^{-1} for Cu-CO stretching. And the C=O bond stretching of *CO could be identified at around 2000 cm^{-1}. These experimental results reflect that *CO has higher coverage and is easier to be observed during the ECR, which gives clues that *CO is the key intermediates[39].

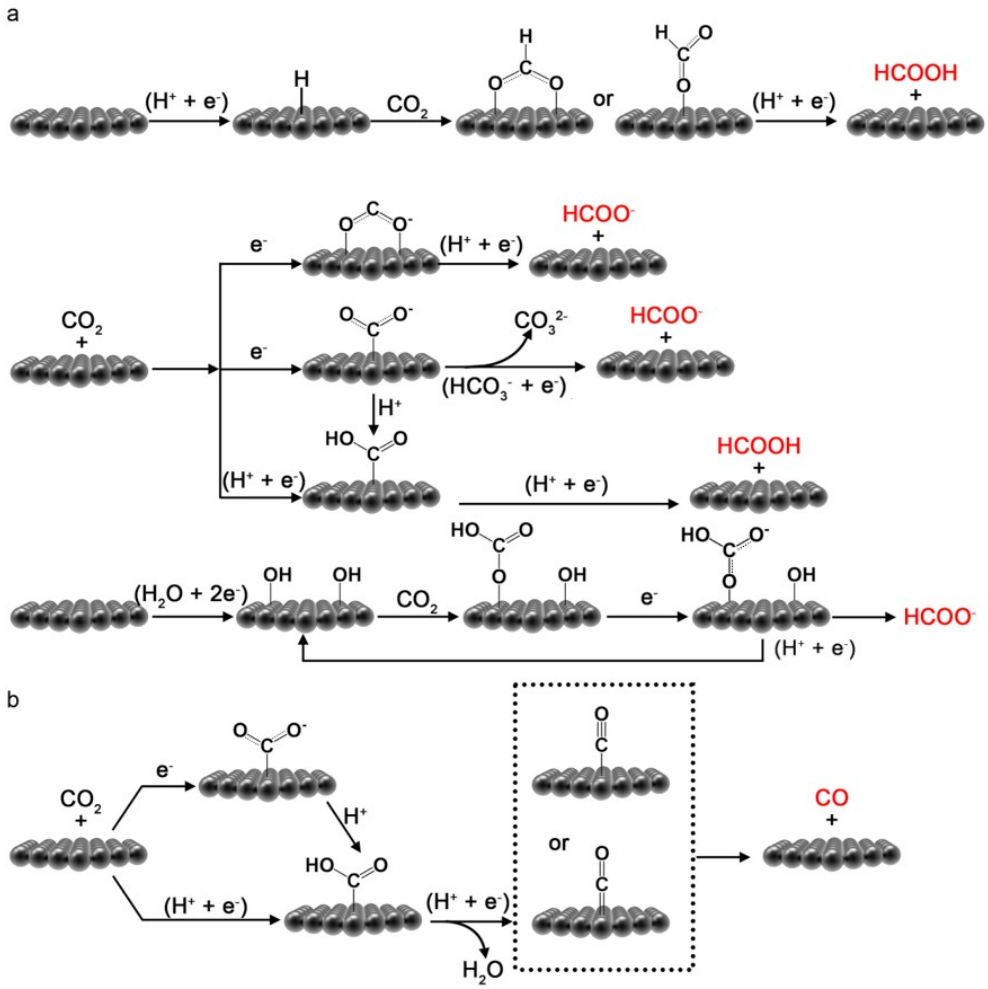


Figure 1.2 Proposed reaction pathways from CO_2 to CO and COOH involving 2 electrons transferring. Reproduced from reference[6] with electron transferring numbers corrected. Copyright 2023 John Wiley & Sons.

Excluding the $HCOOH/HCOO^-$ and CO production, the products of ECR involve the essential *CO protonation step. For CH_4 and CH_3OH, a shared pathway could be the three consecutive proton-electron transfer steps to the *CO intermediate leading to the formation of $*OCH_3$, from which the fourth proton is added to C atom for CH_4 in the gas phase and to O atom for CH_3OH in the liquid phase. However, calculations and experiments suggested different pathways exist. The calculations have revealed that C-O bond dissociation with the C-H bond formation has an energy barrier as high as 1.12eV, which is more unlikely compared to the O-H bond formation (0.15 eV). Therefore, it is usually believed that CH_4 is not formed following this pathway. Other possible routes for CH_4 require an earlier deoxygenation. Nørskov's group had proposed that the dominant pathway for CH_4 includes *CHOH and *CH as intermediates on the Cu(211) surface. The C-O scission is energy-favoured in *CHOH to *CH step rather than the $*CH_3OH$ to CH_4[40]. And for methanol, real-time mass spectroscopy data also suggested a route via *CHOH intermediates but without the C-O breakage[41].

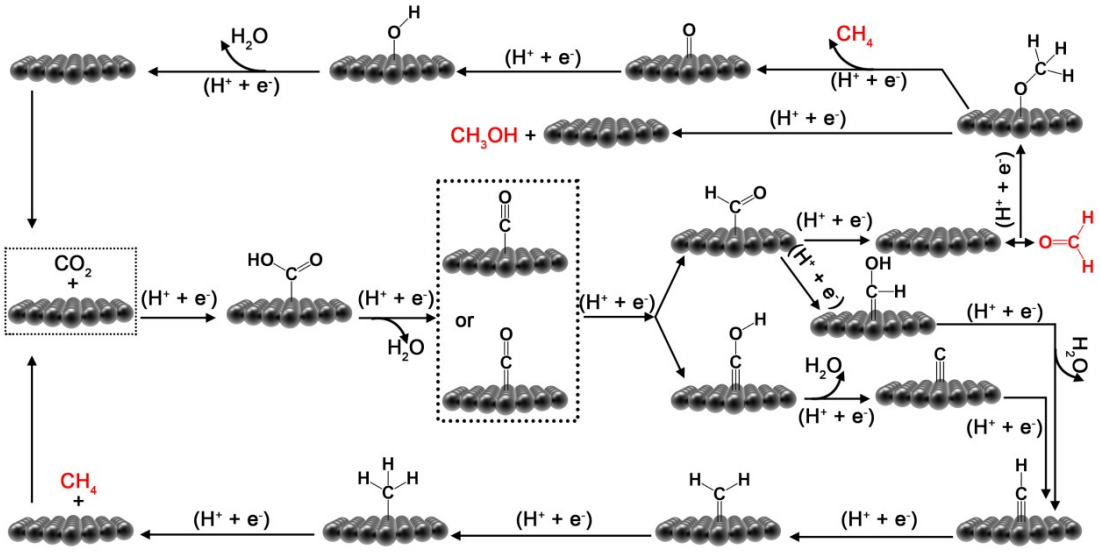


Figure 1.3 Proposed reaction pathways from CO_2 to CH_4 and CH_3OH involving 8 electrons transferring and CO_2 to HCHO involving 4 electrons transferring. Reproduced from reference[6]. Copyright 2023 John Wiley & Sons.

1.2.3 C_{2+} Products and Mechanisms

The C_{2+} mechanism is much more complicated and controversial due to the large variety of transition states. The commonly believed key intermediate *CO is based on the studies of CO production from ECR and the enhanced C_2 products in CO electroreduction experiments[42, 43]. It is proved that the formation of *CO follows the bonding of O-H in advance to the breakage of C-O. The disputation lies in the next C-C coupling step: whether it is the combination between two identical *CO intermediates or there are protons reacting with *CO before the C-C coupling, and if this is the case, with which atom the proton tends to form a bond.

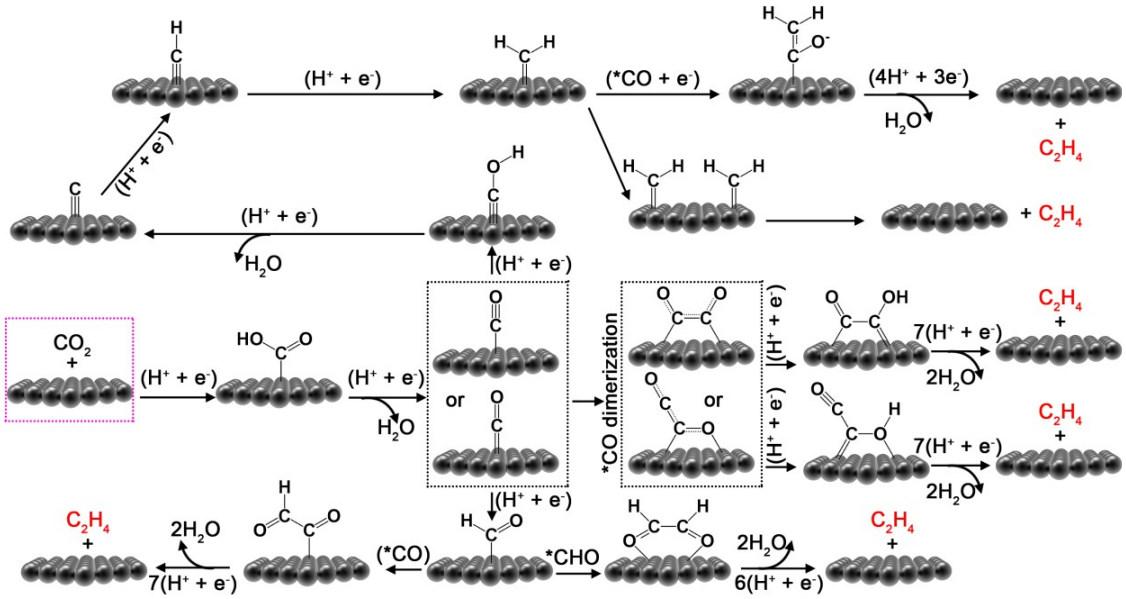


Figure 1.4 Proposed reaction pathways from CO_2 to C_2H_4 involving 12 electrons transferring. Reproduced from reference[6]. Copyright 2023 John Wiley & Sons.

Fig. 1.4 illustrates some possible pathways for C_2H_4 which is the most popular product from ECR. Most of the C_{2+} intermediates are based on the calculation results on a Cu surface. The initial Cu model is built in vacuum with no electrolyte and potential influence. This model provides results that *CO dimerization (OC-CO) must overcome a

high energy barrier (>1.2 eV) even after the exposure to electric fields[44, 45]. Further, researchers introduced water molecules near the surface to build a model closer to real electrolysis conditions[46]. It was then corrected that with a H_2O surface model, the *CO coupling became facile on the Cu surface (Fig 1.4, dashed line box). Recent studies with time resolved surface enhanced infrared absorption spectroscopy also indicated that the dimerization of *CO had a faster kinetics compared to the protonation of *CO to *CHO[47]. However, it is still controversial which step is the rate determine step (RDS) for CO_2 electroreduction on copper materials considering the variety of synthesis, morphology, and surface reactions. There were research groups studying the possibilities of *COH and *CHO involved in the C-C coupling process. Sundararaman's group predicted the OC-COH coupling pathway at neutral and acidic pH while the OC-CO dominates at higher pH[48]. In contrast, Bell and Head-Gordon proposed the ethylene path starting from the OC-CHO coupling due to a more stable *COCHO than the *COCOH[49].

The several electron-proton transferring steps proposed here after C-C coupling lack solid observations from experiments. Due to the short life of these transition states and low coverage on the surface, spectroscopy could hardly collect effective signals during the reaction. Fortunately, these steps often have less impact on the ECR performance as they are unlikely to be the rate-limiting steps.

1.2.4 Selectivity and Faradaic Efficiency

When it comes to the selectivity of ECR, it often refers to the percentage of electrons consumed to convert CO_2, that is, the number of electrons consumed by ECR versus the total number of electrons flowing through the circuit. Unlike the heterogeneous CO_2 hydrogenation where the traditional selectivity concept focuses on the products distribution, in the ECR regime the efficiency of electrons usage is the focus as this

reflects the system energy efficiency. Another reason that researchers seldom report the ECR products selectivity is the low conversion rate particularly for C_{2+} products[50]. This will be further illustrated in section 1.3 where the catalysts play an important role in boosting the performance.

Faradaic efficiency (FE) is one of the most frequently used criteria when evaluating ECR performance. The concept of FE is the electron selectivity towards each product. When calculating the FE, the main concept is to divide the number of electrons transferred to generate the target molecules with the total amount of electrons transferred on the electrode. The equations used to derive and calculate FE will be shown in detail in Chapter 2.

FE is usually monitored at a constant potential or current density. An online GC should be connected to the gas outlet of the cell for real-time measurements, or a gas-tight syringe should be used to collect the gas sample for analysis. It is important to report the operation condition corresponding to each FE. FE reflects the distribution of each product including H_2 from the competitive reaction HER. The higher FE under a certain voltage/current indicates a higher selectivity of the target product. When testing the lifetime of an ECR system, a stable FE is desired with no significant increasing of H_2 FE. So far, the FE of HCOOH and CO could reach almost 100%[16, 51-53], while for hydrocarbons there is room for improvement. The FE of CH_4 is usually below 60%[54, 55] due to the inevitable proton activation from HER and C_{2+} could achieve over 80% by summing up C_2H_4 and alcohols in the highly concentrated alkaline solution[29, 30, 32-35].

1.3 Development of ECR Catalysts

Most of the ECR catalysts can be divided into three categories by the product types according to the literature survey. The first group of elements consists of Pb, In, Sn and

Bi *etc.* which tend to produce formic ions ($HCOO^-$). The second group includes Au, Ag, Pd, Ni and Zn elements that reduce CO_2 into CO in most cases. The third group has only one candidate, copper.

1.3.1 Non-copper Electrocatalysts: towards CO and HCOOH/$HCOO^-$

In this section, the first and second groups of elements will be introduced. By classifying them with the targeted products, a detailed picture of transition metals for ECR to C_1 products will be displayed.

Production of CO. CO is the simplest product in gas phase from ECR. As it involves a single deoxygenation step from CO_2, it is, so far, one of the most well-studied products among all ECR. The reason why researchers are interested in investigating CO is that it is an important chemical feedstock for processes such as Fischer–Tropsch synthesis and hydrogenation process for methanol production[56, 57]. It is also a necessary component of syngas and the ratios between H_2 and CO is controllable via the changing of potentials[58, 59].

Morphology control is the most frequently applied method to improve the selectivity. At atomic scale, it can be explained as the controlling of exposed reactive sites (edges, steps, and corners *etc.*) or the creation of defective sites, *i.e.*, the unsaturated coordination environment. A porous structure could increase the area of exposed surface, that is, the specific surface area of the electrode. It had been found that the porous Zn metal catalysts showed nearly doubled CO selectivity compared with Zn foil[60]. Jiao *et al.* had prepared Ag with nanoporous structure that displayed the selectivity of CO up to 92%. They claimed that the high curvature of the pore inner surface was the key to stabilize the activated CO_2^- intermediate[61]. A hierarchical hexagonal Zn catalyst was developed by Woo *et al.* with Zn(101) facet dominant the surface. The authors concluded that the

improved CO selectivity up to 84% is due to the increased ratio of Zu (101)/(002) compared to the Zn foil[62]. Furthermore, the facet dependency was studied by Bell *et al.* who compared Ag(100), (110) and (111) facets using DFT calculations[63]. The binding energy calculated for *COOH intermediate was higher at the less coordinated step surface. It was noteworthy that the authors corrected the results with a homogeneous electric field which predominately lowers the free energies of *COOH formation step. Such field effect was also supported by the Au needle electrocatalysts developed by Sargent's group[64].

In addition to the morphology engineering, researchers also paid attention to the interface of the materials. With the development of advanced spectroscopy technologies, it became possible to visualize the transformation of crystal surfaces under certain conditions. Kanan's group first applied the in situ scanning electrochemical cell microscopy to understand the grain boundaries of Au surface at submicrometric scales[65]. Direct evidence was provided that the selectivity of CO_2-to CO was indeed improved on the boundaries of Au electrode but not for the competing HER. A further look at the interface with the electron backscatter diffraction also from Kanan's group elaborated that the dislocation of atoms was the reason for higher CO selectivity[66]. Their findings from mapping the Au electrode supported the assumption that defects accumulated at the interface and such dislocation of unsaturated-coordinated atoms enhanced the performance. It is also vital to clarify that ECR on Au electrode is not sensitive to the lattice strain on its own.

Single-atom catalysts (SACs) have been exploited massively in the recent years, though there is not even a commonly accepted definition for it. The core idea of SACs is to use an appropriate support to disperse the metal atoms uniformly and highly on the surface and stabilize them during the reaction. The unsaturated coordination environment of metal centres accounts for the high reactivity. Nevertheless, SACs can sometimes be

treated as dopants to the support considering the low amount of exotic metal atoms (<1%). There are also molecular catalysts in which the metal sites serve as the reaction centre[67, 68] such as Co(II) phthalocyanine (CoPc)[69, 70]. For the CO_2-to-CO conversion with one CO_2 molecule involved solely, or in other words as a single-site reaction, it is reasonable to take the advantage of SACs which does increase the efficiency of atom usage and the number of exposed sites.

Among the large varieties of SACs researchers had explored, the M-N_x and M-N_x-C sites (M stands for metal, N for nitrogen and C for carbon atoms) were selected as one of the most effective SACs. For transition metals including Fe, Co, and Ni *etc.*[67, 68, 71, 72], such binding sites could be identified by extended X-ray absorption fine structure spectroscopy (EXAFS) and high-angle annular dark-field scanning transmission electron microscopy (HAADF-STEM). Calculations on M-N_4 model also pointed out that the binding energy of *CO is controllable by the metal centre and peripheral molecules[73]. This raised the possibility of mimicking copper metal surface (will be introduced in the next section) to achieve higher efficiency of ECR. It is impressive to find that a Ni-N-C type material with only 0.27% metal loading on the nitride-functionalized carbon black (CB) could reach nearly 100% CO selectivity[74]. Borrowing the concept from homogeneous catalysts, a class of molecular catalysts being immobilized on carbon supports also showed high efficiency for CO production up to 95%. CoPc, FePc and NiPc loaded on carbon nanotubes (CNTs) maintained the M-N_4 active centre that altered the electronic structures favouring the reduction of CO_2 over HER[73].

Production of HCOOH/HCOO$^-$. Formic acid is potentially an efficient H_2 carrier with 53 g_{H2}/L capacity[75]. It has also been widely applied in the textile industry and chemical production. Catalysts with elements from the first group shows superb selectivity towards formic acid and some of them demonstrated in conditions close to the industrial level.

Sn-based catalysts are usually studied in the form of oxides and sulphides[76, 77], both of which showed good stability in water and air. It was found by Chen and Kanan that even under the long-term reducing condition, there were residual oxygen atoms taking part in CO_2-to HCOOH reaction and they are likely to be the driving force of surface reconstruction[78].

It was not until recently that Bi was first tested in an aqueous ECR system which unveiled its huge potential in $HCOO^-$ ions production from CO_2[79-81]. Wang *et al.* improved the electrolyser with a porous solid electrolyte (PSE) that allowed pure formic acid production directly from the electrochemical cell for 100 hours[15]. The catalyst they applied was ultra-small Bi nanoparticles prepared under extreme conditions with *n*-Butyllithium (*n*-BuLi) exfoliation. They claimed that the grain boundaries formation resulted from the n-BuLi treatment and a further reduction of Bi_2O_3 to metallic Bi took place during the removal of excessive Li and Li_2O by water treatment. The small particle size and abundant grain boundaries led to the exceptional high efficiency of the catalysts.

As a noble metal, Pd was not investigate as much as the previous elements. It was often used as a dopant or alloy element into particles or with non-metal materials to finely control the surface properties, especially the adsorption ability to *CO[82]. For example, $Pd_{70}Pt_{33}$ catalyst developed by Koper and co-workers had an onset potential close to 0 V with the 88% selectivity to $HCOO^-$[83]. It was found that most Pd-based catalysts for $HCOOH/HCOO^-$ did not perform ECR with high and stable selectivity compared to Sn and Bi. But Pd plays a more valuable role with Cu for C_{2+} production which will be included in the next section.

1.3.2 Copper-based Electrocatalysts

Copper is the essential material for ECR to produce hydrocarbons (CH_4, C_2H_4 and C_2H_6) and other multiple-carbon products (C_{2+}) such as alcohols and acids in a quantitively reproducible amount. This section will focus on Cu only and the key intermediates that affect C-C coupling.

Production of CH_4. Methane is the main component of natural gas. It could be used as a feedstock to produce chemicals such as methanol, formaldehyde, and chloromethanes *etc.* apart from being fuel for heating and electricity generation.

The production of CH_4 from ECR heavily relies on copper-based materials. Similar concepts of catalysts design were used to prepare Cu catalysts including morphology control, interface engineering and single atom doping. For example, a fivefold twinned Cu nanowire was synthesized by Yang's group which exhibited FE at 55% CH_4 selectivity[84]. It was claimed by the authors that the improved efficiency resulted from the higher concentration of edge sites exposed between the twin boundaries. Zheng's group constructed a Cu SACs on CeO_2 catalysts[85] which had multiple oxygen vacancies around the Cu site. This catalyst showed up to 58% FE towards CH_4 at -1.8V_{RHE}. The choice of support to stabilize Cu site is not limited to conventional metal oxides or carbon/nitrides. Recently, perovskite has also been attractive due to its flexibility in structure and unique electromagnetic properties from lanthanide elements. Xia's group designed a copper perovskite with a CuO_6 octahedral coordination intercalated in two LaO layers[86]. The Cu/ La_2CuO_4 is believed to enhance the methanation of CO_2. It was also reported in some papers that a Zn SAC catalyst loaded on N-doped carbon could reach the CH_4 FE over 85%, yet these results were controversial on the measurement conditions and data analysis[87].

In short, the development of catalysts for CH_4 production from ECR still has room for optimization. The intrinsic 4-step proton-electron transferring process decides that the proton activation is inevitable, and the competitive HER can hardly be supressed. Efforts on SACs showed possibilities to improve the efficiency and the interface effect between Cu and support could not be neglected either.

Production of CH_3OH presumably shares a similar route as CH_4 (**Fig. 1.3**), yet it has rarely been reported in aqueous ECR. To produce CH_3OH, ionic liquid is an important component for the electrolyte such as butyl-3-methylimidazolium tetrafluoroborate ([Bmim]BF_4). A Pd-Cu catalyst was reported to achieve CH_3OH FE at 80% with a at around 30 mA/cm^2 methanol partial current density[88]. It is also possible to use a mixture of ionic liquid and aqueous sulfuric acid for CH_3OH production. However, due to the difficulties in separate and purify the products, it is not widely believed to be a practicable solution for CO_2-to-CH_3OH conversion[89]. As CH_3OH is seldom observed as a product in an aqueous ECR cell, this thesis will not elaborate more on its catalysts design.

Production of C_{2+}. When it comes to C_{2+} products, it often refers to ethylene, ethanol, and n-propanol. These three products have the highest efficiency among all the multi-carbon products. With the existing processes, these products could then become various chemicals such as aromatics, cyclic alkanes, and fuels. It is, therefore, promising that CO_2 could be directly converted into C_{2+} products through one single step.

The development of Cu-based catalysts for aqueous ECR has been decades with Hori et al. observed that CO_2 could be converted with metal electrode into gaseous products in 1986[90]. It did not attract much attention until the 2010s when climate change and carbon emission became the burning issue for all human being. With the assistance of advanced cell design and material characterisation techniques, ECR came back to researchers'

horizon targeting at producing high-value C_{2+} with efficiencies meeting the industrial requirements.

In 2012, Kanan's group reported an oxide-derived copper (OD-Cu) catalyst by annealing the copper foil in air and then electrochemically reducing the oxide layer[27]. The resulted catalysts showed a lower overpotential to produce CO and HCOOH and the ability of producing C_2 products at higher overpotential. It was believed that the grain boundaries formed during the *in-situ* reduction of Cu could strengthen the adsorption of *CO intermediate and the following protonation steps. Further studies were conducted not only on visualising the grain boundaries as introduced previously, but also on the role of surface oxygen residual. One example was that Cu_4O_3 paramelaconite, a mixture of Cu(I) and Cu(II) oxides, was used as the electrocatalysts with a C_{2+} selectivity up to 60% with at $-0.59V_{RHE}$[91]. It was believed that only surface Cu underwent the reduction reactions completely, while the bulk still had Cu(I) species. This caused trouble in identifying the active phase of the materials experimentally. However, isotope experiments conducted by Ager with ^{18}O suggested that a 10 min reduction of OD-Cu could lead to over 99% reduction to metallic Cu[92]. Whether the oxygen residual could last during the reaction and what role it is playing remain unclear.

However, theoretical works supported that these partially oxidised copper in the surface/subsurface layer might exert influence on the performance as they were believed to resist of being reduced. Based on this type of theory, a series of doped copper materials were tested for ECR. The boron and nitrogen were doped into Cu particles to control the valence state of Cu ions. It was found by Sargent *et al.* that the oxidation state of Cu was closer to Cu_2O as the doping level of B increasing[93] and that the N doping could significantly increase the ratio of Cu^+ [94]. Ye Wang's group investigated surface-decorated Cu nanoparticles with halogen (F, Cl, Br, and I)[95]. They discovered that the Cu-F bond on

the surface had the most prominent effect on boosting the C_{2-4} selectivity to over 80% at a total current density of 1.6 $A \cdot cm^{-2}$ with a single-pass yield of 16.5%. While the attempt was made to decouple the effects of F-decoration and Cu^{+} ions, or more precisely, $Cu^{\delta+}$ (partially oxidised copper), it is possible that the metal-F bonding had changed the electronic states of Cu which eventually influenced the performance. Fundamentally, these two effects are the same, which can be ascribed to affecting the binding energy of intermediates. All the doping and functionalization of copper share the identical purpose of driving the electronic states of surface Cu sites for ECR towards a C_{2+}-favoured direction.

Another strategy of improving Cu catalysts for C_{2+} production is alloy with transition metals including Pd, Au, Ag and Co *etc*. Though it is often discovered that the monometallic copper is the optimized materials, the introducing of heteroatoms effectively alters the behaviour of Cu. For example, a Pd-doping into Cu did not always increase the selectivity towards C_2 products. The highest selectivity of C_2 was achieved in a phase separated CuPd particle, while the disordered mixture (close to the alloy), in turn, favoured the production of CO[96]. Sargent's group first predicted that a Cu-Al alloy could improve the performance of CO_2-to-C_{2+} with the assistance of machine learning[97]. It marks the start of a new era that researchers no longer need to test each element on the periodic table but could train a model to make predictions ahead of experiments. However, the training of an accurate model depends heavily on the quality of datasets from the previous experiments and calculations, which makes this method far from being practical used in real research scenario.

Apart from altering the surface Cu site by introducing atoms to the catalysts, it is also possible to use organic molecules as binders to confine the local environment on the catalysts surface[34, 98]. The most used Nafion® binder in ECR can be classified into this

category as it provides accessible pathways for the cations moving to and from the electrolyte. The development of ion-conducting polymers will be introduced in the next section as they are now playing a vital part in ECR system, not limited by the performance. Sargent *et al.* investigated a library of molecules derived by electro-dimerization of arylpyridinium on Cu electrodes[99]. They found that *N*-aryl-substituted tetrahydro-4,4′-bipyridine molecules could assist the stabilization of *CO intermediate thus achieving a FE over 70% to ethylene in neutral medium. By comparing the performance of different functional group-substituted tetrahydro-bipyridines, they concluded with the relationship between the ethylene selectivity and the Bader charges of N atom in the molecules that a moderate electron-donating ability favours the ethylene selectivity[99]. It was noteworthy that the addition of a thin polymer layer did not substantially retard the electron transfer nor affect the morphology of Cu electrode as the authors claimed. Zheng *et al.* recently applied toluene to modify the Cu surface, where the distance between each benzyloxy group was 5.1 Å. This could successfully prevent water molecules from flooding the catalysts while allow sufficient CO_2 feeding, resulting in a stability of CO_2-to-C_2H_4 for over 400 hrs[100]. Alternatively, Sinton's group chose a benzimidazolium-based ionomer to replace the alkali cations within the ionomer coatings to functionalize Cu surface and around 83% FE towards C_{2+} was achieved in acidic conditions[101].

Further to the reduction of CO_2, scientists realized that the higher CO concentration of the reactant is, the higher C_{2+} productivity can be achieved with the similar Cu catalysts[102, 103]. This phenomenon agrees with the assumption that *CO is the key intermediate for C_{2+} production. By jumping to the CO reduction, the thermodynamically unfavoured CO_2 activation step could be avoided which greatly lowered the overpotential. While the CO reduction allows a higher yield and selectivity, it requires an extra step of converting CO_2

into CO which is energy-consuming from the perspective of chemical process. In this thesis, the reduction of CO will not be discussed in detail as the direct conversion of CO_2 is the focus.

Overall, the application of ECR under a broader scope not only requires the development of novel materials as the electrocatalysts, but also the design of reactors and other downstream engineering process.

1.4 Electrolysers Configuration of ECR

The development of electrolysers for ECR paved the way for potential industrial applications. Based on the status of electrolyte, static or flow, the electrolysers of ECR have two categories: H-cell and flow cell. The flow cell, benefiting from its layered structure, could be further classified into the one-/two-gap flow cell and the zero-gap membrane electrode assembly (MEA). In this section, each type of the reactor will be introduced followed by the introduction on ion-exchange membrane that separates the compartments and provides ion conductivity across the cell.

1.4.1 H-cell

H-cell gets its name from the shape (**Fig. 1.6**). It was developed from the single compartment cell that was used in traditional electrochemistry with a cathode for reductive reactions and an anode for oxidative reactions. The addition of a second compartment separated the oxidation and reduction reactions (**Fig. 1.5**, right and left compartment, respectively) on the two electrodes, which avoid the re-oxidation of reductive products and vice versa. As the focus reaction is CO_2 reduction which takes place on the cathode, the cathode could also be called working electrode (WE) and the anode counter electrode (CE).

To conduct ECR measurements in H-cell, CO_2 is supplied into the cathode side where both water and CO_2 will be reduced. The inlet of CO_2 is placed close to the cathode to minimize the diffusion distance. However, when the inlet is too close to the electrode surface, bubbles will sometimes block the surface and cause open circuit or fluctuations in the current density. The gas products of ECR will be removed with the CO_2 flow and are usually analysed an online GC for real-time quantification. The liquid products, on the contrary, accumulate in the cell over the reaction and hence the quantifying of their efficiency or selectivity is less accurate compared to gas products which should not be reported in the same graph.

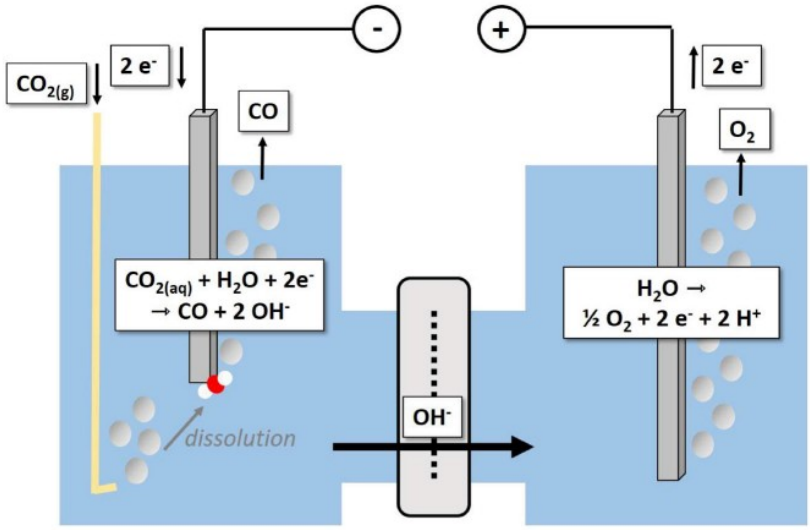


Figure 1.5 Scheme of ECR in H-cell with simplified representation of processes during the reaction. The dashed black line represents ion-exchange membrane. Reprinted from reference[104]. Copyright 2022 Elsevier.

The outstanding problem of H-cell is the mass transport limitation of CO_2. One reason for this is the low solubility of CO_2 in the aqueous electrolyte (about 34 mM). It is possible to use alkaline solution with higher pH which does increase the solubility but also consume a considerable amount of CO_2 forming carbonates. Another way to overcome the low solubility is to use organic solvents or ionic liquid yet they could not offer higher

conductivity. It is also problematic to use solvent that has molecules included in possible reduction products such as methanol and ethanol which would influence the calculation of efficiency. As a result, the concentration of reactant in the H-cell for ECR is not likely to allow a high current density nor a high conversion of CO_2.

1.4.2 Liquid-phase Flow Cell

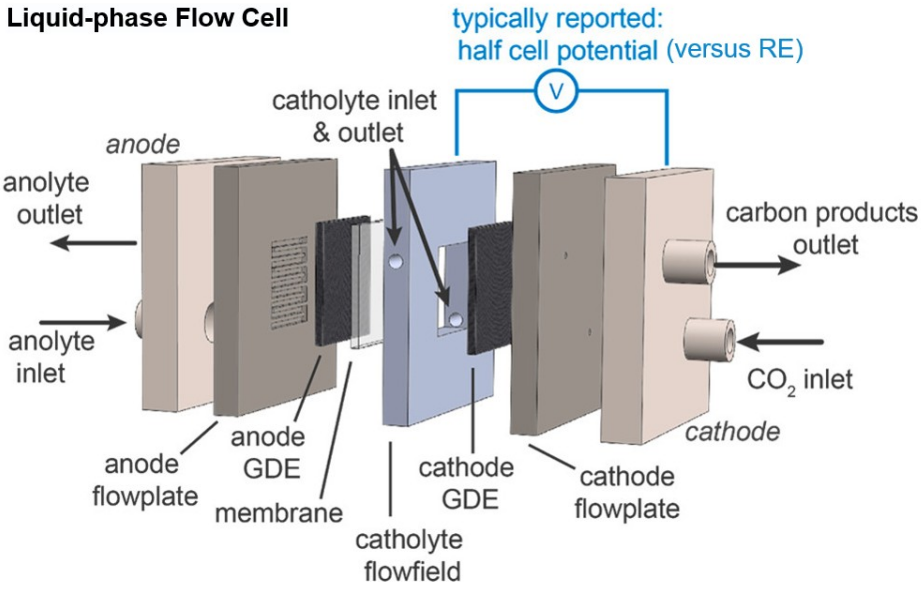


Figure 1.6 Illustration of a liquid-phase flow cell. Reprinted with permission from reference[105]. Copyright 2020 American Chemical Society.

The flow cell introduced in this section has a layered structure that consists of two electrodes (cathode and anode) each with a flow plate, a membrane separating the two electrodes and an extra electrolyte flow field for cathode (**Fig. 1.6**). The catholyte layer is usually a few millimetres thick to minimise the ion diffusion distance as well as the solution resistance. A reference electrode (RE) is inserted in the centre of the catholyte layer during the measurement. This excludes the effect of counter electrode by monitoring the potential difference between WE and RE (**Fig. 1.6**, highlighted in blue). When evaluating performance between different cathode catalysts, the liquid-phase flow cell should be used for testing.

The design of flow cell perfectly tackles the mass transport limitations in H-cell. The use of gas diffusion electrode (GDE), a hydrophobic, conductive, and porous substrate, has constructed a three-phase interface where CO_2 in the gas phase is separated from the liquid phase. The joint point of gas and liquid phase is the catalysts surface (solid phase) on which the reduction reactions take place. **Fig. 1.7a** shows an enlarged and more detailed structure of a half flow cell.

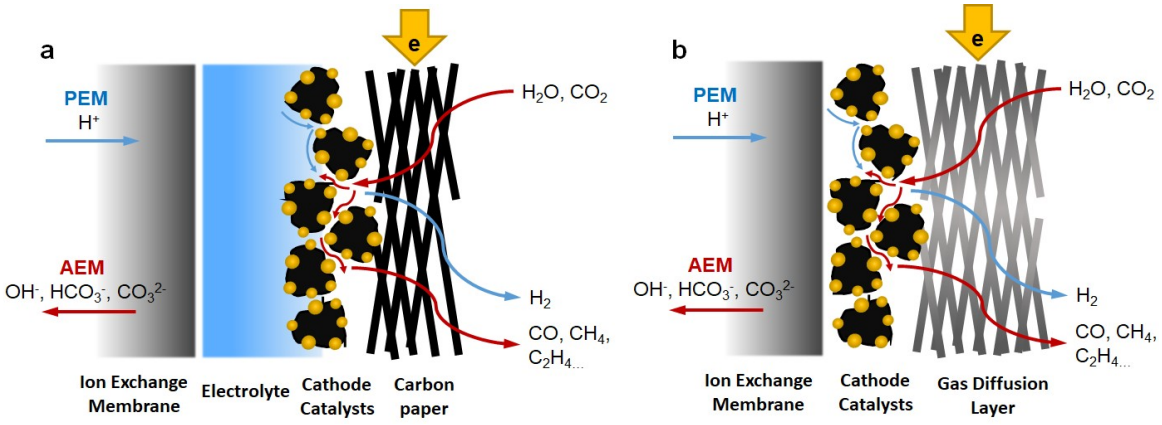


Figure 1.7 Configurations of the cathode chamber in **(a)** liquid-phase flow cell and **(b)** membrane electrode assembly (MEA). Blue arrows indicate the move of proton and hydrogen; red arrows indicate the move of carbon species in gas phase across the catalysts and membrane.

Carbon paper is the most used GDE substrate which serves as a conductor, catalysts supporter and gas diffusion layer. Recent advances in carbon paper modification focus on improving the hydrophobicity and gas permeability. The addition of a thin polytetrafluoroethylene (PTFE) layer could significantly increase the lifetime with a little trade-off on conductivity. The fabrication of catalyst layer onto GDE is via spray-coating a thin film with uniform thickness, usually tens of micrometres. The detailed processes will be introduced in Chapter 2. When assembling the flow cell, the catalysts layer should face the electrolyte and the carbon support face the gas supply.

The deactivation of ECR in flow-cell is due to the flooding of electrolyte over the GDE. This is reflected by the appearance of liquid in the gas chamber and outlet. When electrolyte penetrate through the GDE, the contact between the catalysts and reactant gas is cut off, hence ECR is fully blocked. To decrease the possibility of flooding, a carbon layer composed of graphite and carbon black on top of the catalyst layer was proved to be effective[31]. Moreover, a PTFE substrate could be applied to support the catalysts layer even though the material itself is an insulator. The electrical contact must then be realized through the catalyst/carbon layer. Sargent's group has successfully achieved high current density up to 1 $A \cdot cm^{-2}$ with a selectivity to C_{2+} over FE 85%[106].

The choice of membrane depends on the electrolyte and the ionomers added to catalyst ink. The left part of **Fig. 1.7(a)** marks the two major types of membrane, the proton exchange membrane (PEM) and the anion exchange membrane (AEM). How the membrane properties exert influence on the operation of the system will be introduced later in section 1.4.4.

1.4.3 Membrane Electrode Assembly (MEA)

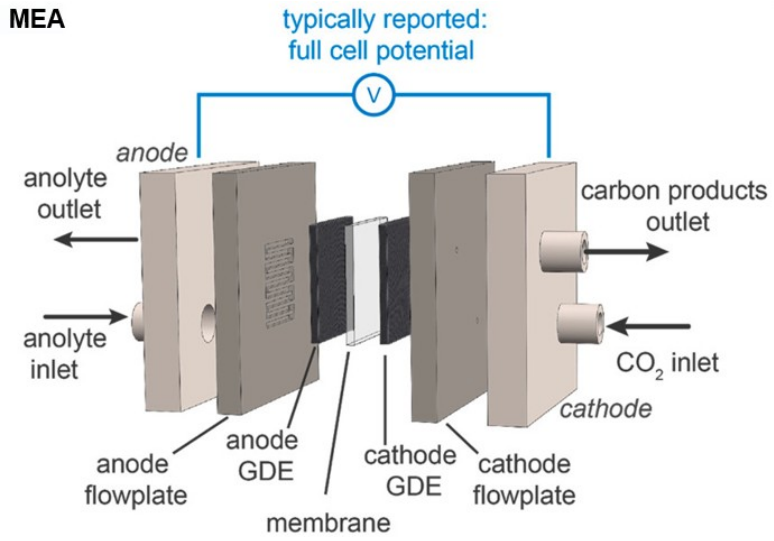


Figure 1.8 Illustration of a membrane electrode assembly cell. Reproduced from reference[105]. Copyright 2020 American Chemical Society.

The only difference between the MEA and the liquid-phase flow cell is the physical state of electrolyte layer. MEA could be regarded as a flow cell with an infinitely small gap between the cathode and the membrane (**Fig. 1.8**), where MEA gets its name as zero-gap flow cell. The membrane in MEA is not only a salt bridge but also serves as solid electrolyte, which makes MEA also known as solid-phase flow cell. Without a liquid layer, the suffering of flooding in a flow cell that worsen the stability and lifetime is relieved. With the cathode and the anode sandwich the membrane, the mass transfer resistance could be significantly decreased. This leads to the capability of operating MEA at much higher current that could meet the industry's standards[107].

With the omission of the catholyte layer, it is essential to supply moisture from the gas stream. A humidified CO_2 flow is necessary for MEA to maintain the ion conductivity of membrane as well as the proton supply. It should be mentioned that there is still some possibility of flooding in the MEA cell, even though the use of aqueous solution has been avoided in the cathode chamber. The production of liquid products from ECR and the moisture from CO_2 stream could block the pores of GDE resulting in cell deactivation.

At large current density, the consumption of protons to form hydrocarbons would lead to OH^- ions accumulation near the surface of electrode. Excessive OH^- ions would be likely to react with CO_2 directly generating carbonates[108]. The carbonate salts might precipitate on the cathode, which again block the pathway for CO_2 diffusion. To retard the formation of carbonates, water could be used as anolyte in MEA which lowers the concentration of OH^- and facilitates the OH^- transport towards the anode chamber driven by the electric fields. Other possible solutions are related with the employment of membrane which will be included in the next section.

1.4.4 Ion-exchange Membranes

The role of ion-exchange membranes in any ECR system is irreplaceable. There are three major categories based on the charge carriers (**Fig. 1.9**): proton/cation-exchange membranes (PEM/CEM) for ions including H^+ and K^+, anion-exchange membranes (AEM) for OH^- and HCO_3^-, and bipolar membranes (BPM) that combines PEM and AEM.

As a salt bridge in electrochemical cells, membranes physically separate the cathode and the anode chamber without short circuit and allow specific ions to move through. The mechanical properties such as strengths, toughness and elasticity of a membrane decide whether it could last long during the electrochemistry process. The preparation of a MEA sometimes involves hot press at high temperature and pressure to create close contact between catalysts and the membrane which requires the polymer with good heat endurance. As the production of gas products on both electrodes would usually create imbalanced pressure between two chambers, a strong physical strength is also necessary to guarantee a long lifetime of the membrane.

From the chemical side, the ion conductivity is the most important criterion. The higher conductivity of the membrane is, the less ohmic resistance and potential loss in the cell. The conductivity is positively correlated with the level of humidity, ion concentration and temperature[109]. The thickness of the membrane also has influence on the conductivity, where a thick membrane usually shows higher resistance. However, a thick membrane is not always a drawback. Crossover through the membrane of reactants and products could also affect the overall efficiency of ECR cell, and a thick membrane would lower the possibility of crossover.

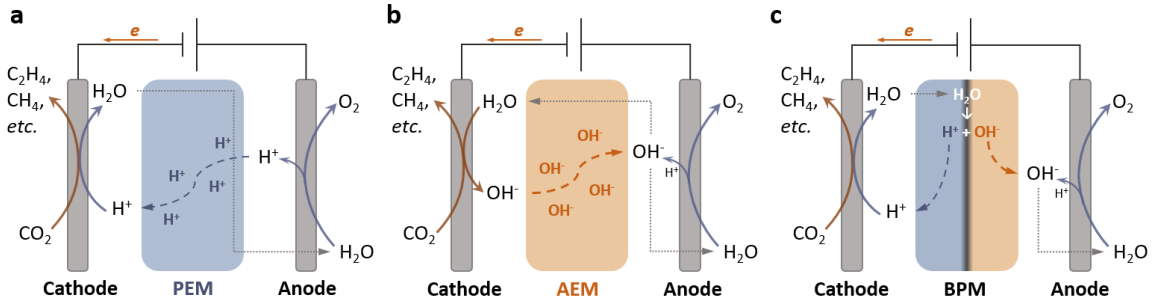


Figure 1.9 Illustration of **(a)** proton, **(b)** anion exchange membrane and **(c)** bipolar membrane applied in ECR systems. Dashed arrows indicate the moving direction of species in the membrane. Solid arrows indicate the reaction taking place on the electrodes.

PEM has a mature fabrication technology that has been widely applied in water electrolysis and fuel cell. In PEM, protons are allowed to pass through the membrane driven by concentration gradients and electric fields. For ECR measurements, the oxidation of water takes place on the anode where 4 protons are generated for each O_2 molecule. The protons would then move towards the cathode closing the inner circuit and compensate for the proton consumption in the cathode from HER or ECR (**Fig. 1.9a**). Taking the popular Nafion® membrane as an example, instead of diffusion, the protons when moving within the membrane are 'hopping' from one sulfonic acid site ($-SO_3H$) on the PTFE backbone to another. The proton conductivity of an untreated Nafion® 117 membrane is *ca.* 78 $mS \cdot cm^{-1}$ [109]. It is possible to exchange cations with Li^+ and K^+ *etc* depending on different applications.

The issue of PEM in ECR system is the high proton conductivity could easily establish H^+ accumulation on the cathode. Yet the advantage is that acidic electrolyte decreases the carbonation process that could consume most of the CO_2 before electrolysis. Sargent's group recently achieved 26% FE to ethylene in a K^+-rich acid electrolyte and a single-pass conversion of over 70%[110]. For acidic catholyte in flow cell, the pH will decrease as

the reactions happening. HER is, therefore, favoured over ECR. To avoid this, AEM seems to be a better choice for ECR-to-C_{2+} in terms of efficiency.

AEM transports anions (OH^-, CO_3^{2-} and HCO_3^- *etc*.). It is a relatively new research field compared to PEM. There have been a few types of AEM commercialized, one of which is the Sustainion®, a polystyrene backbone functionalized with imidazolium groups. Though Sustainion® AEM features high OH^- conductivity, it is still over one order of magnitude lower than Nafion® and its mechanical strength is an issue. Pre-treatment of ion exchange is necessary to activate the Sustainion® membrane by replacing the chloride with hydroxide ions within the polymer networks.

The crossover of products and ions exists in AEM as in PEM. Different from proton movement, carbonates and bicarbonates will move towards the anode driven by the electric field and concentration gradients. Excessive hydroxide ions also lead to formation of carbonates after their direct reactions with CO_2 in the cathode chamber. On the anode side, carbonates then react with the protons from water oxidation and part of them is released in gas phase from the anode. This process matters when the current density of ECR reaches ampere's level and up to 50% CO_2 will cross over the membrane to the anode instead of being reduced to the desired products[108]. Such effect is ceiling the single-pass conversion rate of ECR. Furthermore, some liquid products such as formic acid and alcohols will diffuse to the anode due to the concentration difference regardless of the potential as they are uncharged molecules. Overall, both PEM and AEM show the intrinsic crossover problem which limit the efficiency of ECR.

BPM consists of one PEM and one AEM which allows both cations and anions transferring within the confined electrode chamber[111]. A water dissociation catalyst layer is usually sandwiched between the two membranes to achieve rapid splitting of water and

avoid delamination of two membranes. The proton and hydroxide migrate towards the cathode and anode, respectively, under the electric field applied to the cell (**Fig. 1.9c**). This also prevents the crossover of products and ions between the electrodes and ideally should increase the total carbon utilization rate.

Due to the combination of two ion-exchange membrane, the resistance of BPM is generally larger than the single membrane. Additionally, the water dissociation ($H_2O \rightarrow H^+ + OH^-$, note its difference from water splitting to gaseous products) requires extra energy (*ca.* 1V)[112] input to functionalize the membrane which increases the total operation voltage. Therefore, it is far too early to conclude that BPM is the final choice of membrane in ECR cell.

In short, each type of membrane has its advantages and shortages. PEM offers high standard mechanical properties; AEM shows the best efficiency for ECR and BPM allows the least crossover. However, there has not been a membrane that could meet most of the requirements for long-term ECR measurements. The selection of an appropriate membrane for experiments depends on the types of electrolytes, the applied voltage, the configuration of electrolysers and the targeted products or efficiency. In this thesis, AEM was the choice for most of the ECR measurements, which provides moderate conductivity and less voltage loss.

1.5 Aims and Objectives

Based on the discussion of ECR basics and its development so far, it is of great significance to optimize this reaction targeting at hydrocarbons. In this thesis, copper-based catalysts are studied in flow cell systems to understand the structure-activity-selectivity relations of ECR with a focus on the production of methane and ethylene.

As illustrated in section 1.2, ECR is suffering from insufficient activity and selectivity. Copper materials were chosen as electrocatalysts, and by engineering the interface and the surface, high efficiency and selectivity towards methane and ethylene were both achieved. The principle of interface design is to boost the efficiency of CH_4 production from CO_2 by accelerating the proton transferring rate with substrates that possess higher proton conductivity (MoS_2 and $MgO/Mg(OH)_2$). For surface engineering, it takes the advantage of the small size effect of nanomaterials to optimize ethylene selectivity by introducing sufficient active sites and altering the neighbouring environment. Combining both strategies, surface reactions that lead to different products on electrodes are unveiled.

While the catalysts play an important role in ECR, cell design also determines the future application of the reaction at a larger scale. In this thesis, two mainstream electrolysers (two- and zero-gap cells) are applied to test the performance which provide insights into the choice of catalysts as well as electrolyser engineering.

1.6 Thesis Overview

This thesis is divided into 6 chapters. In addition to a general introduction and literature review in this chapter, chapter 3 to 5 provide the details of experimental work carried out over the course of the DPhil degree.

Chapter 1 introduces the concepts of electrochemistry related to ECR and provides a broad literature review on the current development of ECR from electrode materials to electrolysers. The motivation and aim of this thesis are also illustrated in this chapter.

Chapter 2 details the characterization techniques and their principles used throughout the thesis, followed by a detailed description on the experimental methods including catalyst synthesis, performance tests and electrochemical setups.

Chapter 3 focuses on the methane production from ECR via the construction of metal-support interface. Substrates with high proton conductivity were introduced to support copper particles. The relationship between support types and ECR selectivity was studied to understand methane production mechanism.

Chapter 4 investigates the behaviours of Cu particles on GDE in different aqueous environments. An optimal synthesis method of Cu particle was selected. Both the alkaline and neutral conditions were studied with EIS to elaborate how electrode surface process determines the final product patterns.

Chapter 5 described the achieved enhancement of ethylene production in near-neutral environment on Pd doped Cu particles. Controlling the dopant Pd amount resulted in changes of product distribution. Operando studies by PTR-TOF-MS assist the elucidation of possible mechanism leading to C_1 and C_2 products.

Chapter 6 concludes the whole thesis and provides a perspective of future development of catalysts and electrolysers for ECR.

1.7 References

1. S. Anna, A Low Ineffective French Carbon Tax Lies Frozen at 2018 Level - Climate Scorecard, https://www.climatescorecard.org/2020/03/the-dysfunctional-french-carbon-tax-is-frozen-at-2018-level/.
2. C. Government, Pan-Canadian Approach to Pricing Carbon Pollution - Canada.ca, https://www.canada.ca/en/environment-climate-change/news/2016/10/canadian-approach-pricing-carbon-pollution.html.

3. E. U. Commission, 2050 long-term strategy, https://climate.ec.europa.eu/eu-action/climate-strategies-targets/2050-long-term-strategy_en.
4. D. Zhang, J. Wang, Y. Lin, Y. Si, C. Huang, J. Yang, B. Huang and W. Li, Present situation and future prospect of renewable energy in China, *Renew. Sust. Energ. Rev.*, 2017, **76**, 865-871.
5. K. P. Kuhl, T. Hatsukade, E. R. Cave, D. N. Abram, J. Kibsgaard and T. F. Jaramillo, Electrocatalytic conversion of carbon dioxide to methane and methanol on transition metal surfaces, *J. Am. Chem. Soc.*, 2014, **136**, 14107-14113.
6. X. She, Y. Wang, H. Xu, S. Chi Edman Tsang and S. Ping Lau, Challenges and Opportunities in Electrocatalytic CO_2 Reduction to Chemicals and Fuels, *Angew. Chem. Int. Ed.*, 2022, **61**, e202211396-e202211396.
7. K. Yang, R. Kas, W. A. Smith and T. Burdyny, Role of the Carbon-Based Gas Diffusion Layer on Flooding in a Gas Diffusion Electrode Cell for Electrochemical CO_2 Reduction, *ACS Energy Lett.*, 2021, **6**, 33-40.
8. X. Jing, F. Li and Y. Wang, Assessing the economic potential of large-scale carbonate-formation-free CO_2 electrolysis, *Catal. Sci. Technol.*, 2022, **12**, 2912-2919.
9. J.-J. Velasco-Vélez, C.-H. Chuang, D. Gao, Q. Zhu, D. Ivanov, H. S. Jeon, R. Arrigo, R. V. Mom, E. Stotz, H.-L. Wu, T. E. Jones, B. Roldan Cuenya, A. Knop-Gericke and R. Schlögl, On the Activity/Selectivity and Phase Stability of Thermally Grown Copper Oxides during the Electrocatalytic Reduction of CO_2, *ACS Catal.*, 2020, **10**, 11510-11518.
10. Q. Li, Y. Zhang, L. Shi, M. Wu, Y. Ouyang and J. Wang, Dynamic structure change of Cu nanoparticles on carbon supports for CO_2 electro-reduction toward multicarbon products, *InfoMat*, 2021, **3**, 1285-1294.
11. S. H. Lee, J. C. Lin, M. Farmand, A. T. Landers, J. T. Feaster, J. E. Avilés Acosta, J. W. Beeman, Y. Ye, J. Yano, A. Mehta, R. C. Davis, T. F. Jaramillo, C. Hahn and W. S. Drisdell, Oxidation State and Surface Reconstruction of Cu under CO_2 Reduction Conditions from In Situ X-ray Characterization, *J. Am. Chem. Soc.*, 2021, **143**, 588-592.
12. X.-M. Hu, H. H. Hval, E. T. Bjerglund, K. J. Dalgaard, M. R. Madsen, M.-M. Pohl, E. Welter, P. Lamagni, K. B. Buhl, M. Bremholm, M. Beller, S. U. Pedersen, T. Skrydstrup and K. Daasbjerg, Selective CO_2 Reduction to CO in Water using Earth-

Abundant Metal and Nitrogen-Doped Carbon Electrocatalysts, *ACS Catal.*, 2018, **8**, 6255-6264.

13. S. Vijay, W. Ju, S. Brückner, S.-C. Tsang, P. Strasser and K. Chan, Unified mechanistic understanding of CO_2 reduction to CO on transition metal and single atom catalysts, *Nat. Catal.*, 2021, **4**, 1024-1031.
14. G. Marcandalli, A. Goyal and M. T. M. Koper, Electrolyte Effects on the Faradaic Efficiency of CO_2 Reduction to CO on a Gold Electrode, *ACS Catal.*, 2021, **11**, 4936-4945.
15. L. Fan, C. Xia, P. Zhu, Y. Lu and H. Wang, Electrochemical CO_2 reduction to high-concentration pure formic acid solutions in an all-solid-state reactor, *Nat. Commun.*, 2020, **11**, 3633.
16. F. P. García de Arquer, O. S. Bushuyev, P. De Luna, C. T. Dinh, A. Seifitokaldani, M. I. Saidaminov, C. S. Tan, L. N. Quan, A. Proppe, M. G. Kibria, S. O. Kelley, D. Sinton and E. H. Sargent, 2D Metal Oxyhalide-Derived Catalysts for Efficient CO_2 Electroreduction, *Adv. Mater.*, 2018, **30**, 1802858-1802858.
17. T. Kim, A. Kargar, Y. Luo, R. Mohammed, E. Martinez-Loran, A. Ganapathi, P. Shah and D. P. Fenning, Enhancing C_2–C_3 Production from CO_2 on Copper Electrocatalysts via a Potential-Dependent Mesostructure, *ACS Appl. Energy Mater.*, 2018, **1**, 1965-1972.
18. D. Kim, C. S. Kley, Y. Li and P. Yang, Copper nanoparticle ensembles for selective electroreduction of CO_2 to C_2-C_3 products, *Proc. Natl. Acad. Sci. U. S. A.*, 2017, **114**, 10560-10565.
19. G. Horányi, Heterogeneous catalysis and electrocatalysis, *Catal. Today*, 1994, **19**, 285-311.
20. J. Wang, F. Xu, H. Jin, Y. Chen and Y. Wang, Non-Noble Metal-based Carbon Composites in Hydrogen Evolution Reaction: Fundamentals to Applications, *Adv. Mater.*, 2017, **29**, 1605838.
21. K. F. L. Hagesteijn, S. Jiang and B. P. Ladewig, A review of the synthesis and characterization of anion exchange membranes, *J. Mater. Sci.*, 2018, **53**, 11131-11150.
22. H. Yoshitake, K. Takahashi and K.-i. Ota, Electrochemical reduction of CO_2 on hydrogen-enriched and hydrogen-depleted surfaces, *J. Chem. Soc., Faraday Trans.*, 1994, **90**, 155-159.

23. Y. Wang, P. Han, X. Lv, L. Zhang and G. Zheng, Defect and Interface Engineering for Aqueous Electrocatalytic CO_2 Reduction, *Joule*, 2018, **2**, 2551-2582.
24. L. Liu and H. Xiao, Inverted Region in Electrochemical Reduction of CO2 Induced by Potential-Dependent Pauli Repulsion, *J. Am. Chem. Soc.*, 2023, **145**, 14267-14275.
25. E. E. Benson, C. P. Kubiak, A. J. Sathrum and J. M. Smieja, Electrocatalytic and homogeneous approaches to conversion of CO_2 to liquid fuels, *Chem. Soc. Rev.*, 2009, **38**, 89-99.
26. A. S. Varela, The importance of pH in controlling the selectivity of the electrochemical CO_2 reduction, *Curr. Opin. Green Sustain.*, 2020, **26**, 100371.
27. C. W. Li and M. W. Kanan, CO_2 Reduction at Low Overpotential on Cu Electrodes Resulting from the Reduction of Thick Cu_2O Films, *J. Am. Chem. Soc.*, 2012, **134**, 7231-7234.
28. X. Lu, C. Zhu, Z. Wu, J. Xuan, J. S. Francisco and H. Wang, In Situ Observation of the pH Gradient near the Gas Diffusion Electrode of CO_2 Reduction in Alkaline Electrolyte, *J. Am. Chem. Soc.*, 2020, **142**, 15438-15444.
29. D. G. Park, J. W. Choi, H. Chun, H. S. Jang, H. Lee, W. H. Choi, B. C. Moon, K.-H. Kim, M. G. Kim, K. M. Choi, B. Han and J. K. Kang, Increasing CO Binding Energy and Defects by Preserving Cu Oxidation State via O_2-Plasma-Assisted N Doping on CuO Enables High C_{2+} Selectivity and Long-Term Stability in Electrochemical CO_2 Reduction, *ACS Catal.*, 2023, **13**, 9222-9233.
30. L. Fan, C. Xia, F. Yang, J. Wang, H. Wang and Y. Lu, Strategies in catalysts and electrolyzer design for electrochemical CO_2 reduction toward C_{2+} products, *Sci. Adv.*, 2020, **6**, eaay3111.
31. C.-T. Dinh, T. Burdyny, M. G. Kibria, A. Seifitokaldani, C. M. Gabardo, F. P. García de Arquer, A. Kiani, J. P. Edwards, P. De Luna, O. S. Bushuyev, C. Zou, R. Quintero-Bermudez, Y. Pang, D. Sinton and E. H. Sargent, CO_2 electroreduction to ethylene via hydroxide-mediated copper catalysis at an abrupt interface, *Science*, 2018, **360**, 783-787.
32. J. Feng, L. Wu, S. Liu, L. Xu, X. Song, L. Zhang, Q. Zhu, X. Kang, X. Sun and B. Han, Improving CO_2-to-C_{2+} Product Electroreduction Efficiency via Atomic Lanthanide Dopant-Induced Tensile-Strained CuO_x Catalysts, *J. Am. Chem. Soc.*, 2023, **145**, 9857-9866.

33. Q. Wu, R. Du, P. Wang, G. I. N. Waterhouse, J. Li, Y. Qiu, K. Yan, Y. Zhao, W.-W. Zhao, H.-J. Tsai, M.-C. Chen, S.-F. Hung, X. Wang and G. Chen, Nanograin-Boundary-Abundant Cu_2O-Cu Nanocubes with High C_{2+} Selectivity and Good Stability during Electrochemical CO_2 Reduction at a Current Density of 500 mA/cm^2, *ACS Nano*, 2023, **17**, 12884-12894.
34. T. H. M. Pham, J. Zhang, M. Li, T.-H. Shen, Y. Ko, V. Tileli, W. Luo and A. Züttel, Enhanced Electrocatalytic CO_2 Reduction to C_{2+} Products by Adjusting the Local Reaction Environment with Polymer Binders, *Adv. Energy Mater.*, 2022, **12**, 2103663.
35. Y. Jiang, X. Wang, D. Duan, C. He, J. Ma, W. Zhang, H. Liu, R. Long, Z. Li, T. Kong, X. J. Loh, L. Song, E. Ye and Y. Xiong, Structural Reconstruction of Cu_2O Superparticles toward Electrocatalytic CO_2 Reduction with High C_{2+} Products Selectivity, *Adv. Sci.*, 2022, **9**, 2105292.
36. P. Wang, H. Yang, Y. Xu, X. Huang, J. Wang, M. Zhong, T. Cheng and Q. Shao, Synergized Cu/Pb Core/Shell Electrocatalyst for High-Efficiency CO_2 Reduction to C_{2+} Liquids, *ACS Nano*, 2021, **15**, 1039-1047.
37. A. J. Bard and L. R. Faulkner, *Electrochemical Methods: Fundamentals and Applications*, Wiley, 2nd edition., 2001.
38. A. A. Peterson, F. Abild-Pedersen, F. Studt, J. Rossmeisl and J. K. Nørskov, How copper catalyzes the electroreduction of carbon dioxide into hydrocarbon fuels, *Energy Environ. Sci.*, 2010, **3**, 1311-1315.
39. H. Li, P. Wei, D. Gao and G. Wang, In situ Raman spectroscopy studies for electrochemical CO_2 reduction over Cu catalysts, *Curr. Opin. Green Sustain.*, 2022, **34**, 100589.
40. C. Shi, K. Chan, J. S. Yoo and J. K. Nørskov, Barriers of Electrochemical CO_2 Reduction on Transition Metals, *Org. Process Res. Dev.*, 2016, **20**, 1424-1430.
41. H. Ren, M. Kovalev, Z. Weng, M. Z. Muhamad, H. Ma, Y. Sheng, L. Sun, J. Wang, S. Rihm, W. Yang, A. A. Lapkin and J. W. Ager, Operando proton-transfer-reaction time-of-flight mass spectrometry of carbon dioxide reduction electrocatalysis, *Nat. Catal.*, 2022, **5**, 1169-1179.
42. A. Bagger, L. Arnarson, M. H. Hansen, E. Spohr and J. Rossmeisl, Electrochemical CO Reduction: A Property of the Electrochemical Interface, *J. Am. Chem. Soc.*, 2019, **141**, 1506-1514.

43. L. Wang, D. C. Higgins, Y. Ji, C. G. Morales-Guio, K. Chan, C. Hahn and T. F. Jaramillo, Selective reduction of CO to acetaldehyde with CuAg electrocatalysts, *Proc. Natl. Acad. Sci.*, 2020, **117**, 12572-12575.
44. F. Calle-Vallejo and M. T. M. Koper, Theoretical Considerations on the Electroreduction of CO to C_2 Species on Cu(100) Electrodes, *Angew. Chem. Int. Ed.*, 2013, **52**, 7282-7285.
45. J. H. Montoya, A. A. Peterson and J. K. Nørskov, Insights into C-C Coupling in CO_2 Electroreduction on Copper Electrodes, *ChemCatChem*, 2013, **5**, 737-742.
46. J. H. Montoya, C. Shi, K. Chan and J. K. Nørskov, Theoretical Insights into a CO Dimerization Mechanism in CO_2 Electroreduction, *The Journal of Physical Chemistry Letters*, 2015, **6**, 2032-2037.
47. Y. Kim, S. Park, S.-J. Shin, W. Choi, B. K. Min, H. Kim, W. Kim and Y. J. Hwang, Time-resolved observation of C–C coupling intermediates on Cu electrodes for selective electrochemical CO_2 reduction, *Energy Environ. Sci.*, 2020, **13**, 4301-4311.
48. H. Xiao, T. Cheng, W. A. Goddard, III and R. Sundararaman, Mechanistic Explanation of the pH Dependence and Onset Potentials for Hydrocarbon Products from Electrochemical Reduction of CO on Cu (111), *J. Am. Chem. Soc.*, 2016, **138**, 483-486.
49. A. J. Garza, A. T. Bell and M. Head-Gordon, Mechanism of CO2 Reduction at Copper Surfaces: Pathways to C_2 Products, *ACS Catal.*, 2018, **8**, 1490-1499.
50. B. Pan, J. Fan, J. Zhang, Y. Luo, C. Shen, C. Wang, Y. Wang and Y. Li, Close to 90% Single-Pass Conversion Efficiency for CO_2 Electroreduction in an Acid-Fed Membrane Electrode Assembly, *ACS Energy Lett.*, 2022, **7**, 4224-4231.
51. Y. Guo, H. Yang, X. Zhou, K. Liu, C. Zhang, Z. Zhou, C. Wang and W. Lin, Electrocatalytic reduction of CO_2 to CO with 100% faradaic efficiency by using pyrolyzed zeolitic imidazolate frameworks supported on carbon nanotube networks, *J. Mater. Chem. A*, 2017, **5**, 24867-24873.
52. J.-R. Huang, X.-F. Qiu, Z.-H. Zhao, H.-L. Zhu, Y.-C. Liu, W. Shi, P.-Q. Liao and X.-M. Chen, Single-Product Faradaic Efficiency for Electrocatalytic of CO_2 to CO at Current Density Larger than 1.2 A cm^{-2} in Neutral Aqueous Solution by a Single-Atom Nanozyme, *Angew. Chem. Int. Ed.*, 2022, **61**, e202210985.
53. Q. Wang, Y. Wu, C. Zhu, R. Xiong, Y. Deng, X. Wang, C. Wu and H. Yu, Sn nanoparticles deposited onto a gas diffusion layer via impregnation-electroreduction

for enhanced CO_2 electroreduction to formate, *Electrochim. Acta*, 2020, DOI: https://doi.org/10.1016/j.electacta.2020.137662, 137662-137662.

54. A. Guan, Z. Chen, Y. Quan, C. Peng, Z. Wang, T.-K. Sham, C. Yang, Y. Ji, L. Qian, X. Xu and G. Zheng, Boosting CO_2 Electroreduction to CH4 via Tuning Neighboring Single-Copper Sites, *ACS Energy Lett.*, 2020, **5**, 1044-1053.
55. Y. Zhang, Q. Zhou, Z.-F. Qiu, X.-Y. Zhang, J.-Q. Chen, Y. Zhao, F. Gong and W.-Y. Sun, Tailoring Coordination Microenvironment of Cu(I) in Metal–Organic Frameworks for Enhancing Electroreduction of CO_2 to CH_4, *Adv. Funct. Mater.*, 2022, **32**, 2203677.
56. B. H. Davis, Fischer–Tropsch synthesis: current mechanism and futuristic needs, *Fuel Process. Technol.*, 2001, **71**, 157-166.
57. H. Schulz, Short history and present trends of Fischer–Tropsch synthesis, *Appl. Catal., A*, 1999, **186**, 3-12.
58. B. Qin, Y. Li, H. Fu, H. Wang, S. Chen, Z. Liu and F. Peng, Electrochemical Reduction of CO_2 into Tunable Syngas Production by Regulating the Crystal Facets of Earth-Abundant Zn Catalyst, *ACS Appl. Mater. Interfaces*, 2018, **10**, 20530-20539.
59. J. Zhao, J. Deng, J. Han, S. Imhanria, K. Chen and W. Wang, Effective tunable syngas generation via CO_2 reduction reaction by non-precious Fe-N-C electrocatalyst, *Chem. Eng. J.*, 2020, **389**, 124323.
60. W. Luo, J. Zhang, M. Li and A. Züttel, Boosting CO Production in Electrocatalytic CO_2 Reduction on Highly Porous Zn Catalysts, *ACS Catal.*, 2019, **9**, 3783-3791.
61. Q. Lu, J. Rosen, Y. Zhou, G. S. Hutchings, Y. C. Kimmel, J. G. Chen and F. Jiao, A selective and efficient electrocatalyst for carbon dioxide reduction, *Nat. Commun.*, 2014, **5**, 3242.
62. D. H. Won, H. Shin, J. Koh, J. Chung, H. S. Lee, H. Kim and S. I. Woo, Highly Efficient, Selective, and Stable CO_2 Electroreduction on a Hexagonal Zn Catalyst, *Angew. Chem. Int. Ed.*, 2016, **55**, 9297-9300.
63. E. L. Clark, S. Ringe, M. Tang, A. Walton, C. Hahn, T. F. Jaramillo, K. Chan and A. T. Bell, Influence of Atomic Surface Structure on the Activity of Ag for the Electrochemical Reduction of CO_2 to CO, *ACS Catal.*, 2019, **9**, 4006-4014.
64. M. Liu, Y. Pang, B. Zhang, P. De Luna, O. Voznyy, J. Xu, X. Zheng, C. T. Dinh, F. Fan, C. Cao, F. P. G. de Arquer, T. S. Safaei, A. Mepham, A. Klinkova, E. Kumacheva, T. Filleter, D. Sinton, S. O. Kelley and E. H. Sargent, Enhanced

electrocatalytic CO_2 reduction via field-induced reagent concentration, *Nature*, 2016, **537**, 382-386.

65. R. G. Mariano, K. McKelvey, H. S. White and M. W. Kanan, Selective increase in CO_2 electroreduction activity at grain-boundary surface terminations, *Science*, 2017, **358**, 1187-1192.
66. R. G. Mariano, M. Kang, O. J. Wahab, I. J. McPherson, J. A. Rabinowitz, P. R. Unwin and M. W. Kanan, Microstructural origin of locally enhanced CO_2 electroreduction activity on gold, *Nat. Mater.*, 2021, **20**, 1000-1006.
67. J. Gu, C.-S. Hsu, L. Bai, H. M. Chen and X. Hu, Atomically dispersed Fe^{3+} sites catalyze efficient CO_2 electroreduction to CO, *Science*, 2019, **364**, 1091-1094.
68. C. Costentin, S. Drouet, M. Robert and J.-M. Savéant, A Local Proton Source Enhances CO_2 Electroreduction to CO by a Molecular Fe Catalyst, *Science*, 2012, **338**, 90-94.
69. T. Abe, T. Yoshida, S. Tokita, F. Taguchi, H. Imaya and M. Kaneko, Factors affecting selective electrocatalytic CO_2 reduction with cobalt phthalocyanine incorporated in a polyvinylpyridine membrane coated on a graphite electrode, *J. Electroanal. Chem.*, 1996, **412**, 125-132.
70. X. Wang, Z.-F. Cai, Y.-Q. Wang, Y.-C. Feng, H.-J. Yan, D. Wang and L.-J. Wan, In Situ Scanning Tunneling Microscopy of Cobalt-Phthalocyanine-Catalyzed CO_2 Reduction Reaction, *Angew. Chem. Int. Ed.*, 2020, **59**, 16098-16103.
71. Y. Zheng, P. Cheng, J. Xu, J. Han, D. Wang, C. Hao, H. R. Alanagh, C. Long, X. Shi and Z. Tang, MOF-derived nitrogen-doped nanoporous carbon for electroreduction of CO_2 to CO: the calcining temperature effect and the mechanism, *Nanoscale*, 2019, **11**, 4911-4917.
72. C. Yan, H. Li, Y. Ye, H. Wu, F. Cai, R. Si, J. Xiao, S. Miao, S. Xie, F. Yang, Y. Li, G. Wang and X. Bao, Coordinatively unsaturated nickel–nitrogen sites towards selective and high-rate CO_2 electroreduction, *Energy Environ. Sci.*, 2018, **11**, 1204-1210.
73. Y. Wu, Z. Jiang, X. Lu, Y. Liang and H. Wang, Domino electroreduction of CO_2 to methanol on a molecular catalyst, *Nature*, 2019, **575**, 639-642.
74. T. Zheng, K. Jiang, N. Ta, Y. Hu, J. Zeng, J. Liu and H. Wang, Large-Scale and Highly Selective CO_2 Electrocatalytic Reduction on Nickel Single-Atom Catalyst, *Joule*, 2019, **3**, 265-278.

75. J. Eppinger and K.-W. Huang, Formic Acid as a Hydrogen Energy Carrier, *ACS Energy Lett.*, 2017, **2**, 188-195.
76. D. Tan, W. Lee, K. T. Park, Y. E. Jeon, J. Hong, Y. N. Ko and Y. E. Kim, Promoting CO_2 reduction to formate selectivity on indium-doped tin oxide nanowires, *Appl. Surf. Sci.*, 2023, **613**, 155944.
77. X. Zheng, P. De Luna, F. P. García de Arquer, B. Zhang, N. Becknell, M. B. Ross, Y. Li, M. N. Banis, Y. Li, M. Liu, O. Voznyy, C. T. Dinh, T. Zhuang, P. Stadler, Y. Cui, X. Du, P. Yang and E. H. Sargent, Sulfur-Modulated Tin Sites Enable Highly Selective Electrochemical Reduction of CO_2 to Formate, *Joule*, 2017, **1**, 794-805.
78. Y. Chen and M. W. Kanan, Tin Oxide Dependence of the CO_2 Reduction Efficiency on Tin Electrodes and Enhanced Activity for Tin/Tin Oxide Thin-Film Catalysts, *J. Am. Chem. Soc.*, 2012, **134**, 1986-1989.
79. C. Xia, P. Zhu, Q. Jiang, Y. Pan, W. Liang, E. Stavitski, H. N. Alshareef and H. Wang, Continuous production of pure liquid fuel solutions via electrocatalytic CO_2 reduction using solid-electrolyte devices, *Nat. Energy*, 2019, **4**, 776-785.
80. S. Kim, W. J. Dong, S. Gim, W. Sohn, J. Y. Park, C. J. Yoo, H. W. Jang and J.-L. Lee, Shape-controlled bismuth nanoflakes as highly selective catalysts for electrochemical carbon dioxide reduction to formate, *Nano Energy*, 2017, **39**, 44-52.
81. J. H. Koh, D. H. Won, T. Eom, N.-K. Kim, K. D. Jung, H. Kim, Y. J. Hwang and B. K. Min, Facile CO_2 Electro-Reduction to Formate via Oxygen Bidentate Intermediate Stabilized by High-Index Planes of Bi Dendrite Catalyst, *ACS Catal.*, 2017, **7**, 5071-5077.
82. W. Zhu, L. Zhang, P. Yang, C. Hu, Z. Luo, X. Chang, Z.-J. Zhao and J. Gong, Low-Coordinated Edge Sites on Ultrathin Palladium Nanosheets Boost Carbon Dioxide Electroreduction Performance, *Angew. Chem. Int. Ed.*, 2018, **57**, 11544-11548.
83. R. Kortlever, I. Peters, S. Koper and M. T. M. Koper, Electrochemical CO_2 Reduction to Formic Acid at Low Overpotential and with High Faradaic Efficiency on Carbon-Supported Bimetallic Pd–Pt Nanoparticles, *ACS Catal.*, 2015, **5**, 3916-3923.
84. Y. Li, F. Cui, M. B. Ross, D. Kim, Y. Sun and P. Yang, Structure-Sensitive CO_2 Electroreduction to Hydrocarbons on Ultrathin 5-fold Twinned Copper Nanowires, *Nano Lett.*, 2017, **17**, 1312-1317.

85. Y. Wang, Z. Chen, P. Han, Y. Du, Z. Gu, X. Xu and G. Zheng, Single-Atomic Cu with Multiple Oxygen Vacancies on Ceria for Electrocatalytic CO_2 Reduction to CH4, *ACS Catal.*, 2018, **8**, 7113-7119.
86. S. Chen, Y. Su, P. Deng, R. Qi, J. Zhu, J. Chen, Z. Wang, L. Zhou, X. Guo and B. Y. Xia, Highly Selective Carbon Dioxide Electroreduction on Structure-Evolved Copper Perovskite Oxide toward Methane Production, *ACS Catal.*, 2020, **10**, 4640-4646.
87. L. Han, S. Song, M. Liu, S. Yao, Z. Liang, H. Cheng, Z. Ren, W. Liu, R. Lin, G. Qi, X. Liu, Q. Wu, J. Luo and H. L. Xin, Stable and Efficient Single-Atom Zn Catalyst for CO_2 Reduction to CH4, *J. Am. Chem. Soc.*, 2020, **142**, 12563-12567.
88. L. Lu, X. Sun, J. Ma, D. Yang, H. Wu, B. Zhang, J. Zhang and B. Han, Highly Efficient Electroreduction of CO_2 to Methanol on Palladium–Copper Bimetallic Aerogels, *Angew. Chem. Int. Ed.*, 2018, **57**, 14149-14153.
89. D. Yang, Q. Zhu, C. Chen, H. Liu, Z. Liu, Z. Zhao, X. Zhang, S. Liu and B. Han, Selective electroreduction of carbon dioxide to methanol on copper selenide nanocatalysts, *Nat. Commun.*, 2019, **10**, 677.
90. H. Yoshio, K. Katsuhei, M. Akira and S. Shin, PRODUCTION OF METHANE AND ETHYLENE IN ELECTROCHEMICAL REDUCTION OF CARBON DIOXIDE AT COPPER ELECTRODE IN AQUEOUS HYDROGENCARBONATE SOLUTION, *Chem. Lett.*, 1986, **15**, 897-898.
91. N. Martić, C. Reller, C. Macauley, M. Löffler, B. Schmid, D. Reinisch, E. Volkova, A. Maltenberger, A. Rucki, K. J. J. Mayrhofer and G. Schmid, Paramelaconite-Enriched Copper-Based Material as an Efficient and Robust Catalyst for Electrochemical Carbon Dioxide Reduction, *Adv. Energy Mater.*, 2019, **9**, 1901228.
92. Y. Lum and J. W. Ager, Stability of Residual Oxides in Oxide-Derived Copper Catalysts for Electrochemical CO_2 Reduction Investigated with ^{18}O Labeling, *Angew. Chem. Int. Ed.*, 2018, **57**, 551-554.
93. Y. Zhou, F. Che, M. Liu, C. Zou, Z. Liang, P. De Luna, H. Yuan, J. Li, Z. Wang, H. Xie, H. Li, P. Chen, E. Bladt, R. Quintero-Bermudez, T.-K. Sham, S. Bals, J. Hofkens, D. Sinton, G. Chen and E. H. Sargent, Dopant-induced electron localization drives CO_2 reduction to C_2 hydrocarbons, *Nat. Chem.*, 2018, **10**, 974-980.
94. Z.-Q. Liang, T.-T. Zhuang, A. Seifitokaldani, J. Li, C.-W. Huang, C.-S. Tan, Y. Li, P. De Luna, C. T. Dinh, Y. Hu, Q. Xiao, P.-L. Hsieh, Y. Wang, F. Li, R. Quintero-

Bermudez, Y. Zhou, P. Chen, Y. Pang, S.-C. Lo, L.-J. Chen, H. Tan, Z. Xu, S. Zhao, D. Sinton and E. H. Sargent, Copper-on-nitride enhances the stable electrosynthesis of multi-carbon products from CO_2, *Nat. Commun.*, 2018, **9**, 3828.

95. W. Ma, S. Xie, T. Liu, Q. Fan, J. Ye, F. Sun, Z. Jiang, Q. Zhang, J. Cheng and Y. Wang, Electrocatalytic reduction of CO_2 to ethylene and ethanol through hydrogen-assisted C–C coupling over fluorine-modified copper, *Nat. Catal.*, 2020, **3**, 478-487.
96. S. Ma, M. Sadakiyo, M. Heima, R. Luo, R. T. Haasch, J. I. Gold, M. Yamauchi and P. J. A. Kenis, Electroreduction of Carbon Dioxide to Hydrocarbons Using Bimetallic Cu–Pd Catalysts with Different Mixing Patterns, *J. Am. Chem. Soc.*, 2017, **139**, 47-50.
97. M. Zhong, K. Tran, Y. Min, C. Wang, Z. Wang, C.-T. Dinh, P. De Luna, Z. Yu, A. S. Rasouli, P. Brodersen, S. Sun, O. Voznyy, C.-S. Tan, M. Askerka, F. Che, M. Liu, A. Seifitokaldani, Y. Pang, S.-C. Lo, A. Ip, Z. Ulissi and E. H. Sargent, Accelerated discovery of CO_2 electrocatalysts using active machine learning, *Nature*, 2020, **581**, 178-183.
98. U. O. Nwabara, A. D. Hernandez, D. A. Henckel, X. Chen, E. R. Cofell, M. P. De-Heer, S. Verma, A. A. Gewirth and P. J. A. Kenis, Binder-Focused Approaches to Improve the Stability of Cathodes for CO_2 Electroreduction, *ACS Appl. Energy Mater.*, 2021, **4**, 5175-5186.
99. F. Li, A. Thevenon, A. Rosas-Hernández, Z. Wang, Y. Li, C. M. Gabardo, A. Ozden, C. T. Dinh, J. Li, Y. Wang, J. P. Edwards, Y. Xu, C. McCallum, L. Tao, Z.-Q. Liang, M. Luo, X. Wang, H. Li, C. P. O'Brien, C.-S. Tan, D.-H. Nam, R. Quintero-Bermudez, T.-T. Zhuang, Y. C. Li, Z. Han, R. D. Britt, D. Sinton, T. Agapie, J. C. Peters and E. H. Sargent, Molecular tuning of CO_2-to-ethylene conversion, *Nature*, 2020, **577**, 509-513.
100. Z. Liu, X. Lv, S. Kong, M. Liu, K. Liu, J. Zhang, B. Wu, Q. Zhang, Y. Tang, L. Qian, L. Zhang and G. Zheng, Interfacial Water Tuning by Intermolecular Spacing for Stable CO_2 Electroreduction to C2+ Products, *Angew. Chem. Int. Ed.*, 2023, e202309319.
101. M. Fan, J. E. Huang, R. K. Miao, Y. Mao, P. Ou, F. Li, X.-Y. Li, Y. Cao, Z. Zhang, J. Zhang, Y. Yan, A. Ozden, W. Ni, Y. Wang, Y. Zhao, Z. Chen, B. Khatir, C. P. O'Brien, Y. Xu, Y. C. Xiao, G. I. N. Waterhouse, K. Golovin, Z. Wang, E. H.

Sargent and D. Sinton, Cationic-group-functionalized electrocatalysts enable stable acidic CO_2 electrolysis, *Nat. Catal.*, 2023, DOI: 10.1038/s41929-023-01003-5.

102. Y. Hori, R. Takahashi, Y. Yoshinami and A. Murata, Electrochemical Reduction of CO at a Copper Electrode, *J. Phys. Chem. B*, 1997, **101**, 7075-7081.
103. Y. Wang, B. Li, B. Xue, N. Libretto, Z. Xie, H. Shen, C. Wang, D. Raciti, N. Marinkovic, H. Zong, W. Xie, Z. Li, G. Zhou, J. Vitek, J. G. Chen, J. Miller, G. Wang and C. Wang, CO electroreduction on single-atom copper, *Science Advances*, 2023, **9**, eade3557.
104. A. Gawel, T. Jaster, D. Siegmund, J. Holzmann, H. Lohmann, E. Klemm and U.-P. Apfel, Electrochemical CO_2 reduction - The macroscopic world of electrode design, reactor concepts & economic aspects, *iScience*, 2022, **25**.
105. D. Salvatore and C. P. Berlinguette, Voltage Matters When Reducing CO2 in an Electrochemical Flow Cell, *ACS Energy Lett.*, 2020, **5**, 215-220.
106. Y. Xie, P. Ou, X. Wang, Z. Xu, Y. C. Li, Z. Wang, J. E. Huang, J. Wicks, C. McCallum, N. Wang, Y. Wang, T. Chen, B. T. W. Lo, D. Sinton, J. C. Yu, Y. Wang and E. H. Sargent, High carbon utilization in CO_2 reduction to multi-carbon products in acidic media, *Nat. Catal.*, 2022, **5**, 564-570.
107. W. Li, Z. Yin, Z. Gao, G. Wang, Z. Li, F. Wei, X. Wei, H. Peng, X. Hu, L. Xiao, J. Lu and L. Zhuang, Bifunctional ionomers for efficient co-electrolysis of CO_2 and pure water towards ethylene production at industrial-scale current densities, *Nat. Energy*, 2022, **7**, 835-843.
108. M. Sassenburg, M. Kelly, S. Subramanian, W. A. Smith and T. Burdyny, Zero-Gap Electrochemical CO_2 Reduction Cells: Challenges and Operational Strategies for Prevention of Salt Precipitation, *ACS Energy Lett.*, 2023, **8**, 321-331.
109. Y. Sone, P. Ekdunge and D. Simonsson, Proton Conductivity of Nafion 117 as Measured by a Four-Electrode AC Impedance Method, *J. Electrochem. Soc.*, 1996, **143**, 1254.
110. J. E. Huang, F. Li, A. Ozden, A. Sedighian Rasouli, F. P. García de Arquer, S. Liu, S. Zhang, M. Luo, X. Wang, Y. Lum, Y. Xu, K. Bertens, R. K. Miao, C.-T. Dinh, D. Sinton and E. H. Sargent, CO_2 electrolysis to multicarbon products in strong acid, *Science*, 2021, **372**, 1074-1078.
111. R. Pärnamäe, S. Mareev, V. Nikonenko, S. Melnikov, N. Sheldeshov, V. Zabolotskii, H. V. M. Hamelers and M. Tedesco, Bipolar membranes: A review on

principles, latest developments, and applications, *J. Membr. Sci.*, 2021, **617**, 118538.

112. L. Chen, Q. Xu, S. Z. Oener, K. Fabrizio and S. W. Boettcher, Design principles for water dissociation catalysts in high-performance bipolar membranes, *Nat. Commun.*, 2022, **13**, 3846.

Chapter 2 Characterisation Techniques and Experimental Methods

2.1 Introduction

Characterisation techniques facilitate researchers to understand the properties of materials and the reaction systems of interest. The development of advanced characterisation methods in recent years has pushed the frontiers of materials research to an unprecedented level. In the field of heterogeneous catalysis, it relies on both *ex-situ* and *in-situ* characterisation to explain the behaviours of catalysts and reaction system[1]. Monitoring the catalysts states during the reaction has become the trend of research apart from understanding the catalysts themselves individually. It becomes even more important when studying a complicated system such as the flow cell for ECR. Picturing the real-time behaviours of electrocatalysts, especially surface and interface, enables a better design and engineering of efficient catalysts and electrolysers.

In this chapter, techniques involved to complete the experiments in this thesis were introduced including their operating principles and measurement conditions, followed by the chemicals used and details of synthetic procedures of catalysts.

2.2 Characterisation Techniques

2.2.1 X-ray Diffraction

XRD is a useful tool for solid-state materials characterisation. Information of crystalline materials could be extracted from XRD patterns such as unit cell parameters, lattice constant, particle size and phase identification[2]. It takes the advantage that the interatomic distances in crystallized materials are usually comparable to the wavelength of X-ray. Therefore, the diffraction of X-ray becomes possible with the crystalline materials acting as gratings. A laboratory based XRD diffractometer consists of an X-ray source, a

monochromator, a sample holder, and a detector. X-ray could be generated from electrons at high energy level occupying the low energy vacancies created by bombarding the anode material (copper or tungsten) in the X-ray tube. The beam is then monochromated to select wavelength before shining on the sample at different incident angles.

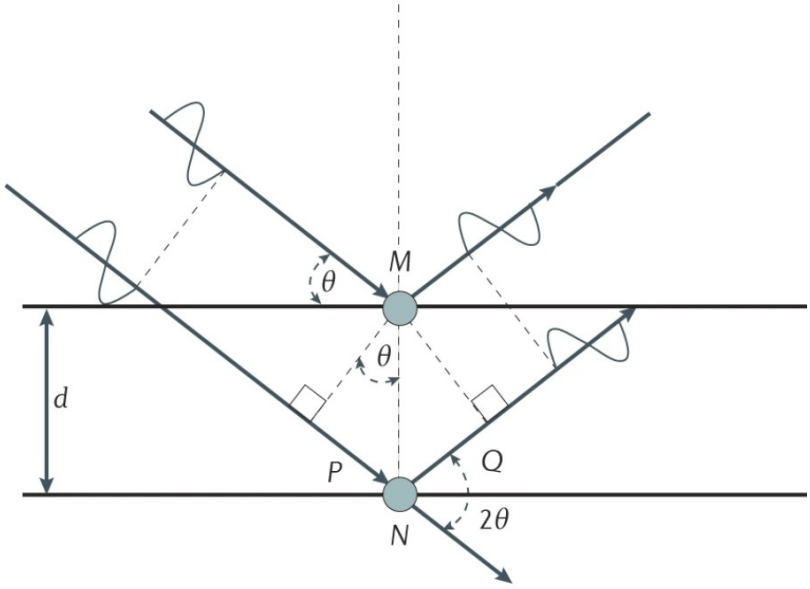


Figure 2.1 Geometry for simplified derivation of Bragg's law. Reproduced from reference[3]. Copyright 2008 Royal Society of Chemistry.

For a well-crystallized sample, constructive and destructive interference take place and produce a unique diffraction pattern, where the constructive interference increases the signal intensity forming a peak, while the destructive interference is cancelled out with each other and not shown in the pattern. The Bragg's Law (**Eq. 2.1**) describes the condition of constructive interference to be at its strongest[4]:

$$n\lambda = 2d\sin\theta \qquad \textbf{(Equation 2.1)}$$

where n is the diffraction order, λ is the wavelength of incident radiation, d is the spacing of parallel planes, and θ is the angle between incident path and scattering planes. Lattice parameters can be calculated using Miller indices (hkl). For simple cubic crystals such as Cu, Pd and MgO, the lattice vectors are orthogonal with equal length. It follows:

$$d_{hkl} = \frac{a}{\sqrt{h^2 + k^2 + l^2}} \qquad \textbf{(Equation 2.2)}$$

where d is the interlayer spacing h, k and l are Miller indices and a is the lattice parameter. For a non-cubic hexagonal crystal structure, the relation between lattice parameters and d spacing follows:

$$d_{hkl} = \frac{a}{\sqrt{\frac{4}{3}(h¿¿2 + k^2 + hk) + \frac{a^2}{c^2}l^2¿}} \qquad \textbf{(Equation 2.3)}$$

where d is the interlayer spacing h, k and l are Miller indices and a, c are lattice parameters.

While an ideal XRD pattern should have sharp and well-defined peaks when crystal planes are aligned with destructive interference at all incident angles, common cases see asymmetric peak and broadening especially in catalytic nanomaterials studied in this thesis. The decrease in domain sizes and increase in defects lead to a wide distribution of interplane spacing[5]. Scherrer equation relates the size of crystallinity with the peak broadening[6, 7]:

$$\tau = \frac{K\lambda}{\beta \cos\theta} \qquad \textbf{(Equation 2.4)}$$

where τ is the calculated particle size; K is a dimensionless shape factor (close to unity), which varies with the actual shape of the crystallite (usually ranges 0.8-1.2); λ is the wavelength of the X-ray photon; β is the peak width at full width half maximum (FWHM) in radians and θ is the Bragg angle. It is, however, uneasy to estimate the size of crystals as other aspects such as background subtraction, crystal strain and instrument settings may also affect the peak broadening.

Albeit the wide availability and the capability of structure analysis, XRD has limitations when tackling with amorphous materials and local environments (e.g., bonding, defects,

and interface). Other characterisation techniques are needed to compensate for its shortages.

2.2.2 Transmission Electron Microscopy

Optical microscope has a resolution of at most 0.2 μm, which is limited by the wavelength of visible light (380-700 nm). For modern catalysts research, this is often insufficient to identify morphologies, sizes or even lattice from imaging. Replacing visible light source with electron beams at tens of kiloelectronvolts (keV) that has orders of magnitude smaller wavelengths could improve the performance of microscope to the atomic level[8]. The Abbe's diffraction limit is determined by:

$$d = \frac{\lambda}{2 n \sin\theta} \qquad \textbf{(Equation 2.5)}$$

where d is the minimum resolvable distance, λ is the wavelength of light, n is the refraction index of the medium that light travels in, and θ is the half-angle subtended by the objective lens[9]. For example, operating at 100 keV, transmission electron microscopy (TEM) could offer a theoretical resolution of 0.004 nm, much smaller than the size of an atom.

The typical TEM measurements are operated under ultra-high vacuum (10^{-6} mbar) to reduce the collision frequency of electrons with gas molecules. Beams generated from the electron gun first pass through electromagnetic lenses which produce radially symmetric field focusing electrons at a constant focal distance. Apertures could be applied in the beam path to filter electrons scattered to high angles. The transmitted electrons then interact with the sample, and they are refocused and magnified through objective lens before projected onto a screen (**Fig. 2.2**). The imaging of TEM has two modes, i.e., bright field and dark field. When an objective aperture is inserted into the path with central beam selected, a bright field image is obtained with a bright background and dark sample

areas. In contrast, when diffracted signal is selected to pass through the aperture, a dark field image is received on the screen with bright areas showing the sample of interest. In this case, the heavier the element is (higher electron density), the brighter spot appears. Additional detectors could also be equipped with TEM, for instance, Energy Dispersion X-ray spectroscopy (EDX) which enables imaging on elemental distribution[10].

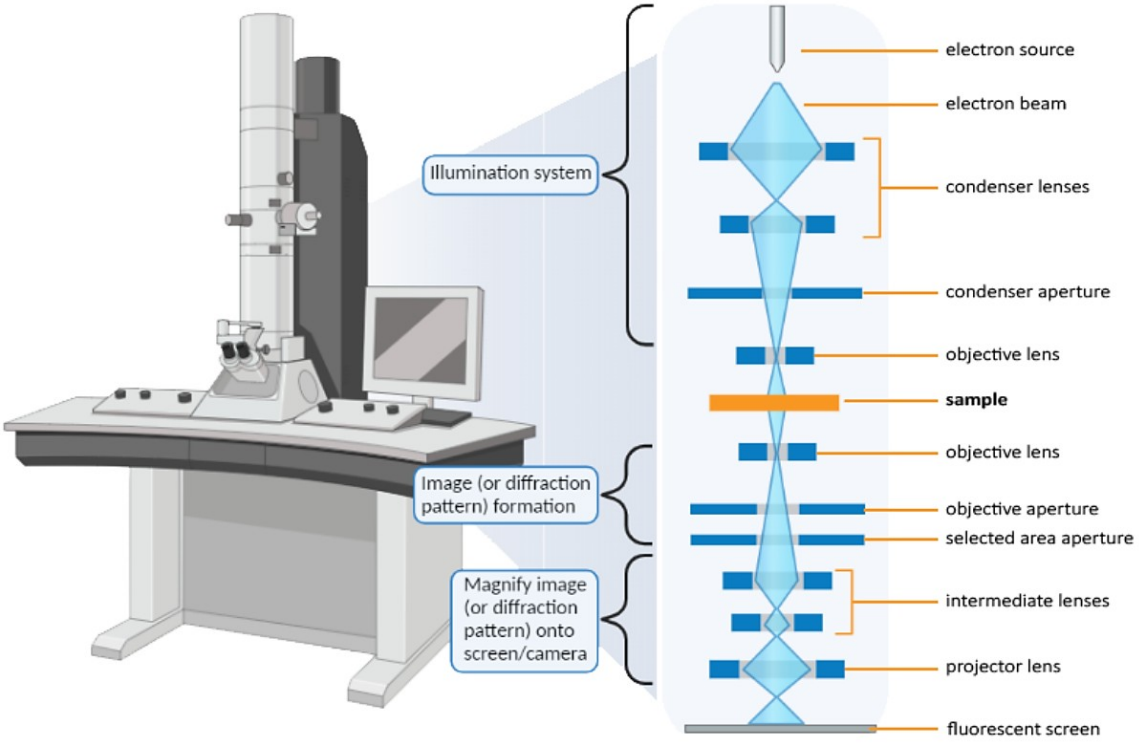


Figure 2.2 Simplified TEM scheme highlighting the major components. Reproduced from reference[11]. Copyright 2023 Nanoscience Instruments.

2.2.3 X-ray Absorption Spectroscopy

X-ray Absorption spectroscopy (XAS) has been widely used in catalysis research recently[12] as it could provide information on local environment of the targeted element regardless of the crystallinity. Unlike X-ray photoelectron spectroscopy (XPS), XAS is a bulk characterisation where the photons penetrate the materials to excite the core electrons. Depending on the principal quantum numbers (n=1, 2, or 3), the edges are named as K-, L- and M- edge, respectively. Synchrotron radiation is usually used as the

X-ray source to perform the experiments due to its tuneable energy range and intense beam. To collect the data, there are two modes depends on the experiment conditions, namely transmission and fluorescence mode (**Fig. 2.3**). The former mode allows rapid measurements and is suitable for elements with high content, for instance, supported metal/oxide materials with metal loading over 1 wt%[13]. The latter one offers higher sensitivity to elements which can be applied to diluted samples, or for *in-situ* measurements when the transmitted signals are significantly affected by the sample setup.

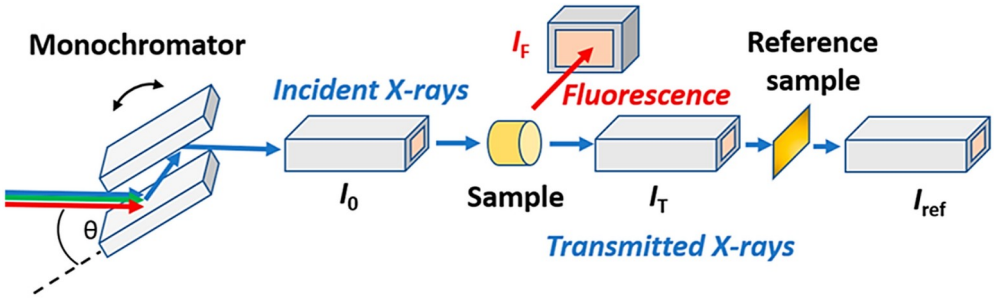


Figure 2.3 Schematics of a common setup for XAS measurements with double crystal monochromator. Reprinted with permission from reference[14]. Copyright 2020 American Chemical Society.

A typical spectrum has two main regions (**Fig. 2.4**): the X-ray absorption near-edge structure (XANES) also known as near-edge X-ray absorption fine structure (NEXAFS) including the pre-edge and the extended X-ray absorption fine structure (EXAFS). The pre-edge region is related with the transition to the lowest unoccupied states usually shown as a small shoulder peak slightly below the edge, while the XANES region with the sharp rising edge results from the core electron transition to quasi bound states. Electronic structures and the geometry of the studied elements could be obtained from this region[15]. In high kinetic energy range (about 50 eV above the absorption edge), EXAFS originates from the scattering of photoelectrons ejected from the absorbing atoms and its neighbours. The local structure such as bond length and coordination can be determined by Fourier transformation to deconvolute absorbing centre and surrounding atoms[16].

Additionally, when distance between neighbouring and absorbing atoms are close to each other, wavelet transformation could distinguish the different types of atoms by considering the contribution in the k-space together with the R-space spectra.

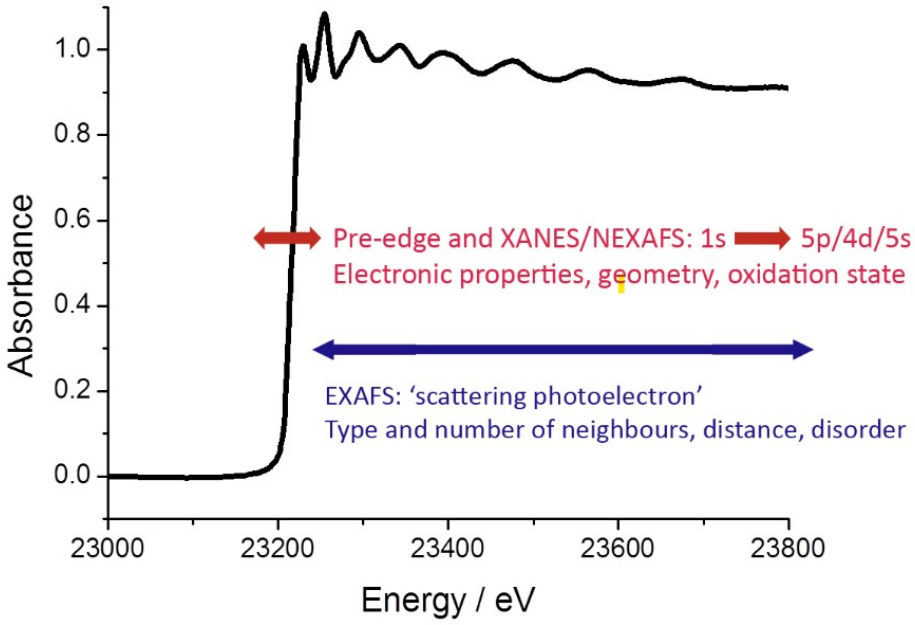


Figure 2.4 A typical normalized XAS spectrum depicting pre-edge, XANES (near-edge and edge) and EXAFS (post-edge oscillation) regions. Figure reproduced from reference[17]. Copyright 2022 Diamond Light Source.

2.2.4 Raman Spectroscopy

Raman spectroscopy provides information on vibration modes of molecules by shining a laser on a sample and observing inelastically scattered photons with energy changes compared to the incident photons (**Fig. 2.5**). It is a non-destructive characterisation method based on the interaction of light with the chemical bonds and has been used in real-time analysis of catalytical reactions[18]. Components in the sample are identified through the specific shift related to a certain vibrational mode in the molecule. Raman shift is usually expressed in wavenumbers (cm^{-1}) by the difference between the absolute wavenumbers of excitation wavelength ($1/\lambda_0$) and Raman scattered photons ($1/\lambda_1$). It is

proportional to the energy change of photons in Raman scattering and independent from the incident light.

$$\Delta \nu = \frac{1}{\lambda_0} - \frac{1}{\lambda_1} \qquad \textbf{(Equation 2.6)}$$

Raman spectroscopy is complementary to infrared spectroscopy (IR). Symmetric stretching vibrational modes with unchanged dipole moment are IR inactive, yet they could be Raman active when the molecule polarizability is changed (i.e., electron cloud of CO_2 is re-arranged during symmetric stretching, but the dipole moment remains the same). High polarizability of a molecule does not necessarily require the molecule to have a large dipole moment.

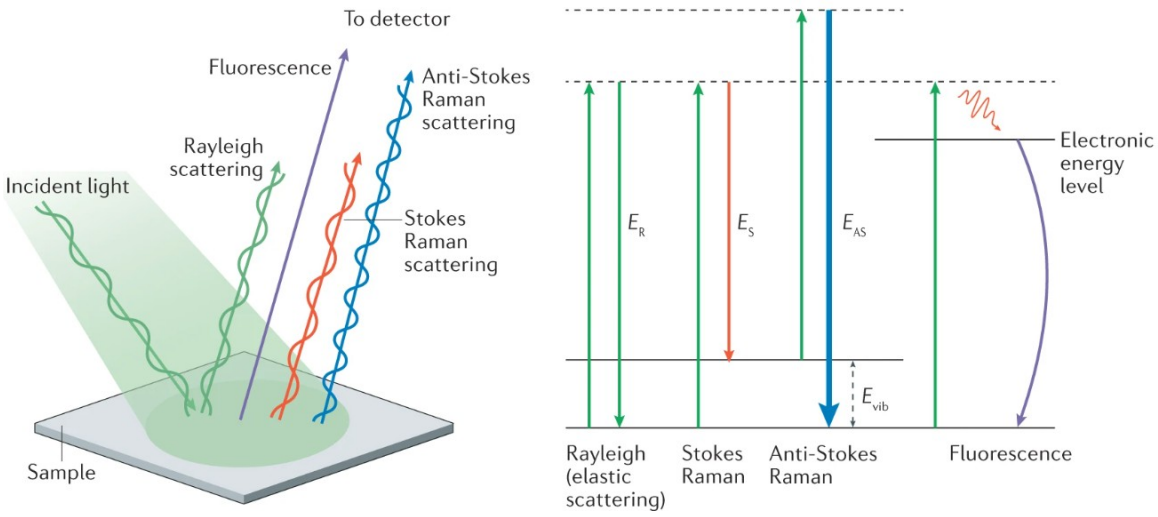


Figure 2.5 Schematic energy transitions when light illuminate on a sample. Rayleigh scattering is when light undergoes direct specular reflection with incident and scattered photons at same energy level (elastic scattering). Raman scattering contains two modes, the Stokes scattering induce constituent molecules to absorb energy from the incident light and therefore emitted photons with less energy, whereas the Anti-Stokes involves molecules that are initially vibrationally activated transferring energy to the incident light. Fluorescence takes place when molecules are excited to a higher electronic level and then relaxed to the ground state through the emission of photons of longer wavelength. Reprinted with permission from reference[19]. Copyright 2021 Springer Nature.

2.2.5 Electrochemical Techniques

Electrochemistry concerns with the relationship between electrical potential difference and chemical change. When the potential difference is the outcome of a chemical reaction, it is called a fuel cell or battery. On the contrary, when a certain reaction takes place due to the existence of the potential difference, it is named as electrolysis. The techniques applied to study these systems are similar including voltammetry, chrono analysis and impedance spectroscopy.

Voltammetry is the measurement of current when varying the potential. The linear sweep voltammetry (LSV), by its name, is applying potential linearly in time to the working electrode. Oxidation or reduction reactions can be observed in the current signal if the oxidation/reduction potential is within the scanned range. For cyclic voltammetry (CV), the potential not only ramps linearly versus time but also scans from the opposite direction returning to the initial potential to finish a complete cycle. The number of cycles can be chosen depending on the aim of the measurement. For a reversible redox couple, the species reduced by cathodic potential will be re-oxidised resulting in anodic current when the sweep direction is reversed[20]. The more reversible the couple is, the more similar the reduction and oxidation peak will be. The relation of current-potential in a simple one-electron, one-step process can be described by the Butler-Volmer equation (**Eq. 2.7**):

$$I = FAk^0 C_O^{*(1-\alpha)} C_R^{*\alpha} \left[\frac{C_O(0,t)}{C_O^*} e^{\frac{-\alpha F}{RT}\eta} - \frac{C_R(0,t)}{C_R^*} e^{\frac{(1-\alpha)F}{RT}\eta} \right] \quad \textbf{(Equation 2.7)}$$

where I is the total current; F is Faraday constant (96485 C·mol^{-1}); A is the area of electrode; k^0 is the standard electrochemical rate constant (cm·s^{-1}); η = E − E_{eq}, is the potential difference between a half reaction's reduction potential(E_{eq}) and the potential where the redox event happens (E), namely overpotential; R is the universal gas constant (8.314 J·K^{-1}·mol^{-1}); T is temperature (K); C_O and C_R refer to the concentration of the

species to be oxidized and to be reduced, respectively; *C(0,t)* is the concentration at distance zero from the surface of the electrode at time t; α is the transfer coefficient ranging from 0 to 1. The transfer coefficient depicts the symmetry of the barrier to reaction, which tend to locate at around 0.5 in most experiments[21]. Both LSV and CV are plotted as current versus potential with additional information such as scan rate and scan step. There are other types of voltammetry such as staircase voltammetry and square wave voltammetry[22], most of which follows a similar principle as CV and LSV with different potential-time patterns.

Chrono analysis employed in electrocatalysis usually include chronoamperometry and chronopotentiometry. Chronoamperometry is applying constant potential to the working electrode and recording the current over time; whereas chronopotentiometry is controlling current at constant and monitor the potential change. Operating the electrolysis cell under the selected potential/current, catalytic reactions take place accompanied by online products analysis or stability testing.

Electrochemical impedance spectroscopy (EIS) is a tool for the investigation of electrode reactions[23]. An electrochemistry reaction on the electrode-electrolyte interface consists of a series of multistep process including mass transport, charge transfer, adsorption, and desorption. These processes happen at distinct timescales in response to current/potential. EIS, as a transient analysis technique could characterise different steps based on their behaviours to the change of frequencies. Therefore, EIS has been used to evaluate battery system[24], corrosion of materials[25] and electrochemical sensors[26]. In this thesis, EIS will be used to understand the electrochemical reactions to various products in ECR for the adsorption of intermediates and charge transfer steps.

Unlike Raman or IR spectroscopy which excite the sample with light at certain wavelengths, the EIS measurements excite the electrode samples with period perturbation from small-amplitude potential or current at selected frequencies. The spectra are obtained by monitoring the response to this perturbation in the system (**Fig. 2.6**). The impedance (Z) is expressed as:

$$Z(\omega)=\frac{\widetilde{V}(\omega)}{\widetilde{I}(\omega)}=\left|\frac{\widetilde{V}(\omega)}{\widetilde{I}(\omega)}\right|\left[cos\varphi(\omega)+jsin(\omega)\right]=Z_R+jZ_I \quad \textbf{(Equation 2.8)}$$

where ω is the angular frequency defined as $\omega = 2\pi f$ in which f is frequency in Hertz, ϕ is the phase angle between the input and output signals, and the imaginary number $j=\sqrt{-1}$. The variables $\tilde{V}$ and $\tilde{I}$ are complex time-invariant numbers representing the amplitude and phase of a sinusoidal function. Z_R and Z_I are the real and imaginary part of the impedance (measured in Ohm, Ω), respectively.

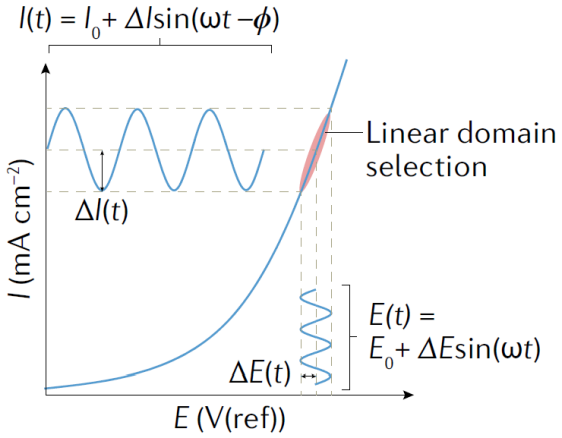


Figure 2.6 Example of electrochemical response to a ΔE perturbation. The oval marked in red is the where the response is measured. Reprinted with permission from reference[23]. Copyright 2021 Springer Nature.

Making a correct measurement of impedance is crucial of understanding the electrode process. A three-electrode system is employed enabling the study of working electrode (WE) independently from the counter electrode (CE). To further reduce the influence of counter electrode, a larger counter electrode area is usually used compared to the. In our

setup, the counter electrode has an effective working area of 4 cm^2, four times larger than the working electrode. Another advantage of using a large CE is that a more uniform current/potential distribution could be created on the WE, which improved the quality of the impedance measurements. However, frequency dispersion at high-frequency impedance response could still exist as the GDE surface itself is ununiform, plus the impedance of reference electrode (RE) tend to decrease and cause fluctuations on potential of WE. This could be avoided by eliminating frequencies larger than the characteristic frequency (f_c):

$$f_c = \frac{1}{2\pi R_e C} \qquad \textbf{(Equation 2.9)}$$

where R_e is the high-frequency ohmic resistance between the working and reference electrodes and C is the capacitance of the working electrode–electrolyte interface[27].

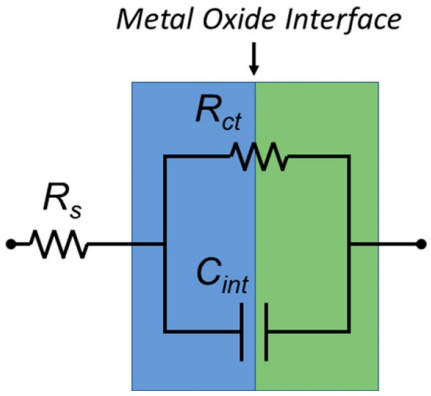


Figure. 2.7 Randles circuit describing a metal oxide interface with current flow. R_s stands for solution/electrolyte resistance, R_{ct} for charge transfer resistance and C_{int} for interfacial capacitance. Reprinted with permission from reference[28]. Copyright 2020 American Chemical Society.

To analyse the impedance data, an equivalent circuit is built that could illustrate the surface electrode process. The interfacial capacitance in **Fig. 2.7** is usually replaced by constant-phase element (CPE) in the model to depict the double-layer capacitors in real cell that do not behave ideally, defined as:

$$Z_{CPE} = \frac{1}{(j\omega)^{\alpha} Y_0} \qquad \textbf{(Equation 2.10)}$$

where Z_{CPE} is the impedance of CPE; ω is the angular frequency; α is a factor ranging from 0-1 that describes how close the behaviour of CPE is to a capacitor or resistor, when α=1, the CPE equals a capacitor. Y_0 is the capacitance. In this thesis, two R_{ct}||CPE connected in series with R_s were used as the circuit model for analysis and extraction of effective capacitance (C_{eff})[29].

$$C_{eff} = Y_0^{\frac{1}{\alpha}} \cdot \left(\frac{1}{\frac{1}{R_s} + \frac{1}{R_{ct}}}\right)^{\frac{1}{\alpha}-1} \qquad \textbf{(Equation 2.11)}$$

2.2.6 Gas Chromatography

Gas chromatography (GC) is applied to separate and analyse compounds that can be vaporized. The sample gas/liquid is first injected into a mobile phase (carrier gas) before goes through the stationary phase contained inside of separation columns. The columns are kept in the oven with controlled temperature so that the separation process remains constant for the detectors to identify the products.

To analyse the product gas component from ECR, online GC was connected to the outlet of the electrolyser. Gas products are first separated by a Porapak column with all light components (H_2, N_2, O_2, CO, and CH_4) passing through. Then a back flush to the column forces the remaining components, mostly hydrocarbons in our system, to the flame ionization detector (FID) before using an alumina plot column to separate them. The light components pass through a Shimcarbon packed column for further separation and quantified by a Dielectric-Barrier Discharge Ionization detector (BID), which has a signal-to-noise ratio 100 times higher than thermal conductivity detector (TCD)[30]. High purity He is the carrier gas, as well as the discharge flow for plasma generation in BID.

2.2.7 Mass Spectrometry

Mass spectrometry (MS)is used to measure the mass-to-charge ration of ions. The sample is first ionized then separated according to their mass-to-charge ratio by an electric or magnetic field. The detector is to count for charged particles and the resulted spectrum displays signal intensity of ions as a function of the mass-to-charge ratio (m/z). Through the mass information of the atoms or molecules and their fragments pattern, it is possible to identify the components of the sample. Two laws govern the charged particles movement: the Lorentz force law and Newton's second law in non-relativistic case. The force applied to the ions equates which gives:

$$Q(E+v\times B)=ma \qquad \textbf{(Equation 2.12)}$$

in which, Q is the charge of the ions which can be calculated to the number of elementary charges (e) with $z=Q/e$, $\boldsymbol{E}$ is the electric field, $\boldsymbol{v}\times\boldsymbol{B}$ is the cross product of velocity and magnetic field, m is the mass of the ion and $\boldsymbol{a}$ is the acceleration. Provided that the particles initial conditions are known, their motion in space and time can be determined in terms of m/Q, or more commonly termed as the dimensionless m/z, mess-to-charge ratio.

Two types of MS were involved in this thesis. First, a triple filter mass spectrometer (HPR-20) that selects the m/z ratio precisely through a radio frequency quadrupole field between four parallel rods. This spectrometer was equipped with the electron ioniser (EI) which resulted in a high level of fragments with m/z lower than the molecular ion. It was, therefore, found to be less suitable to the ECR system as the main component (>95%) in the outlet gas, CO_2, had fragments overlapping severely with the products (i.e., CH_4, C_2H_4 and CO) pattern[31]. The second type of MS applied was the PTR-TOF-MS, which uses hydronium (H_3O^+) as the reagent ion for the proton transfer reaction (PTR) and time-of-flight (TOF) analyser that accelerates the ions under the same potential and measure the

time taken to reach the detector. The PTR offers low detection limit as the reagent source has exceptionally high purity and was directly injected into the instrument. Low fragmentation can be achieved through the PTR process as a much less amount of energy is transferred during the ionization process compared with EI. However, the trade-off is that the proton affinity of molecules should be higher than that of H_2O, which indicating that molecules such as H_2, CO_2 and CH_4 cannot be ionized and then detected by the TOF analyser. The PTR-TOF-MS was kindly measured with the assistance from Dr. Hangjuan Ren, Department of Chemistry, University of Oxford.

2.2.8 X-ray Photoelectron Spectroscopy

X-ray photoelectron spectroscopy (XPS) is widely used as a powerful technique for studying chemical composition of materials and chemical states of elements. Aluminium is used as the source of the soft X-ray beam (Al Kα: 1486.7 eV), which is much lower than the copper beam source for XRD (Cu Kα: 8047.8 eV). Consequently, the penetration depth is few atomic layers, making the signal of the XPS sensitive to surface. From theoretical perspective, the XPS signal comes from measuring the kinetic energies of excited photoelectrons ejected from the surface[32]. Its theoretical relationship follows:

$$E_{binding} = h\nu - E_{kinetic} - \varphi \qquad \textbf{(Equation 2.13)}$$

where h is the Planck constant, ν is the frequency of X-ray, φ is the work function correction of a spectrometer caused by contact potential, $E_{binding}$ and $E_{kinetic}$ represent the binding energy of the excited electrons to the nucleus and the kinetic energy of the detected photoelectrons, respectively.

For a typical lab based XPS measurement, the experiment was conducted under ultra-high vacuum to avoid photoelectron colliding with gaseous molecules and protect moisture sensitive detectors. A survey scan from 0 eV to 1400 eV in binding energy is

measured to obtain chemical composition by assigning peaks to different elements. The ratio of elements can be calculated by the integrated area of peaks and the corresponding relative sensitivity factor. The oxidation states of elements are investigated by conducting high-resolution scans in a specific binding energy range, depending on the element of interest. Generally, the oxidation state difference of the same element will lead to different electron densities and thus varied binding energies. By comparing the experimental binding energies with the values in database, it is possible to obtain information on chemical states of elements.

2.3 Experimental Methods

2.3.1 Chemicals

Molybdenum(IV) sulphide (MoS_2), Copper(II) nitrate trihydrate ($Cu(NO_3)_2 \cdot 3H_2O$, 99-104%), Magnesium chloride ($MgCl_2$, >98%), Sodium hydroxide (NaOH, >98%), Potassium hydroxide (KOH, 90%), Potassium bicarbonate ($KHCO_3$, 99.7%), Potassium sulphate (K_2SO_4, >99.0), Copper(II) acetylacetonate ($Cu(acac)_2$, >99.9%), $Pd(acac)_2$, 99%), oleylamine (primary amine >98%), *N*-Methyl-2-pyrrolidinone (NMP, anhydrous, 99.5%), ethanol (>99.5%), hexane (95%), 2-propanol (isopropanol, >99.5%), were purchased from Merck. Cupric chloride dihydrate ($CuCl_2 \cdot 2H_2O$, >99.0%) was purchased from Alfa Aesar. Deionised (DI) water used for electrolyte preparation was obtained from a Purite Select Water Purification System.

The anion exchange membrane (Fumasep FAA-3-PK-75), gas diffusion electrode (carbon paper, GDE, Sigracet 39BB and Freudenberg H14C10), and Nafion® 117 membrane were purchased from FuelCellStore. The alkaline ionomer solution (5% in ethanol, Sustainion XC-1) and anion exchange membrane (Sustainion X37-50) were purchased from Dioxide Materials.

2.3.2 Synthesis of Single-layer MoS_2 and Cu Exchange

Preparation of single layer MoS_2. To prepare single layer MoS_2, *n*-butyl Lithium was used to intercalate bulk MoS_2. Typically, 6g bulk MoS_2 was added to a 150 mL round flask with a magnetic stirring bar and degas with N_2 for at least 30 mins. Then, 48 mL 1.6 M n-BuLi/hexane solution was added to the flask under the protection of N_2. The mixture was stirred at room temperature for 48-72 hrs. After the intercalation, 60 mL hexane was added to the flask and stirring for another 30 mins to dilute the unreacted n-BuLi. The products were separated and washed in hexane with centrifuging at 5000 rpm for 10-15 mins and then, dried in the oven at about 60 °C to remove the solvent. The resulted black powder was denoted as Li-MoS_2.

To exfoliate the MoS_2 into single layers, 6g Li-MoS_2 was added to 1 L DI water and sonicate for over 6 hrs. The single layer products were separated by centrifuging the solution and collecting the upper layer liquid. Concentrated HCl was added dropwise to the obtained solution until the pH value was around 5-7. Then, rest the solution in the oven at 60-70 °C allowing the single layer product to precipitate. The precipitates were collected via centrifuging and dried in the vacuum oven at 60 °C overnight. The resulted powder was denoted as s-MoS_2.

Cu^{2+} exchange with Li^+. 200 mg of dry Li-MoS_2 powder synthesized in the previous step, $Cu(NO_3)_2 \cdot 3H_2O$ (4.83 g, 0.02 mol), and anhydrous NMP (35 mL) were added to a Teflon autoclave. After stirring the mixture to form a homogeneous suspension, it was sealed in the autoclave and underwent a solvothermal process at 80 °C for 48 h. The product was washed thoroughly with NMP, isopropanol, ethanol, and water before being dried in a vacuum dryer. The obtained green powder was denoted as Cu-MoS_2.

2.3.3 Preparation of $Mg(OH)_2$ Substrates

Hydrothermal synthesis of $Mg(OH)_2$. 0.12g benzoic acid was first dissolved in 60 ml DI water by sonication. Then 2g $MgCl_2$ was added in the benzoic acid solution and stirred for 10 mins. 20 ml of 2M NaOH(aq) was then added dropwise into the previous solution and white 'gel' was obtained. The solution was then transferred into a 100ml autoclave and heated to 180 C for 24 hrs. The obtained white precipitate was washed with DI water and vacuum dried at 60-80 °C overnight. The sample was denoted as $BMg(OH)_2$.

Acetone treatment of $Mg(OH)_2$. 1g $Mg(OH)_2$ powder obtained from the previous step was added into 100ml acetone in a 250 ml round flask and kept at 65 °C for 24 hrs in oil bath with reflux. The white precipitate was then collected and dried in vacuum oven at 60 °C for 2 hrs. The sample was labelled as $AMg(OH)_2$.

2.3.4 Cu loading on MgO/$Mg(OH)_2$ Substrates

In a typical experiment, 26.4 mg $CuCl_2 \cdot 2H_2O$ was first dissolved in 500 uL DI water. Then, 100 mg chosen $Mg(OH)_2$ substrate from the previous step was added into the obtained solution and mixed well before putting into the vacuum oven at 60 °C. After drying for 2 hrs, the obtained powder was grounded and then calcined in 5% H_2/N_2 at 200 °C with a ramp rate of 2 °C/min and dwelling at 200 °C for 4. The resulted powder was denoted as 10Cu-$Mg(OH)_2$. The loading amount of Cu was decided by the weight ratio of $CuCl_2 \cdot 2H_2O$ precursor and $Mg(OH)_2$ substrate. When calcination temperature was controlled, the dwelling temperature was set to 200, 300 and 500 °C with the same ramp rate and dwelling duration. The resulted samples are denoted as 10Cu-200, 10Cu-300 and 10Cu-500, respectively. The loading amount of Cu could also be altered via the ratio of Cu precursor.

2.3.5 Synthesis of Cu Nanoparticles

A solution containing 250 mg g of $Cu(acac)_2$ and 20 mL of oleylamine (OA) first added into a 50 ml round bottom flask with reflux and degas for 10 min under N_2. The flask was then heated to 250 °C from room temperature under string. The solution was kept at this temperature for 1 hour and the turned red with metallic Cu forming on the inner wall of the flask. The red solution was collected into a 50 mL centrifuge tube and the solid was separated from the solvent via centrifuging. Hexane and isopropanol were added into the solid and centrifuge at 5000 rpm for 15 min to wash the solid twice. The collected and washed solid could either be dried under N_2 flow in the form of powder for storage in glovebox or be re-dissolved by 1:1 hexane and isopropanol for electrode preparation. The yield of copper particles is around 50 mg from a single batch of synthesis. The sample was denoted as Cu-S1. By extending the synthesis time at 250 °C to 2, 4 and 6 hours, the samples were denoted as Cu-S2, Cu-S4 and Cu-S6.

2.3.6 Synthesis of CuO_x

Copper oxalate powder was first grounded into fine powder. Then the powder was calcined in a tube furnace under N_2 flow with a ramping rate at 10 °C·min^{-1} and dwelling at 350 °C for 4 hours. The resulted product was denoted as CuO_x-N_2. Calcination under Ar or air flow in the tube furnace with the same precursor and temperature controlling program resulted in CuO_x-Ar and CuO-air, respectively.

2.3.7 Synthesis of CuPd Nanoparticles

The synthesis of Pd-doped Cu NPs follows the same procedure of Cu NPs, except the metal precursor. The duration of synthesis at 250 °C was 2 hours for all Pd-doped samples. For a nominated doping level at 2%, 5 mg $Pd(acac)_2$ and 245 mg $Cu(acac)_2$ was added into 20 ml OA. The resulted product was noted as CuPd2. For CuPd10, the metal precursor consists of 25 mg $Pd(acac)_2$ and 225 mg $Cu(acac)_2$. All procedures for

separation are same as Cu-S1 and samples are used for electrode fabrication once they are ready.



Figure 2.8 Photo of the setup for Cu NPs synthesis.

2.3.8 Electrode Fabrication Process

Gas diffusion electrode (GDE) was used as substrate. For catalysts layer, 3.8 mL iso-propanol was mixed with 50 mg catalyst and 200 μL Sustanion XC-1 solution (5% in ethanol) was added to the mixture. 25 mg graphite and 25 mg Vulcan carbon were both added into 3.8 ml iso-propanol and 200 μL Sustanion XC-1 solution to prepare the carbon layer ink. Each ink was under probe sonication for at least 15 minutes depends on the dispersion. The catalyst layer was first sprayed onto 4×6 cm^2 GDE (Freudenberg H14C10) via air-spray gun, followed by the spray of carbon layer. The GDE was then cut into 2×2 cm^2 pieces for performance tests.

2.3.9 Electrochemical Measurements

Electrochemical tests were performed using an electrochemical workstation (Autolab PGSTAT302N) in a home-designed flow cell. The mass flow controller (MFC, Bronkhorst) was used to control the CO_2 flow rate at 30 mL/min under ambient pressure (equals to sccm, standard cubic centimeter per minute). The flow rate of the cathode and

anode electrolyte streams were 10 mL/min controlled by two peristaltic pumps. The area of the cathode in flow cell and MEA was 1×1 cm^2. All ECR measurements were carried out at room temperature and ambient pressure. The concentration of gas phase products was quantified on a Shimadzu Nexis GC-2030 system with a flame ionization detector (FID), a thermal conductivity detector (TCD) and a dielectric-barrier discharge ionization detector (BID). For all flow cell measurements, a leak-free Ag/AgCl reference electrode was inserted in catholyte chamber close to cathode surface and all cathode potentials were converted to RHE scale *via* the following equation:

$$E_{(RHE)} = E_{(Ag/AgCl)} + 0.205 + 0.059 \times pH + iR \quad \textbf{(Equation 2.14)}$$

where R is the resistance between the cathode and reference electrodes which was measured by electrochemical impedance spectroscopy (EIS) with a frequency range from 1×10^5 Hz to 0.5 Hz at open circuit potential (OCP). 70% of the electrolyte resistance was later compensated for all chronoamperometry experiments to correct the potential (**Eq. 2.14**). All potential reported in the following chapters are in RHE scale unless otherwise specified.

2.3.10 EIS Measurements

EIS scans at different potentials were measured in the same flow cell under CO_2 flow. The applied potentials were from -0.6 V to -1.6 V with a step of 0.2 V (versus Ag/AgCl reference electrode). The frequency range was from 2×10^5 Hz to 0.5 Hz. The flow rate of electrolyte in each chamber was 3.3 mL/min, a third of the performance measurement conditions, to reduce fluctuations and the gas flow rate was 30 mL/min. The applied potential range was set according to the current density from 0 to about 30 $mA\cdot cm^{-2}$. The scan was measured after performance test in the same cell with the same electrode. The EIS were presented in Nyquist and Bode plot. Calculations of Faradaic Efficiency

Faradaic efficiency (FE) was calculated using the following equations:

$$Q_i = n_i \times N_A \times N_e = \frac{P_0 V_i}{RT} \times N_A \times N_e \qquad \textbf{(Equation 2.15)}$$

$$Q_{Total} = \frac{I_{Total} \times t}{e} \qquad \textbf{(Equation 2.16)}$$

$$FE\,\% = \frac{Q_i}{Q_{Total}} = \frac{e N_A \times P_0}{RT} \times \frac{V_i \times N_e}{I_{Total} \times t} = \frac{F \times P_0}{RT} \times \frac{c_i \times vt \times N_e}{I_{Total} \times t} = \frac{N_e F \times P_0}{RT} \times \frac{c_i v}{I_{Total}}$$

(Equation 2.17)

where Q_i represents the amount of charge transferred to produce the product i, Q_{Total} represents the total charge transferred during the reaction, n_i is for the mole of product i and the gas products are treated as ideal gas, N_A is Avogadro constant, N_e is the number of electrons transferred to form one molecule (i.e., N_e=2 for CO, N_e=8 for CH_4, N_e=12 for C_2H_4), I_{Total} is the total current on the working electrode, e is the charge of one electron; F is faradaic constant ($F = eN_A$ = 96485 C/mol), c_i is the concentration of product of interest measured from GC, v is the total flow rate from the outlet of the cell. Other constants: P_0 = 101325 Pa, T = 298 K and R = 8.314 J/(mol·K).

2.3.11 XRD Measurements

XRD patterns were collected on a Bruker D8 Advance diffractometer with a LynxEye detector and Cu Kα1 radiation (λ= 1.5406 A) operating at 40 kV and 25 mA (step size at 0.019º, time per step at 0.10 s and total number of steps at 4368). Samples in powder form were pressed onto a glass preparative slide which was then attached to a sample holder. Sample dissolved in solvent were first drop cast onto the slide to evaporate the solvent before attached to the holder. All measurements were scanned at 2θ of 5-90º.

2.3.12 SEM Measurements

SEM images were taken on a Zeiss NVision 40. GDE samples were stick to specimen stubs with Agar Conductive carbon adhesive tapes. Prof. Alex Robertson and Ms. Yi Yuan from Department of Materials took the SEM images for this thesis.

2.3.13 TEM Measurements

High-resolution TEM (HRTEM) images in this thesis were acquired using a JEOL JEM-2100 and JEOL 3000F microscope. Sample was first dispersed in ethanol then loaded dropwise onto lacey carbon-coated copper mesh (400 meshes) or molybdenum mesh grids when carrying out EDX measurements to avoid Cu interference. TEM images in this thesis were taken in collaboration with Ms. Yi Yuan and Dr. Tianyi Chen in the Department of Materials, University of Oxford.

2.3.14 XPS measurements

XPS was applied for investigation of chemical composition and corresponding chemical states of copper-based materials. A PHI Quantum-2000 photoelectron spectrometer (Al Kα: 1486.7 eV, with operation parameters of 15 kV, 35W and 200 μm spot size) with an Omicron Sphera II hemispherical electron energy analyser on the Thermo Scientific model Nexsa was used for XPS measurements. The voltage of aluminium anode tube for x-ray emission was kept at 12 kV. For survey scans, the pass energy was set to 200 eV with 1 eV/step and the scan was repeated for 5 times. As for high-resolution XPS spectra, 10 scans were measured at 0.1 eV/step and 50 eV pass energy. All the XPS spectra were calibrated according to the characteristic C 1s peak at ca. 284.8 eV (C-C) to eliminate potential charging of the samples during measurements. The XPS was measured at Harwell XPS by Dr. Shaoliang Guan.

2.3.15 *In-situ* Raman Measurements

In-situ Raman spectra were recorded with a Horiba Xplora Plus Confocal Raman Microscope using a 532 nm excitation laser and 1800 grating with a 50x long working distance lens. The *in-situ* Raman cell was a designed one-chamber cell with three electrodes and a quartz window at the top. The working electrode is GDE with exposed catalyst layer (about 0.5 $mg \cdot cm^{-2}$) fixed by a clip electrode. Pt wire and Hg/HgO (1M KOH) were used as counter electrode and reference electrode, respectively. Electrolyte was 1M KOH with CO_2 flow before the measurement. The potential of working electrode was controlled by GAMRY (Gamma 1000) in potentiostatic mode without iR compensation. The Raman measurements were performed in Advanced Technology Institute, University of Surrey with the assistance of Xuelei Pan, Dr. Manman Wang and Prof. Yunlong Zhao.

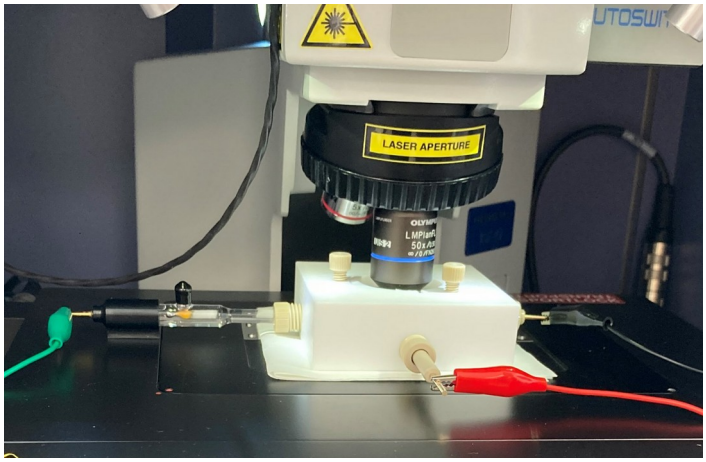


Figure 2.9 Photo of the setup for *in-situ* Raman measurements.

2.3.16 XAS Measurements

The *ex-situ* hard X-ray absorption spectroscopy measurements were conducted at beamline BL01C of the Synchrotron Radiation Research Centre (SRRC) in Taiwan with catalysts spray coated on GDE. The *in-situ* XAS measurements were conducted at beamline BL05U of Shanghai Synchrotron Radiation Facility (SSRF) in Shanghai. Fluorescence mode was used to collect the data. The *in-situ* cell was a homemade one

compartment cell with three electrodes. CO_2 was bubbled to electrolyte before each measurement and stopped bubbling during the measurement to reduce background noise.

2.3.17 Operando PTR-TOF-MS Measurements

This characterisation follows a similar procedure reported by H. Ren *et al*[41]. Mass spectra were collected using a PTR–TOF–MS 8000 (IONICON) with H_3O^+ as the primary ion and a resolution of 5,000–8,000(m/Δm based on the definition from IUPAC). Mass spectra were recorded once per second. The instrument was connected to the centre of the working electrode from the gas chamber via a 1/16-inch capillary and the dilution rate of the sample gas was maintained same for all samples. The gas path was SilcoNert-coated steel tubing covered with heating tapes at 80 °C to minimize adsorption of organic species on the capillary walls (i.e., memory effect). The operando system was initially operated for 100 s without any external current to collect background mass spectra after the background signal became stable. Then, a scan at 0.15 $mA \cdot s^{-1}$ was applied to the GDE from 0 mA to -100 mA (~660 s), followed by an additional 200 s without any external voltage. The flow rate in the probe near GDE was about 1.5 sccm and total flow rate to the PTR–TOF–MS was 100 sccm.

2.4 Reference

1. H. Topsøe, Developments in operando studies and in situ characterization of heterogeneous catalysts, *J. Catal.*, 2003, **216**, 155-164.
2. W. J. Rohrbaugh and E. L. Wu, American Chemical Society, 1989, 411, 279-302.
3. R. E. Dinnebier and S. J. L. Billinge, *Powder Diffraction Theory and Practice*, Royal Society of Chemistry, 2008.
4. W. H. Bragg and W. L. Bragg, The reflection of X-rays by crystals, *Proceedings of the Royal Society of London.*, 1997, **88**, 428-438.

5. C. F. Holder and R. E. Schaak, Tutorial on Powder X-ray Diffraction for Characterizing Nanoscale Materials, *ACS Nano*, 2019, **13**, 7359-7365.
6. A. L. Patterson, The Scherrer Formula for X-Ray Particle Size Determination, *Phys. Rev,*, 1939, **56**, 978-978.
7. P. Scherrer, Bestimmung der Größe und der inneren Struktur von Kolloidteilchen mittels Röntgenstrahlen, *Nachrichten von der Gesellschaft der Wissenschaften zu Göttingen, Mathematisch-Physikalische Klasse*, 1918, **1918**, 98-100.
8. B. J. Inkson, Woodhead Publishing, 2016, DOI: 10.1016/B978-0-08-100040-3.00002-X, 17-43.
9. E. Abbe, Beiträge zur Theorie des Mikroskops und der mikroskopischen Wahrnehmung: I. Die Construction von Mikroskopen auf Grund der Theorie, *Archiv für mikroskopische Anatomie*, 1873, **9**, 413-418.
10. Transmission Electron Microscope (TEM) with EDX detector, https://www.mpi-bremen.de/en/Transmission-Electron-Microscope-TEM-with-EDX-detector.html#section19163.
11. Transmission Electron Microscopy - Nanoscience Instruments, https://www.nanoscience.com/techniques/transmission-electron-microscopy/.
12. R. Rana, F. D. Vila, A. R. Kulkarni and S. R. Bare, Bridging the Gap between the X-ray Absorption Spectroscopy and the Computational Catalysis Communities in Heterogeneous Catalysis: A Perspective on the Current and Future Research Directions, *ACS Catal.*, 2022, **12**, 13813-13830.
13. A. S. Hoffman, L. M. Debefve, A. Bendjeriou-Sedjerari, S. Ouldchikh, S. R. Bare, J. M. Basset and B. C. Gates, Transmission and fluorescence X-ray absorption spectroscopy cell/flow reactor for powder samples under vacuum or in reactive atmospheres, *Rev. Sci. Instrum.*, 2016, **87**.
14. J. Timoshenko and B. Roldan Cuenya, In Situ/ Operando Electrocatalyst Characterization by X-ray Absorption Spectroscopy, *Chem. Rev.*, 2021, **121**, 882-961.
15. J. L. DuBois, P. Mukherjee, T. D. P. Stack, B. Hedman, E. I. Solomon and K. O. Hodgson, A systematic K-edge X-ray absorption spectroscopic study of Cu(III) sites, *J. Am. Chem. Soc.*, 2000, **122**, 5775-5787.
16. G. Martens, P. Rabe, N. Schwentner and A. Werner, Improved extended-x-ray-absorption fine-structure (EXAFS) studies applied to the investigation of Cu-O, Cu-N, and Cu-Br bond lengths, *Phys. Rev. B*, 1978, **17**, 1481-1481.

17. About XAS - Diamond Light Source, https://www.diamond.ac.uk/industry/Techniques-Available/Spectroscopy/X-ray-spectroscopy-XAS/About-XAS.html.
18. I. V. Chernyshova, P. Somasundaran and S. Ponnurangam, On the origin of the elusive first intermediate of CO_2 electroreduction, *Proc. Natl. Acad. Sci. U. S. A.*, 2018, **115**, E9261-E9270.
19. S. Mosca, C. Conti, N. Stone and P. Matousek, Spatially offset Raman spectroscopy, *Nat. Rev. Methods Primers*, 2021, **1**. 21.
20. N. Elgrishi, K. J. Rountree, B. D. McCarthy, E. S. Rountree, T. T. Eisenhart and J. L. Dempsey, A Practical Beginner's Guide to Cyclic Voltammetry, *J. Chem. Educ.*, 2018, **95**, 197-206.
21. A. J. Bard and L. R. Faulkner, *Electrochemical Methods: Fundamentals and Applications*, Wiley, 2000.
22. J. G. Osteryoung and R. A. Osteryoung, Square wave voltammetry, *Anal. Chem.*, 1985, **57**, 101-110.
23. S. Wang, J. Zhang, O. Gharbi, V. Vivier, M. Gao and M. E. Orazem, Electrochemical impedance spectroscopy, *Nat. Rev. Methods Primers*, 2021, **1**, 1-21.
24. L. A. Middlemiss, A. J. R. Rennie, R. Sayers and A. R. West, Characterisation of batteries by electrochemical impedance spectroscopy, *Energy Reports*, 2020, **6**, 232-241.
25. K. Jüttner, Electrochemical impedance spectroscopy (EIS) of corrosion processes on inhomogeneous surfaces, *Electrochim. Acta*, 1990, **35**, 1501-1508.
26. E. P. Randviir and C. E. Banks, A review of electrochemical impedance spectroscopy for bioanalytical sensors, *Anal. Methods*, 2022, **14**, 4602-4624.
27. V. M.-W. Huang, V. Vivier, M. E. Orazem, N. Pébère and B. Tribollet, The Apparent Constant-Phase-Element Behavior of an Ideally Polarized Blocking Electrode: A Global and Local Impedance Analysis, *J. Electrochem. Soc.*, 2006, **154**, C81-C81.
28. A. R. C. Bredar, A. L. Chown, A. R. Burton and B. H. Farnum, Electrochemical Impedance Spectroscopy of Metal Oxide Electrodes for Energy Applications, *ACS Appl. Energy Mater.*, 2020, **3**, 66-98.
29. B.-Y. Chang, The Effective Capacitance of a Constant Phase Element with Resistors in Series, *J. Electrochem. Sci. Technol*, 2022, **13**, 479-485.

30. A. F. Lopes, T. S. M. Fernandes and R. F. do Nascimento, Barrier Discharge Ionization Detector in Gas Chromatography: A Review on Applications, *Crit. Rev. Anal. Chem.*, 2021, **53**, 614-633.
31. C. J. Bondue and M. T. M. Koper, A DEMS approach for the direct detection of CO formed during electrochemical CO_2 reduction, *J. Electroanal. Chem.*, 2020, **875**, 113842-113842.
32. G. Greczynski and L. Hultman, A step-by-step guide to perform x-ray photoelectron spectroscopy, *J. Appl. Phys.*, 2022, **132**, 11101-11101.
33. H. Ren, M. Kovalev, Z. Weng, M. Z. Muhamad, H. Ma, Y. Sheng, L. Sun, J. Wang, S. Rihm, W. Yang, A. A. Lapkin and J. W. Ager, Operando proton-transfer-reaction time-of-flight mass spectrometry of carbon dioxide reduction electrocatalysis, *Nat. Catal.*, 2022, **5**, 1169-1179.

Chapter 3 Cu on Proton-conductive Supports for Methane Production

3.1 Introduction

Converting CO_2 into value-added products is a potential solution of decreasing carbon emission. Among all the products from electrochemical CO_2 reduction (ECR), methane is the one that requires the most electrons transferred up to 8 per carbon atom, which makes it one of the most challenging reactions to achieve with high selectivity. The steps to reduce CO_2 to methane consist of the adsorption of CO_2 molecules and protonation of intermediates[1-3]. It is essential to find a rate-matching point between adsorption and protonation steps to avoid the unwanted CO production or the C-C coupling to form multi-carbon molecules[4].

Being under the spotlight ever since ECR research emerged, copper-based catalysts have always been studied to achieve higher selectivity to hydrocarbons as introduced in Chapter 1. It is, therefore, unneglectable that copper itself could facilitate C-C coupling during the reduction of CO_2 while balancing the rate with protonation steps generating hydrocarbon products with decent selectivity[5-7]. Apart from the studies chasing high selectivity of ethylene and other multi-carbon products from Cu, there are scientists focusing on the methane production with copper[8, 9]. One of the most popular strategies to tune the reactions on catalysts surface is to establish an interface that forms between two components with different preference[10-12]. Metal alloy and supported catalysts have shown such effects in ECR[13], for instance, the CuAu alloy with controlled ratio of syngas CO/H_2 production[14], CuFe alloy for production of methane[15] and the CeO_2-supported Au for nearly 100% selectivity to CO[16]. Selecting an appropriate support or exotic component is the key to boost the reactivity. Transition metal oxides/sulphides are the usual choice of metal supports because of the various valence states of metal giving rise to vacancies[17]

that could act as the redox media[18]. MoS_2, for example, has shown high HER reactivity benefit from the 2D-layered structure and rich-edge active sites[19, 20], which makes it a good proton activation support. However, the rate-limiting step of ECR is unlikely to be the protonation step when the surface coverage of proton is high enough (*i.e.*, in neutral or acidic electrolyte) but instead the process related to carbon species on the catalysts surface. And the choice of MoS_2 leads to HER dominated performance according to our observations. Therefore, a support that could attract as much as CO_2 species was proved to be a more appropriate choice for catalysts designing.

The alkaline-earth metal oxides have been used as carbon capture materials[21-23]. When exposed to water, MgO will undergo hydroxylation on the surface oxygen atoms and forming the corresponding hydroxides layer[24]. Our group's previous studies have unveiled the proton-hopping ability of MgO(111) surface under elevated temperatures[25, 26], which raises our interests to investigate the possibility of using MgO as a metal support in aqueous environment. Theoretical calculations have shown improved reactivity on few-layer MgO/metal heterojunctions for reduction of CO_2 molecules[27, 28]. Such results support our hypothesis that hydrated MgO could create an -OH layer on the surface and capture the CO_2 molecules from the electrolyte via carbonation.

In this chapter, both MoS_2 and MgO/$Mg(OH)_2$ were selected as the support to verify their proton mobility under electric field. MoS_2 exhibited unexpected high HER reactivity under both neutral and alkaline conditions and is believed to be inappropriate as a substrate for ECR. In comparison, the hydrated MgO support was found to assist the methane up to 45% with a current density as high as 400 $mA \cdot cm^{-2}$. The high ratio of C_1/C_2 was due to the increased rate of protonation on the surface, possibly resulted from the OH surface layer keeping the surface pH value at a stable level. And the capturing of CO_2 by the MgO/$Mg(OH)_2$ surface was proved by *in-situ* Raman spectra indicating the

carbonation steps taking place on the oxide/hydroxide surface. The Cu species were monitored by *in-situ* XAS, in which they exhibited high endurance to reduction potentials and maintained a positive valence state at -1 V owing to the strong interactions with MgO support.

3.2 Results and Discussion

Synthesis methods and notations of the materials involved in this chapter can be found in previous sections 2.3.2-2.3.4. Characterisation methods were described in sections 2.3.12-2.3.14.

3.2.1 Cu on supports in PEM Electrolyser

3.2.1.1 Cu on few-layer MoS_2

The support tested first was MoS_2 which has shown exceptional high activity on proton activation during HER[29]. It is believed that exfoliation of MoS_2 allows the exposure of adequate active sites on the surface and edges that could boost the reactivity. By promoting the rate of the proton activation step, we anticipated that the supported Cu would allow a rapid protonation to carbon-related intermediates. In this study, the MoS_2 played a role as the support of Cu aiming to provide a proton supply for ECR. It turned out, however, that HER dominated the whole electrochemical reactions and trace of CO_2 reduction products were detected.

The XRD patterns of Li-MoS_2 and Cu-MoS_2 are shown in **Fig. 3.1a**. The sharp peak of Li-MoS_2 (black line) at 14.3⁰ is designated to the (002) plane of MoS_2 indicating that the Li-MoS_2 remains bulky. The peaks at 32.6⁰ and 39.5⁰ also imply that the Li-MoS_2 has good crystallinity. The TEM image of Li-MoS_2 (**Fig. 3.1b**) agrees with the XRD results. In contrast, the Cu-MoS_2 sample (red line) does not show any characteristic peak of MoS_2

due to the exfoliation that break the long-range order of the bulk MoS_2. The peak at around 22⁰ (red diamond) could be designated to copper molybdenum oxide ($Cu_xMo_yO_z$), yet the composition needs to be clarified. No copper oxide or hydroxide peaks are shown in the XRD pattern, which could be explained by the amorphous morphology of Cu species shown in TEM images (**Fig. 3.1c**).

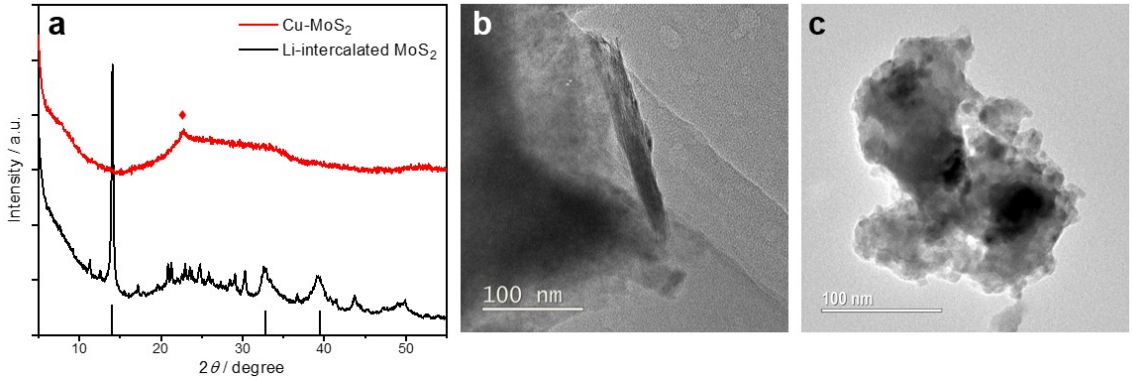


Figure 3.1 (a) XRD patterns of Li-intercalated MoS_2 and Cu-exchanged MoS_2. TEM images of **(b)** Li-MoS_2 and **(c)** Cu-MoS_2.

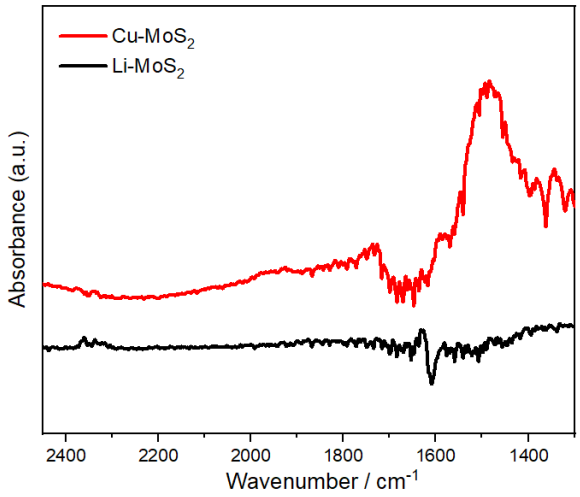


Figure 3.2 Infrared spectra of Li-MoS_2 (black curve) and Cu-MoS_2 (red curve).

Different IR spectra were observed on the samples before and after copper loading in diffuse reflectance infrared Fourier transform spectroscopy (DRIFTS). Humidified CO_2 was first supplied in the sample holder and maintained for 5 min at room temperature. Then dry N_2 was purged into the sample chamber to remove the excessive CO_2 and H_2O.

The spectra were collected right after the purging begins. The extent of purging is reflected from the intensity of the CO_2 stretching peak (2300-2400 cm^{-1}) and the selected spectra were collected when the peak at 2300-2400 almost disappeared. The broad peak between 1400 cm^{-1} and 1500 cm^{-1} of the red line is designated to HCO_3^- species on the Cu-MoS_2 after purging, whose broadening is likely due to the O-H bending from the moisture residual in the chamber. The peak located at around 1700 cm^{-1} could be assigned to the cluster of bicarbonate ion and water molecules[30] (**Fig. 3.2**, red curve). Comparing with the Li-MoS_2 (**Fig. 3.2**, black curve), this difference could be resulted from the carbon species uniquely adsorbed on copper surface.

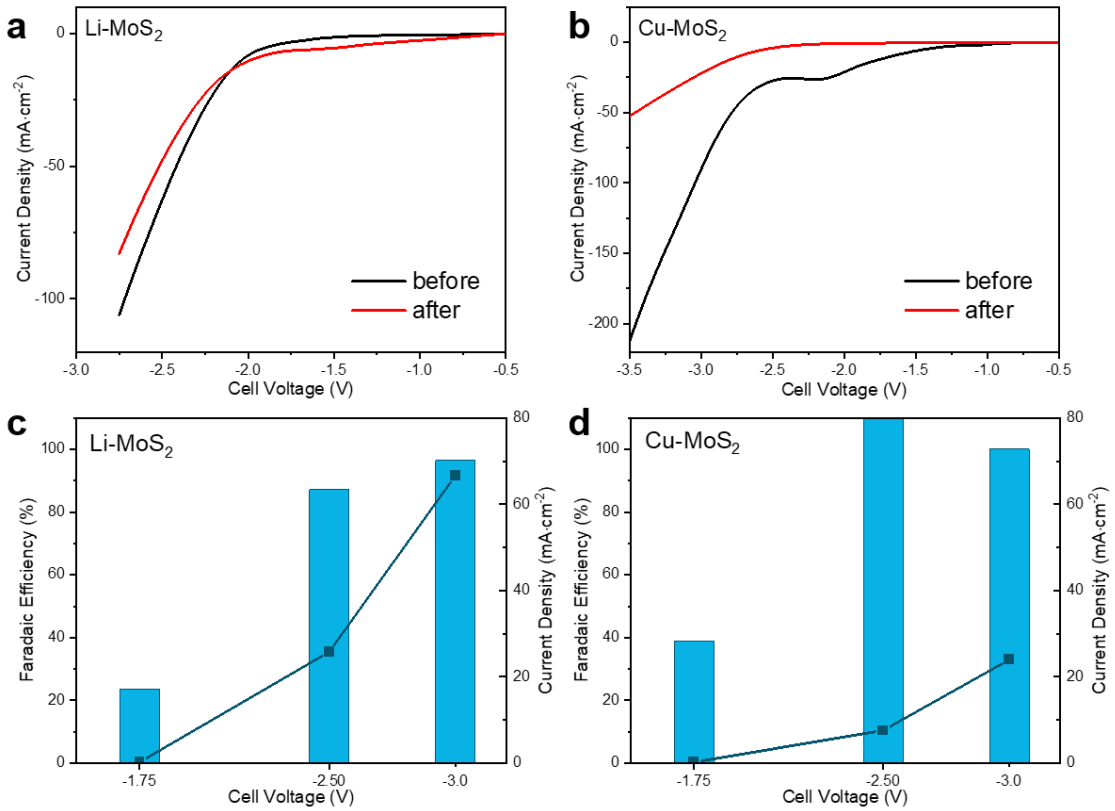


Figure 3.3 LSV curves of **(a)** Li-MoS_2 and **(b)** Cu-MoS_2 before (black) and after (red) the tests. **(c)** and **(d)**: Faradaic efficiency of H_2 (left y-axis, dark blue) and current density (right y-axis, light blue) at different operating potentials in PEM-MEA cell.

Li-MoS_2 and Cu-MoS_2 samples were tested on CO_2 reduction in the PEM-MEA cell. The catalysts loading was around 1 mg/cm^2 on a 2.25 cm^2 GDL. The linear sweep

voltammetry (LSV) curve (**Fig. 3.3a** and **3.3b**) shows changes of the current density and the onset potential of catalysts before and after the chronoamperometry test at different potentials between working electrode and counter electrode. The deactivation of Li-MoS_2 sample is less than the Cu-MoS_2. For the current density, a large proportion of Cu-MoS_2 is contributed to the reduction of Cu(II) to Cu(0) and Cu(I), which could explain the lower current after the test. Comparing the onset potential (potential at 10 mA/cm^2), the Li-MoS_2 is dominated by the MoS_2 that facilitates the HER, and thus has a smaller overpotential compared to the Cu loaded MoS_2 sample. Hydrogen is the only products detected by GC for both catalysts at all potentials. The current density shown at each potential (**Fig. 3.3c** and **3.3d**, right axis) is the average current density corresponding to the potential applied. Only trace amount of CO is detected by the GC. Since the faradaic efficiency of hydrogen is over 90% after the start of the HER and no other carbon products can be confirmed, quantification liquid products were not carried out. Overall, the MoS_2 support showed much higher selectivity towards HER than ECR.

3.2.1.2 Cu on $Mg(OH)_2$ support

The XRD patterns of the synthesized 2, 5 and 10 wt.% Cu-$Mg(OH)_2$ samples are shown in **Fig. 3.4a**. The peaks marked by the solid black line in the bottom belong to $Mg(OH)_2$ support. Small peaks appearing at around 15.9⁰, 31.5⁰ and 39.5⁰ are identified as copper chloride hydroxide, which indicates that a composite formed because of the residual Cl^- ions on the surface. The intensity of these peaks also increases as the percentage of copper loading rises. Further studies are required to clarify what effects this compound could bring to the ECR performance. The XRD pattern after the ECR test should also be taken to identify any change of composition. Considering the negative potentials applied to the electrode, it is likely that the Cu(OH)Cl compound will finally disappear as the Cu(II) tends to be reduced to Cu(I) and Cu(0) during the reduction of CO_2.

TEM images of three samples are displayed in **Fig. 3.4b**, **3.4c** and **3.4d**. The 2% sample has no nanoparticles visible in the image. The dispersion of the copper nanoparticles on the surface is better in the 5% sample than the 10% one. And the size of particles is also smaller and more uniform in the 5% sample. The amorphous structure in the bulk is likely to be $Mg(OH)_2$ support which preserves its intrinsic layered morphology but tend to stack with metal loaded. The thickness of the $Mg(OH)_2$ support calculated from EELS (**Fig. A1**) by mean-free-path was around 98 nm, in consistence with AFM results at 105.92 nm.

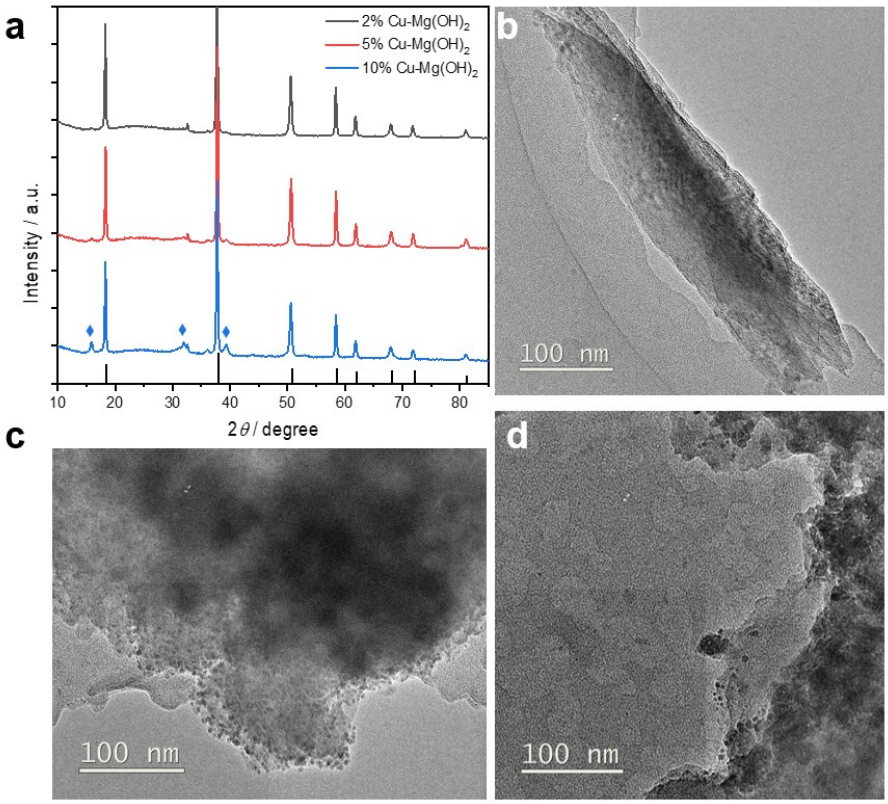


Figure 3.4 (a) XRD pattern of Cu-$Mg(OH)_2$ with different copper loading. Black vertically line in the bottom mark the peaks belonging to $Mg(OH)_2$. TEM images of **(b)** 2% Cu-$Mg(OH)_2$, **(c)** 5% Cu-$Mg(OH)_2$ and **(d)**10% Cu-$Mg(OH)_2$.

The selectivity of CO_2 reduction with PEM-MEA on Cu-$Mg(OH)_2$ was relatively low due to the poor conductivity of support and the high HER rate. Mass spectroscopy (MS) was used to detect the products and no signal of carbon species was found. Despite of this, the experiment was continued to achieve the real-time detection taking the advantage of MS.

LSV curve (**Fig. 3.5a**, left axis, dark blue curve) was measured at a scan rate of 2mV/s from –2.5V to –3V, while the signal of m/z=2 (hydrogen) was being monitored (**Fig. 3.5a**, right axis, light blue curve). As the applied potential becomes more negative, the current density and the intensity of the signal increase almost simultaneously. There is a time lag of around 6 seconds between the electrochemical workstation and the MS due to the length of the gas line as well as the dwell as settling time of the MS. Chronoamperometry results are shown in **Fig. 3.5b** at three different cell voltages. The trend of current density agrees with the intensity of hydrogen ions signal since both are increasing as the operation potential becomes more negative.

The aim of using MS measurement on ECR is to instantly detect the products under a varying potential. Most ECR products are detectable by MS except CO which has the same fragment (m/z=28) as CO_2[31]. This method is more powerful when there are multiple products[32]. It is promising that MS could provide a full products distribution in a short time scale and even more details of CO_2 reduction reactions occurring on the surface. But the current quadrupole MS in our lab cannot match the concentration of carbon species in the DEMS cell, due to the interfering of excessive CO_2 fragments. MS measurements were further updated with a PTR-TOF-MS which will be applied in chapter 6.

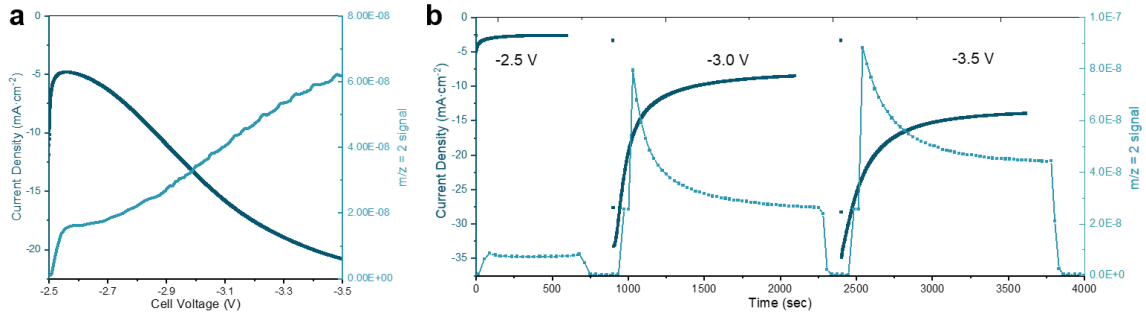


Figure 3.5 (a) LSV (left axis, dark blue) and the corresponding H_2 signal (right axis, light blue) of 10% Cu-$Mg(OH)_2$ sample. **(b)** Chronoamperometry at different full cell potentials and the corresponding H_2 signal of 10% Cu-$Mg(OH)_2$.

In summary, copper particles loaded on $Mg(OH)_2$ support did not exhibit high ECR performance in the PEM cell. The dominant product from cathode was hydrogen gas generated from water splitting. The main reason was that PEM allowed transportation of protons towards the cathode, leading to its accumulation on the local surface of the cathode. The $Mg(OH)_2$ support might not favour the hopping of protons to reach copper surface. This increased the possibility of proton activation and hydrogen formation. Changing the membrane and electrolyte that enables a high pH environment would be one of the solutions to overcome this issue.

3.2.2 Cu on $Mg(OH)_2$ support in AEM-MEA Electrolyser

Further to the PEM testing, AEM became our first choice of membrane for ECR testing. Modifications to $Mg(OH)_2$ support were also tried aiming to increase the selectivity on the catalyst side. Taking the advantage of the layered structure, $Mg(OH)_2$ is believed to provide higher interface area by intercalating with molecules such as acetone. During intercalation, Van der Waals force between the layers are interrupted and the number of layers decreased which creates plenty of metal-support interface when loading Cu. From the XRD patterns, the $Mg(OH)_2$ (101) facet (2θ = 37.9º) dominates the material both before and after the loading of Cu. Cu precursor residual, $CuCl_2{\cdot}Cu(OH)_2$, appears in both commercial $Mg(OH)_2$ support and acetone-treated $Mg(OH)_2$ ($AMg(OH)_2$) (**Fig. 3.6** blue diamond). These residuals are unlikely to affect the further performance test, as most of them will be reduced to Cu in the LSV pre-treatment. For $BMg(OH)_2$, the Cu species peaks are invisible, indicating a well-dispersed Cu loading.

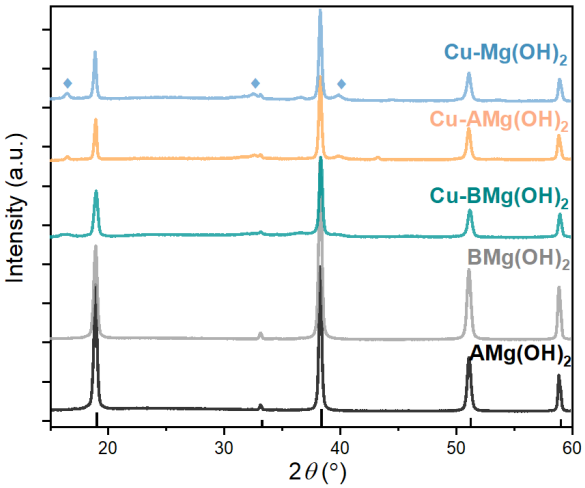


Figure 3.6 XRD patterns of different $Mg(OH)_2$ supports and Cu-loaded $Mg(OH)_2$.

The ECR performance tests were carried out in an AEM-MEA setup. With the assistance of AEM, the selectivity of C_1 products was significantly higher than that with PEM. Though hydrogen still takes up more than 50% of the total products, it becomes possible to calculate the ratio of C_1/C_2, where C_1 and C_2 are the majority of the carbon-related gas products. Comparing three types of $Mg(OH)_2$ supports with same copper loading level, it is found that the commercialized support does not outperform the others (**Fig. 3.7a**). Both acetone-treated and bottom-up $Mg(OH)_2$ supports show up to ten-fold higher C_1/C_2 ratio than bare CuO and $Cu(OH)_2$ (**Fig. 3.7b-d**). From the perspective of current, the controlled CuO catalysts has the highest current density at 3.5V cell voltage. The production of methane is, on the contrary, the lowest compared to all three Cu-supported catalysts. Thus, the selectivity of methane in ECR is improved by using $Mg(OH)_2$ as a support. The higher current density does not guarantee the higher selectivity, as the co-existence of HER from water splitting always takes place simultaneously. In summary, the $Mg(OH)_2$ supports indeed favours the methane selectivity in ECR and suppresses the C_2 production. Yet the hydrogen production is high and there is still room to further increase the methane selectivity. A further optimization of both the electrochemical cell and the GC

for products quantifying were made, together with the development of Cu-loaded catalysts.

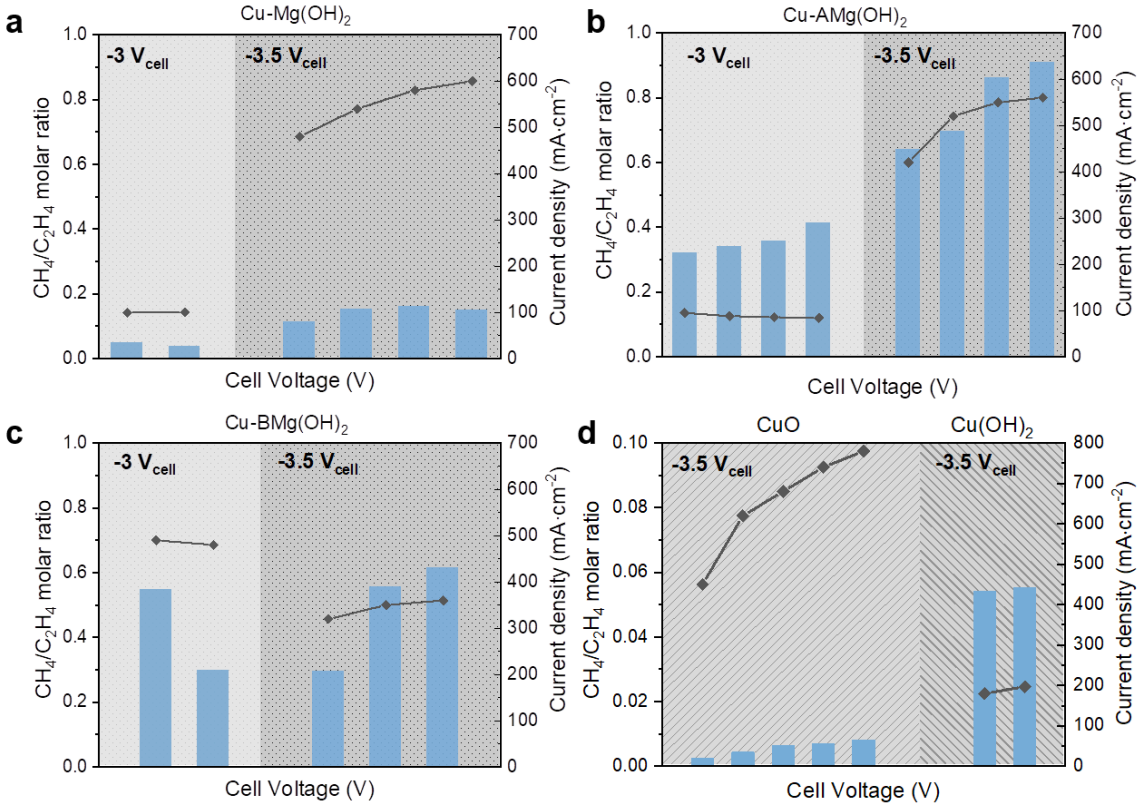


Figure 3.7 ECR performance of **(a)** Cu-$Mg(OH)_2$, **(b)** Cu-$AMg(OH)_2$ and **(c)** Cu-$BMg(OH)_2$ with the ratio of C_1/C_2 shown on the left y-axis and the total current density shown on the right y-axis. **(d)** CuO and $Cu(OH)_2$ performance at -3.5 V for comparison.

3.2.3 Cu on MgO support in AEM flow cell

With a primary understanding of the $Mg(OH)_2$ promotion to methane selectivity, a systematic study was completed on the MgO and $Mg(OH)_2$ supports. While MgO is widely known as an electrical insulator and good thermal conductor[33], the role of MgO as an electrocatalyst support is interesting to explore. It is generally known that surface Mg-O bond would be hydrolysed into $Mg(OH)_2$ in the presence of H_2O[34] and CO_2 molecules could also react with $MgO/Mg(OH)_2$. Our aim is to reveal if the phase transformation of supports exert any influence on the performance of electrochemical reactions.

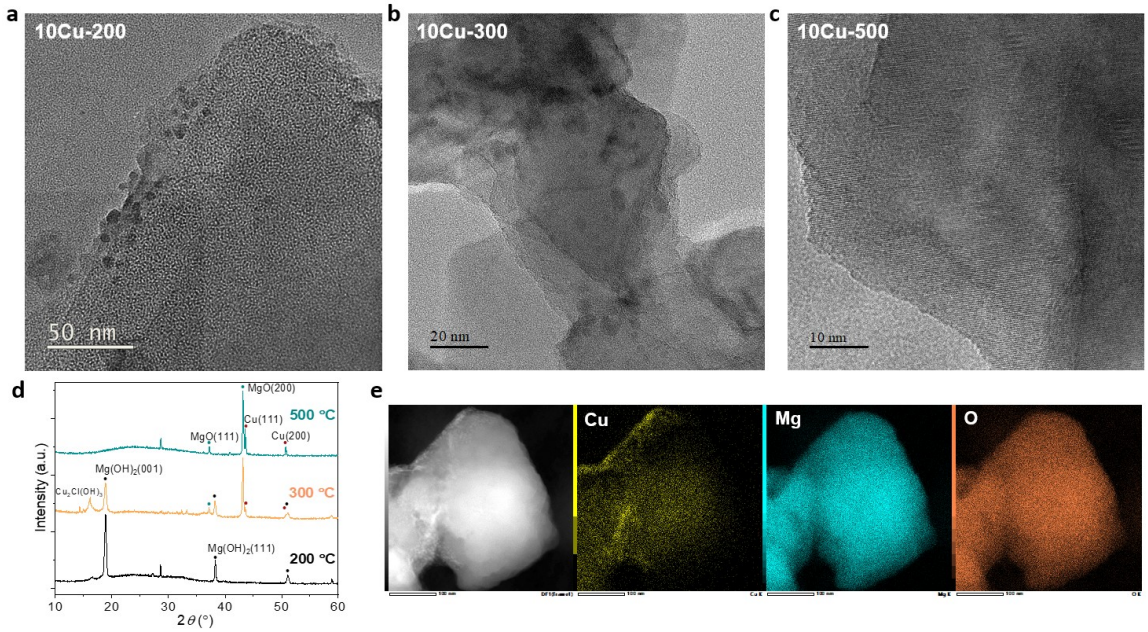


Figure 3.8 TEM images of **(a)** Cu-$Mg(OH)_2$ calcined at 200 ºC, **(b)** Cu-$Mg(OH)_2$ /MgO calcined at 300 ºC and **(d)** Cu-MgO calcined at 500 ºC. XRD patterns of Cu-loaded $Mg(OH)_2$ calcined at different temperatures. **(e)** EDX mapping of Cu (yellow), Mg (cyan) and O (orange) of 10Cu-500 sample.

The composition of supports was controlled by the calcination temperature. A low calcination temperature kept the $Mg(OH)_2$ in its original form and only copper was reduced from $CuCl_2$ precursor. As the temperature increasing, the $Mg(OH)_2$ was gradually dehydrated and completely converted into MgO at 500 ºC simultaneous to the generation of Cu particles. TEM images were taken on samples calcined at 200, 300 and 500 ºC (**Fig. 3.8a-c**). All supports preserves the layered structure regardless of calcination temperatures and the amount of copper loading. There are Cu aggregation on both the surface of $Mg(OH)_2$ phase and the mixed phases, and the Cu(II) residual still exists in the form of chloride and hydroxide which matches with the previous studies. The 500 ºC calcination assists better crystallisation of MgO and no Cu particles are visible on the edges. The dark area in the bulk MgO is likely originated from the Cu. The XRD patterns shows that Cu(0) existed in all three samples, confirming the successful reduction of Cu without changing the morphology of the support. EDX mapping of 10Cu-500 were

captured to visualize the distribution of Cu which matched with the XRD results. The bright area in the dark field is where Cu crowded (**Fig. 3.8e**). The aggregation of Cu into particles was noticed right after the TEM images were taken on the 10Cu-500 sample. This indicated that the dispersed Cu on MgO was in a quasi-stable state and stimulation such as electron beam or electric field would accelerate the particle growth[35].

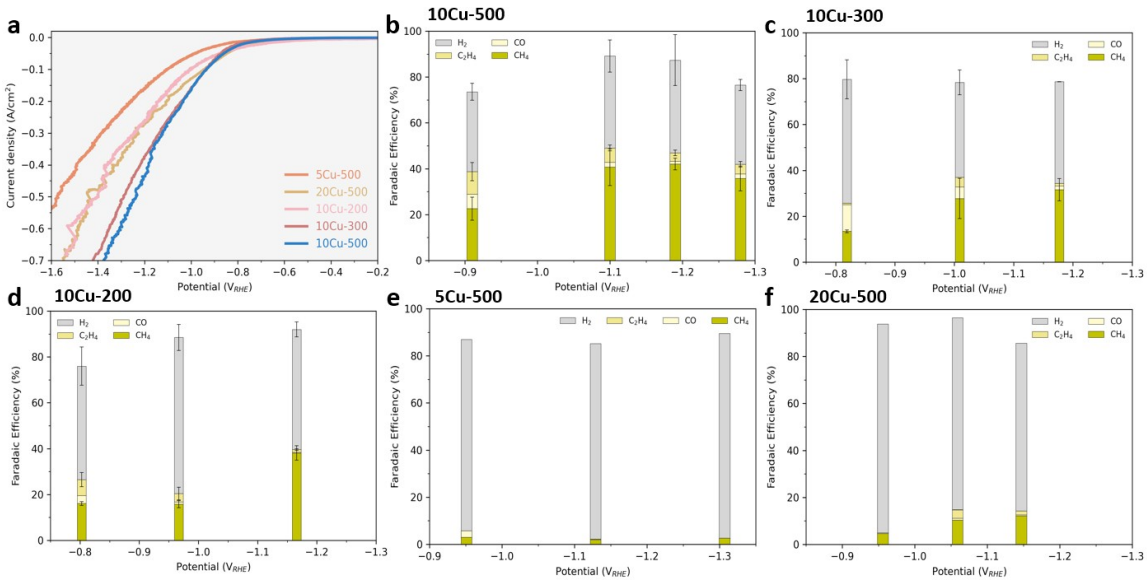


Figure 3.9 (a) LSV curves and gas-phase products FE measured in ECR of **(b)** 10Cu-200, **(c)** 10Cu-300, **(d)** 10Cu-500, **(e)** 5Cu-500, and **(f)** 20Cu-500**.**

ECR performance tests on these catalysts imply that copper loaded on MgO support could achieve methane selectivity up to 43% FE at -1.18 V (**Fig. 3.9b**) and has a higher methane selectivity than the other samples with different substrates (**Fig. 3.9c-d**). A further decrement or increment on the loading level of copper shows no sign of improving the ECR selectivity (**Fig. 3.9e-f**), which are due to the decreasing of Cu-MgO interface and the immoderate gathering of Cu particles, respectively. **Fig. 3.10** shows a detailed ECR performance of sample 10Cu-500. CO is the major ECR product at less negative potentials (< -0.1V_{RHE}) and methane efficiency increases as the potential deepening. The FE of methane reaches up to 53% and in a wide potential window of around 150mV from -1.1 to -1.25V_{RHE} the selectivity maintained above 43%. The partial

current density of CH_4, H_2 and CO is plotted in **Fig. 2c**, where the CH_4 current density peaks at -1.17V with a value of 220 $mA \cdot cm^{-2}$.

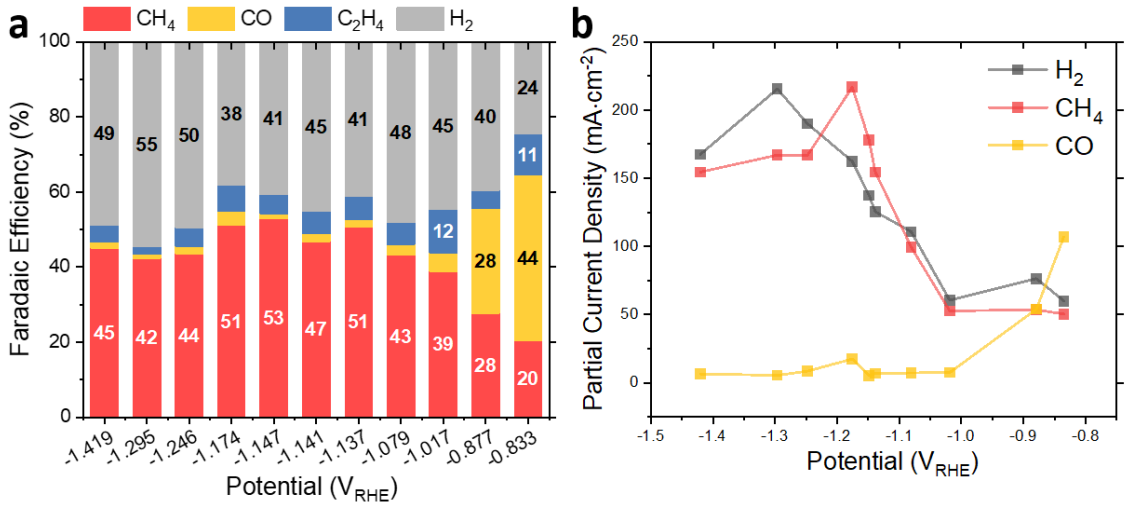


Figure 3.10 (a) Detailed ECR performance of 10Cu-500 with normalized FE of gas products plotted corresponding to potentials. **(b)** Particle current density of CH_4, CO and H_2 as a function of potential.

EIS studies were initially carried out before each performance test. During the testing, flooding of the GDE happened frequently and it was found that EIS could provide a faster method to identify the current state of the electrode before the actual electrolyte flooding occurred on the GDE. From **Fig. 3.11a**, the Bode plot of EIS could identify two separate charge transfer steps with different frequency on the interface, whereas under flooding conditions, only the low frequency step (around 4 Hz) is identified (**Fig. 3.11b**). When the electrode is in good condition, the 10Cu-500 catalyst has high selectivity to methane (**Fig. 3.10a**). The production of methane relies on the generation of key intermediates (*CO or *CHO) from CO_2 and the subsequent protonation steps. The blockage of gas pathways caused by flooding cuts the direct supply of CO_2 reactant to the catalysts; thus the generation of most carbon intermediates would become extremely slow or even stopped which is reflected on the disappearance of the high frequency process. Only

proton-related steps survived during the flooding of GDE leading to the unwanted hydrogen production from water splitting.

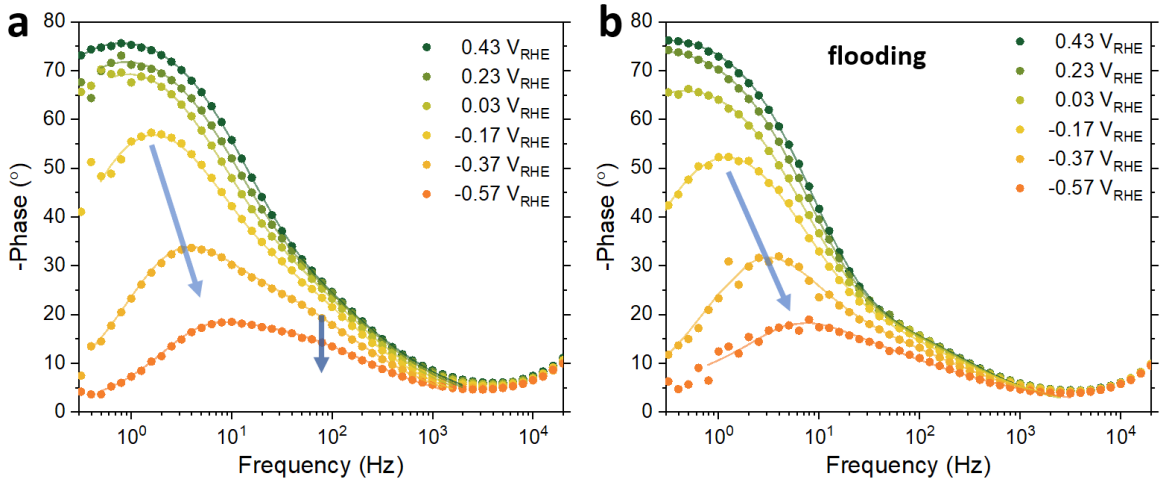


Figure 3.11 Bode plot in phase angle of **(a)** normally operating 10Cu-500 electrode and **(b)** after flooding. Light blue arrow indicates the low frequency process and dark blue arrow indicates the high frequency process. Bode plot in total impedance can be found in **Fig. A2**.

3.2.4 EPR of Copper on MgO Supports

To distinguish the promoting effects from MgO/$Mg(OH)_2$ supports, EPR was measured to monitor oxygen vacancies (V_O) that has been reported existing on MgO[36], as shown in **Fig. 3.10**. The signal at g = 2.003 is assigned to V_O on MgO, which exists in all samples except the $Mg(OH)_2$. Due to the sequence of preparing MgO before loading copper, the MgO sample was exposed to air for 24 hours before EPR was performed. This is believed to cause a slightly decreased oxygen vacancy signal intensity in MgO. The freshly prepared Cu-loaded MgO samples shows different signal intensity at g = 2.003. 10Cu-500 (**Fig. 3.12** red curve) exhibits the highest intensity implying a higher concentration than the other two samples. According to the properties of metal-oxide interface, it could be anticipated that Cu-MgO interface favours the accumulation of V_O[37]. A lower Cu loading has less interface area which explains the decreased signal response. Higher Cu

loading leads to severe aggregation of Cu as well as a phase separation in the catalysts, which impairs the formation of interface for V_O stabilization.

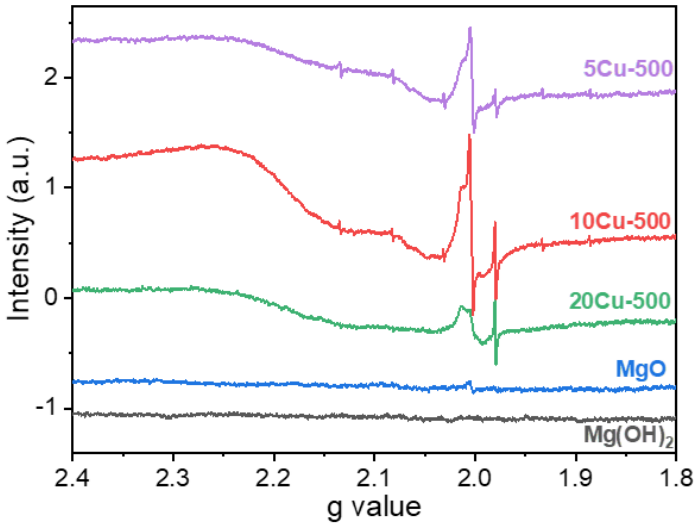


Figure 3.12 EPR patterns of MgO with different Cu loading.

EPR also provides signals for Cu(II), though it would be impossible to detect Cu(I) (d^{10} configuration) with no unpaired electrons. The small signals at g = 2.03 and g = 2.08 could be assigned to small CuO grains[38]. Further designation to the rest of Cu signals is unlikely to complete due to the complicated Cu(II) environment at the Cu-MgO interface. XAS would be a more appropriate tool to understand the local structure and the results will be covered in section 3.2.6.

3.2.5 *In-situ* Raman Spectroscopy

In-situ Raman was measured to understand surface adsorbates on Cu-$Mg(OH)_2$/MgO catalysts during the catalytic reactions. The Raman spectra (**Fig. 3.13a**) show a sharp peak at around 1035 cm^{-1} which could be assigned to the symmetric C-O stretching vibration of the adsorbed carbonate ($\nu_1CO_3^{2-}$)[39]. The dependence of $\nu_1CO_3^{2-}$ on potential illustrated in **Fig. 3.13b, c** is subject to the electrochemical stark effect[40]. In the cathodic region below -0.45V (**Fig. 3.13c**, blue area), the stark tuning rate is approximately 26 cm^{-}

^{1}/V implying that the carbonate species are affected by the interfacial electric field (applied negative potentials). This indicates that the $Mg(OH)_2$/MgO substrate was either capturing the carbonate ions in the electrolyte or the dissolved CO_2 molecules rapidly reacted with the surface hydroxyl group, resulting in the chemisorbed carbonate ions. The symmetric C-O stretching of CO_2^- ($\nu_s CO_2^-$) and CO_3^{2-} ($\nu_3 CO_3^{2-}$) are likely to overlap at around 1330 cm^{-1}, as seen from the broadened peak from -0.1V to -0.4V. The correlation between Raman shift and potentials is not strong (**Fig. 3.13a**, blue dashed line; **Fig. A3b**), while the intensity of the peak slightly increases as the potentials become more negative, unlike many studies on polycrystalline Cu electrodes where this peak only maintained at potentials close to zero[39]. It was possible that the activation of CO_2 or CO_3^{2-} species was facilitated by the $Mg(OH)_2$/MgO resulted from the stronger interactions with the support especially under more cathodic potentials. The peak at about 1515 cm^{-1} refers to the asymmetric stretching of C-O ($\nu_{as}CO$, **Fig. 3.13d**) from either the adsorbed carbonate ion or carboxylate intermediate ($*CO_2^-$). The peak has a red shift from -0.1 V to -0.45 V and the intensity significantly decreases to almost zero in the potential window from -0.45V to 0.6V. The disappearance of $\nu_{as}CO$ at deep reducing potential could be the sign of accelerated C-O bond breakage, after which the adsorbed *C=O intermediate would form. Considering the equilibrium of CO_3^{2-} and $*CO_2^-$ on the surface, the current data is insufficient to resolve these two species. Due to the gas bubble evolution in the current *in-situ* Raman cell, it is unable to measure to the potential (around -1V) where the adsorbed *CO intermediates are detectable.

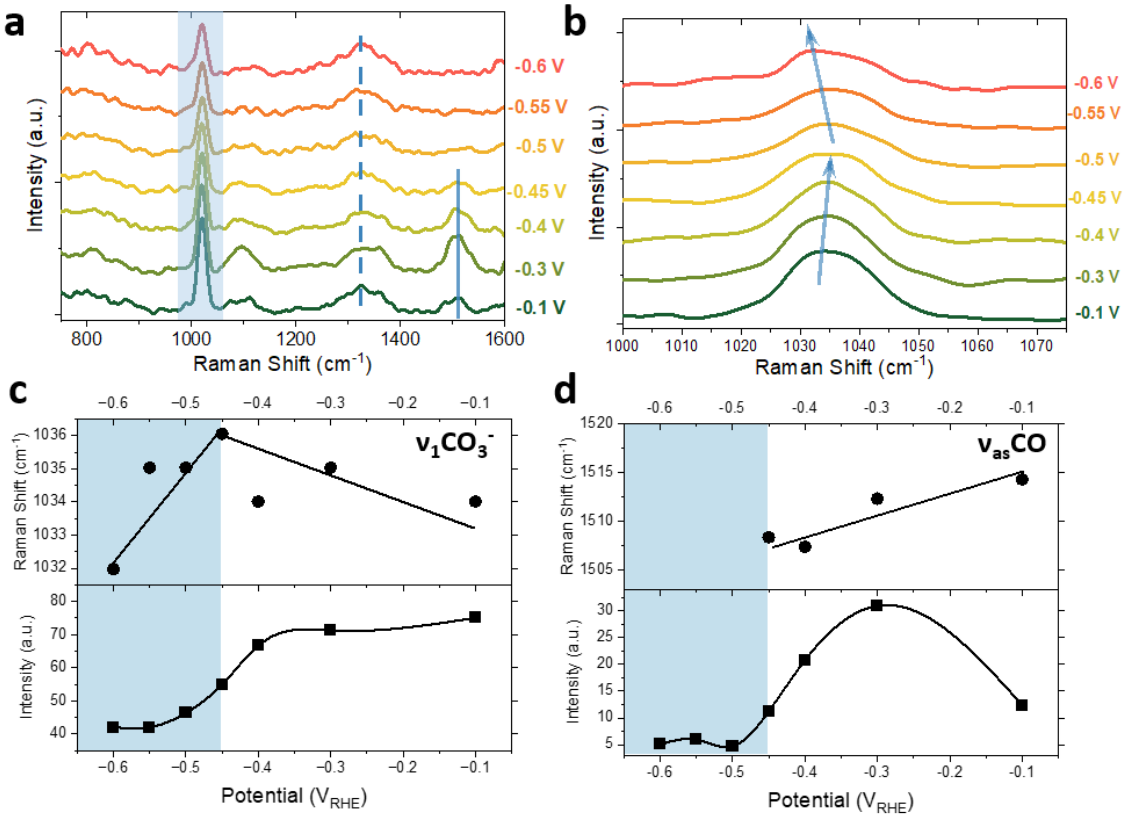


Figure 3.13 (a) Raman spectra of Cu-loaded $Mg(OH)_2$ calcined at 500 ºC (10Cu-500). **(b)** Enlarged spectra of 10Cu-500 with arrows indicating the trend of peak at around 1035 cm^{-1}. Correlation of peak shift and intensity distribution with applied potential: **(c)** $\nu_1CO_3^{2-}$, **(d)** $\nu_{as}CO$.

3.2.6 *In-situ* XAS Studies

Cu K-edge of 10Cu-500 sample was measured under ECR reaction conditions. **Fig. 3.14** shows the XANES spectra under dry condition (air), at open circuit potential (ocp), -0.5V and -1.9V (*vs.* RHE). Standard Cu foil and CuO spectra are also plotted for clearer comparison. Before assembling the electrode into the electrolyser, a weak pre-edge adsorption is observed at *ca.* 8978 eV from the electrode exposed to air (**Fig. 3.14** inset, blue curve) due to the quadrupole allowed 1s→3d transition of Cu(II) species. This confirms the existence of Cu(II) in 10Cu-500 samples which was originated from Cu surface oxidation after air exposure. After being in contact with electrolyte, the pre-edge adsorption peak is preserved and a shift toward higher binding energy indicates a further

oxidation of Cu took place under open circuit condition (**Fig. 3.14** inset, dark red curve). The reduction reactions at -0.5V shift the XANES spectra to the lower energy region and the pre-edge peak disappeared due to the reduction of Cu(II). A further reduction at -1.0V drives more Cu(II) species into lower valence states and a residual Cu(II) exists which could be told from the shape of white line adsorption peak at *ca.* 8997eV (**Fig. 3.14**, yellow curve).

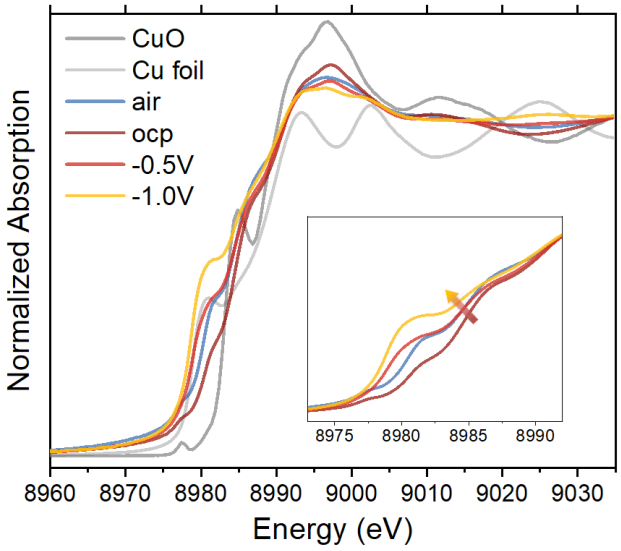


Figure 3.14 Cu K-edge XANES of 10Cu-500 sample measured under applied potentials during the measurement of ECR.

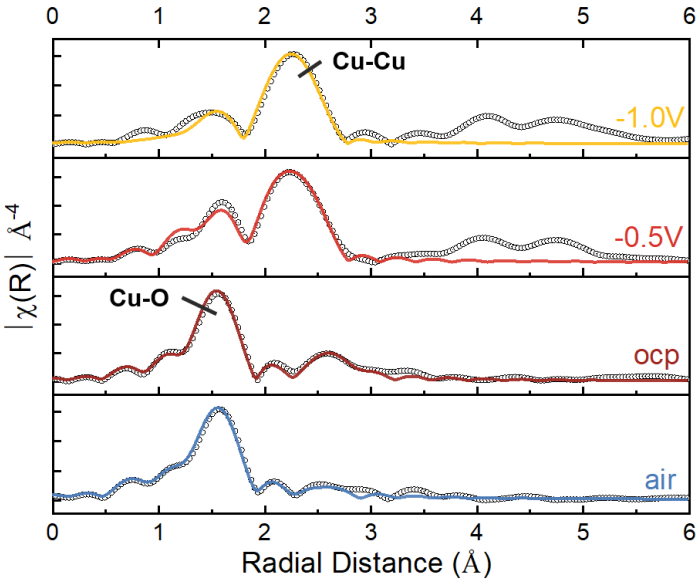


Figure 3.15 . R-space k^3 Cu K-edge Fourier-transformed EXAFS data (scatter) and first shell fitted results (solid line). Fitting range 1-3Å.

To confirm the Cu coordination state, fitting of EXAFS data was performed. CuO model is found to fit well with the EXAFS results measured in air and open circuit condition (**Fig. 3.15**, dark red and blue curve), which confirms the surface oxidation of Cu. The Cu-O bond could also stem from the Cu-MgO interface forming Cu-O-Mg sites. Cu-Cu metal bonding appears after the reduction reaction at -0.5V. The bond length of Cu-Cu_{Cu} decreases (**Table 3.1**) as the reduction potentials deepen, suggesting the gradual elimination of oxygen. A second shell coordination of Cu-Cu became visible between 4 and 5 Å (**Fig. 3.15**, red and yellow curve). A considerable amount of metallic copper formed during the reduction at -1.0V reflected by the drastically increasing of Cu-Cu coordination numbers to 6. The Cu-O still exists with a shortened bond length compared to CuO, which is likely to be the interfacial Cu-O bonding with the MgO support. The fitting results imply that Cu-O bonding was strengthened by the interaction with $MgO/Mg(OH)_2$ support.

Table 3.1 Structural Parameters, Bond Distance (R), and Coordination Number (CN) of Cu Obtained from EXAFS Analysis

Sample	**Scattering Path**	**R (Å)**	**CN**	**σ^2 (Å^2)**
air	$Cu\text{-}O_{CuO}$	1.95(1)	1.3(2)	0.006(2)
	$Cu\text{-}Cu_{CuO}$	2.93(1)	0.1(1)	0.006(2)
ocp	$Cu\text{-}O_{CuO}$	1.95(1)	1.5(2)	0.004(1)
	$Cu\text{-}Cu_{CuO}$	2.94(1)	0.3(1)	0.004(1)
$-0.5V_{RHE}$	$Cu\text{-}O_{Cu2O}$	1.86(3)	0.9(2)	0.007(1)
	$Cu\text{-}O_{CuO}$	1.98(3)	0.5(2)	0.007(1)
	$Cu\text{-}Cu_{Cu}$	2.56(2)	1.6(3)	0.007(1)
$-1.0V_{RHE}$	Cu-O	1.90(3)	1.4(4)	0.002(1)

$Cu\text{-}Cu_{Cu}$	2.56(3)	6.2(9)	0.008(1)

3.3 Conclusion

In this chapter, three proton-active supports (few-layer MoS_2, $Mg(OH)_2$ and MgO) were investigated. Their influence on ECR selectivity was identified by electrochemical performance tests and *in-situ* characterisations. The Cu-MoS_2 did not show any ECR selectivity in neutral conditions in PEM electrolyser due to the high activity of HER MoS_2. Both $Mg(OH)_2$ and MgO were found to provide a moderate acceleration of protonation to carbon intermediates resulting in a high selectivity of methane. The effect of the support was also reflected on the carbonate activation under negative potentials confirmed by Raman spectra. The MgO support showed a higher concentration of oxygen vacancies after Cu loading, and this effect would, in turn, help the Cu species maintaining the oxidised state and a stronger interface interaction with the support.

Overall, the MgO support performed the best with Cu particles well-dispersed on the surface. It is, however, not precise to draw the conclusion that Cu formed a single atom on the surface. Based on the TEM and EXAFS results, the distribution of Cu might not be 100% uniform and some area with quasi-stable Cu dispersion is sensitive to electric field. This correlates with the less stable ECR performance on the $Mg(OH)_2$/MgO series of catalysts. Not only the support would be hydrated and carbonated gradually during the reaction, but the Cu active sites might suffer a severe loss during a long-term measurement. Future work should focus on the stability of the Cu-loaded materials and a balanced point needs to be found between the C=O bond activation by the support and the corrosion to the catalysts surface to achieve a high and stable selectivity towards methane.

3.4 References

1. Y. Wu, C. Chen, X. Yan, R. Wu, S. Liu, J. Ma, J. Zhang, Z. Liu, X. Xing, Z. Wu and B. Han, Enhancing CO_2 electroreduction to CH4 over Cu nanoparticles supported on N-doped carbon, *Chem. Sci.*, 2022, **13**, 8388-8394.
2. Z.-H. Zhao, J.-R. Huang, P.-Q. Liao and X.-M. Chen, Isolated Tin(IV) Active Sites for Highly Efficient Electroreduction of CO_2 to CH_4 in Neutral Aqueous Solution, *Angew. Chem. Int. Ed.*, 2023, **62**, e202301767.
3. K. P. Kuhl, T. Hatsukade, E. R. Cave, D. N. Abram, J. Kibsgaard and T. F. Jaramillo, Electrocatalytic conversion of carbon dioxide to methane and methanol on transition metal surfaces, *J. Am. Chem. Soc.*, 2014, **136**, 14107-14113.
4. X. Chang, J. Li, H. Xiong, H. Zhang, Y. Xu, H. Xiao, Q. Lu and B. Xu, C−C Coupling Is Unlikely to Be the Rate-Determining Step in the Formation of C_{2+} Products in the Copper-Catalyzed Electrochemical Reduction of CO, *Angew. Chem. Int. Ed.*, 2022, **61**, e202111167.
5. T. Kim, A. Kargar, Y. Luo, R. Mohammed, E. Martinez-Loran, A. Ganapathi, P. Shah and D. P. Fenning, Enhancing C_2–C_3 Production from CO_2 on Copper Electrocatalysts via a Potential-Dependent Mesostructure, *ACS Appl. Energy Mater.*, 2018, **1**, 1965-1972.
6. J. H. Montoya, A. A. Peterson and J. K. Nørskov, Insights into C-C Coupling in CO_2 Electroreduction on Copper Electrodes, *ChemCatChem*, 2013, **5**, 737-742.
7. I. V. Chernyshova, P. Somasundaran and S. Ponnurangam, On the origin of the elusive first intermediate of CO_2 electroreduction, *Proc. Natl. Acad. Sci. U. S. A.*, 2018, **115**, E9261-E9270.
8. C.-J. Chang, S.-C. Lin, H.-C. Chen, J. Wang, K. J. Zheng, Y. Zhu and H. M. Chen, Dynamic Reoxidation/Reduction-Driven Atomic Interdiffusion for Highly Selective CO_2 Reduction toward Methane, *J. Am. Chem. Soc.*, 2020, **142**, 12119-12132.
9. X. Zhou, J. Shan, L. Chen, B. Y. Xia, T. Ling, J. Duan, Y. Jiao, Y. Zheng and S.-Z. Qiao, Stabilizing Cu_{2+} Ions by Solid Solutions to Promote CO_2 Electroreduction to Methane, *J. Am. Chem. Soc.*, 2022, **144**, 2079-2084.
10. M. Fang, Y. Ji, S. Geng, J. Su, Y. Li, Q. Shao and J. Lu, Metastable Metal–Alloy Interface in RuNi Nanoplates Boosts Highly Efficient Hydrogen Electrocatalysis, *ACS Appl. Nano Mater.*, 2022, **5**, 17496-17502.

11. W. Ren, X. Tan, J. Qu, S. Li, J. Li, X. Liu, S. P. Ringer, J. M. Cairney, K. Wang, S. C. Smith and C. Zhao, Isolated copper–tin atomic interfaces tuning electrocatalytic CO_2 conversion, *Nat. Commun.*, 2021, **12**, 1449.
12. C. Shen, P. Wang, L. Li, X. Huang and Q. Shao, Phase and structure modulating of bimetallic Cu/In nanoparticles realizes efficient electrosynthesis of syngas with wide CO/H_2 ratios, *Nano Research*, 2022, **15**, 528-534.
13. M. Ding, Z. Chen, C. Liu, Y. Wang, C. Li, X. Li, T. Zheng, Q. Jiang and C. Xia, Electrochemical CO_2 reduction: Progress and opportunity with alloying copper, *Mater. Rep., Energy*, 2023, **3**, 100175.
14. D. Kim, J. Resasco, Y. Yu, A. M. Asiri and P. Yang, Synergistic geometric and electronic effects for electrochemical reduction of carbon dioxide using gold–copper bimetallic nanoparticles, *Nat. Commun.*, 2014, **5**, 4948.
15. B. Zhou, P. Ou, N. Pant, S. Cheng, S. Vanka, S. Chu, R. T. Rashid, G. Botton, J. Song and Z. Mi, Highly efficient binary copper−iron catalyst for photoelectrochemical carbon dioxide reduction toward methane, *Proc. Natl. Acad. Sci.*, 2020, **117**, 1330-1338.
16. D. Gao, Y. Zhang, Z. Zhou, F. Cai, X. Zhao, W. Huang, Y. Li, J. Zhu, P. Liu, F. Yang, G. Wang and X. Bao, Enhancing CO_2 Electroreduction with the Metal–Oxide Interface, *J. Am. Chem. Soc.*, 2017, **139**, 5652-5655.
17. W. Zhou, X. Zou, S. Najmaei, Z. Liu, Y. Shi, J. Kong, J. Lou, P. M. Ajayan, B. I. Yakobson and J.-C. Idrobo, Intrinsic Structural Defects in Monolayer Molybdenum Disulfide, *Nano Lett.*, 2013, **13**, 2615-2622.
18. J. Lee, S. Kang, K. Yim, K. Y. Kim, H. W. Jang, Y. Kang and S. Han, Hydrogen Evolution Reaction at Anion Vacancy of Two-Dimensional Transition-Metal Dichalcogenides: Ab Initio Computational Screening, *J. Phys. Chem. Lett.*, 2018, **9**, 2049-2055.
19. L. Li, Z. Qin, L. Ries, S. Hong, T. Michel, J. Yang, C. Salameh, M. Bechelany, P. Miele, D. Kaplan, M. Chhowalla and D. Voiry, Role of Sulfur Vacancies and Undercoordinated Mo Regions in MoS_2 Nanosheets toward the Evolution of Hydrogen, *ACS Nano*, 2019, **13**, 6824-6834.
20. Y. Li, H. Wang, L. Xie, Y. Liang, G. Hong and H. Dai, MoS_2 Nanoparticles Grown on Graphene: An Advanced Catalyst for the Hydrogen Evolution Reaction, *J. Am. Chem. Soc.*, 2011, **133**, 7296-7299.

21. R. Siriwardane, J. Poston, K. Chaudhari, A. Zinn, T. Simonyi and C. Robinson, Chemical-Looping Combustion of Simulated Synthesis Gas Using Nickel Oxide Oxygen Carrier Supported on Bentonite, *Energy Fuels*, 2007, **21**, 1582-1591.
22. M. Back, M. Bauer, H. Stanjek and S. Peiffer, Sequestration of CO_2 after reaction with alkaline earth metal oxides CaO and MgO, *Appl. Geochem.*, 2011, **26**, 1097-1107.
23. A. Dal Pozzo, A. Armutlulu, M. Rekhtina, P. M. Abdala and C. R. Müller, CO_2 Uptake and Cyclic Stability of MgO-Based CO_2 Sorbents Promoted with Alkali Metal Nitrates and Their Eutectic Mixtures, *ACS Appl. Energy Mater.*, 2019, **2**, 1295-1307.
24. X. Huo, D. R. Conklin, M. Zhou, V. Vorotnikov, R. S. Assary, S. C. Purdy, K. Page, Z. Li, K. A. Unocic, R. I. Balderas, R. M. Richards and D. R. Vardon, Catalytic activity and water stability of the MgO(111) surface for 2-pentanone condensation, *Appl. Catal., B*, 2021, **294**, 120234.
25. T. Yoskamtorn, J. Mo, L. Chen, S. Wu, S. Mukhopadhyay, A. Hawkins, X.-P. Wu and S. C. E. Tsang, Exceptional Hydrogen Diffusion Rate over Ru Nanoparticle-Doped Polar MgO(111) Surface, *Small Methods*, 2023, **7**, 2201200.
26. S. Wu, K.-Y. Tseng, R. Kato, T.-S. Wu, A. Large, Y.-K. Peng, W. Xiang, H. Fang, J. Mo, I. Wilkinson, Y.-L. Soo, G. Held, K. Suenaga, T. Li, H.-Y. T. Chen and S. C. E. Tsang, Rapid Interchangeable Hydrogen, Hydride, and Proton Species at the Interface of Transition Metal Atom on Oxide Surface, *J. Am. Chem. Soc.*, 2021, **143**, 9105-9112.
27. M. G. Gardeh, A. A. Kistanov, H. Nguyen, H. Manzano, W. Cao and P. Kinnunen, Exploring Mechanisms of Hydration and Carbonation of MgO and $Mg(OH)_2$ in Reactive Magnesium Oxide-Based Cements, *J. Phys. Chem. C*, 2022, **126**, 6196-6206.
28. N. Liu, Y. Zhao, S. Zhou and J. Zhao, CO_2 reduction on p-block metal oxide overlayers on metal substrates—2D MgO as a prototype, *J. Mater. Chem. A*, 2020, **8**, 5688-5698.
29. J. Mo, S. Wu, T. H. M. Lau, R. Kato, K. Suenaga, T. S. Wu, Y. L. Soo, J. S. Foord and S. C. E. Tsang, Transition metal atom–doped monolayer MoS_2 in a proton-exchange membrane electrolyzer, *Mater. Today Adv.*, 2020, **6**, 100020.

30. E. Garand, T. Wende, D. J. Goebbert, R. Bergmann, G. Meijer, D. M. Neumark and K. R. Asmis, Infrared Spectroscopy of Hydrated Bicarbonate Anion Clusters: $HCO_3^-(H_2O)_{1-10}$, *J. Am. Chem. Soc.*, 2010, **132**, 849-856.
31. E. L. Clark, M. R. Singh, Y. Kwon and A. T. Bell, Differential Electrochemical Mass Spectrometer Cell Design for Online Quantification of Products Produced during Electrochemical Reduction of CO_2, *Anal. Chem.*, 2015, **87**, 8013-8020.
32. E. L. Clark and A. T. Bell, Direct Observation of the Local Reaction Environment during the Electrochemical Reduction of CO_2, *J. Am. Chem. Soc.*, 2018, **140**, 7012-7020.
33. A. J. Slifka, B. J. Filla and J. M. Phelps, Thermal Conductivity of Magnesium Oxide From Absolute, Steady-State Measurements, *J. Res. Natl. Inst. Stand. Technol.*, 1998, **103**, 357-363.
34. E. Carrasco, M. A. Brown, M. Sterrer, H.-J. Freund, K. Kwapien, M. Sierka and J. Sauer, Thickness-Dependent Hydroxylation of MgO(001) Thin Films, *J. Phys. Chem. C*, 2010, **114**, 18207-18214.
35. S. Clement and E. R. Hodgson, Radiation-enhanced impurity aggregation in MgO, *Phys. Rev. B*, 1987, **36**, 3359-3364.
36. D. M. Murphy, R. D. Farley, I. J. Purnell, C. C. Rowlands, A. R. Yacob, M. C. Paganini and E. Giamello, Surface Defect Sites Formed on Partially and Fully Dehydrated MgO: An EPR/ENDOR Study, *J. Phys. Chem. B*, 1999, **103**, 1944-1953.
37. K. M. Neyman, C. Inntam, A. V. Matveev, V. A. Nasluzov and N. Rösch, Single d-Metal Atoms on F_s and F_s^+ Defects of MgO(001): A Theoretical Study across the Periodic Table, *J. Am. Chem. Soc.*, 2005, **127**, 11652-11660.
38. Y. Li, D. An, Q. Zhang and Y. Wang, Copper-Catalyzed Selective Oxidation of Methane by Oxygen: Studies on Catalytic Behavior and Functioning Mechanism of CuO_x/SBA-15, *J. Phys. Chem. C*, 2008, **112**, 13700-13708.
39. I. V. Chernyshova, P. Somasundaran and S. Ponnurangam, On the origin of the elusive first intermediate of CO_2 electroreduction, *Proc. Natl. Acad. Sci.*, 2018, **115**, E9261-E9270.
40. D. Bhattacharyya, P. E. Videla, M. Cattaneo, V. S. Batista, T. Lian and C. P. Kubiak, Vibrational Stark shift spectroscopy of catalysts under the influence of electric fields at electrode–solution interfaces, *Chem. Sci.*, 2021, **12**, 10131-10149.

Chapter 4 Behaviours of Cu Nanoparticles in Alkaline and Neutral Electrolytes

4.1. Introduction

Copper particles have been widely studied in the regime of ECR in aqueous electrolytes. Its higher selectivity to hydrocarbons in contrast to other transition metals or non-metal catalysts, has made copper the only choice of electrocatalyst for multi-carbon production in ECR. Shapes[1], sizes[2], and doping[3]/alloys[4] of Cu crystals have been well studied in the past few decades. Electrolyte effects were also considered to improve the ECR efficiency by altering the cations[5, 6] and anions[7, 8]. These external factors may have great influence on the reactions taking place on the electrocatalysts yet the intrinsic mechanism on catalysts loaded GDE has never been explained clear. In this chapter, we synthesized Cu nanoparticles (NPs) with a size of about 20 nm as a model catalyst to study its ECR behaviours in different electrolytes.

Research on ECR usually focused on the performance and local environment on the catalysts surface by applying advanced *in-situ* characterisation techniques. Raman and IR spectroscopy can identify intermediates adsorbed on the electrode surface[9, 10], while the XAS and XPS unveil the local and surface environment of catalysts[11, 12]. However, the surface processes during the reactions have rarely been investigated on the electrode. Herein, we propose in this chapter that impedance spectroscopy could serve as a possible way to understand the states of ECR electrode surface.

Electrochemical impedance spectroscopy (EIS) has been widely used to determine the solution resistance between working and reference electrode before measuring any electro-catalytical reaction, as introduced in Chapter 2. Not only does it provide information on resistance change in electrochemical cell, but also on capacitance in the

double layer. There have been studies applying EIS for lithium-ion battery (LIB)[13, 14], solid oxide fuel cells (SOFC)[15, 16] and polymer electrolyte fuel cells[17, 18], but rarely on electrocatalytic studies[17, 19]. So far, there are few papers reporting on EIS studies for ECR in flow cells to the best of our knowledge, including one where the scientists studied the behaviours of carbon GDE with tin catalysts[20]. The cell applied in their research, however, is a traditional 3-electrode one-chamber cell with static electrolyte, which is far from the real ECR measurement conditions. While they proposed four features including the bicarbonate formation and the CO_2 activation from the spectrum, the true process of GDE in a flow cell under working conditions has remained unexplained.

For LIB where the conduction of ions such as Li^+ and O^{2-} in lattice could be well captured and decoupled by EIS, as the diffusive impedance usually dominates the low-frequency range. In catalytical reactions, researchers focus more on the adsorption of intermediates on the electrode. Interfacial process tends to fall between the high frequency range where the electrolyte resistance dominates and the low frequency for the diffusion of ions[21]. It is, therefore, cannot be easily distinguished and decoupled to elementary or unit steps.

To distinguish the different processes, a model circuit was designed based on the understanding of ECR cell applied in this project. The minimised electrolyte layer allows fast diffusion of ion in the solution and, therefore, a small electrolyte resistance of less than 3Ω was guaranteed which was represented by R_S in the model circuit. To capture the basic electrode surface behaviours, both Faradaic and non-Faradaic current were considered. This resulted in the simple Randles circuit with one charge transfer resistance and one double-layer capacitance connected in parallel[22]. Moving closer to the electrode surface in ECR cells, two Randles circuits connected in series are chosen to represent the complicate multiple surface steps related with ions, intermediates, and charge transfer. This model circuit successfully fits in with the target of decoupling proton-related and

carbon-related process by replacing the double-layer capacitance with the constant phase element (CPE) which fits better with the real electrode behaviours. The alkaline condition allows an intensive carbon-related species in high-frequency region, while the neutral condition leads to a strengthened proton-related process in low-frequency region.

Further to the understanding of electrolyte effects, the surface oxide layer generated intrinsically appeared on the Cu particles during handling attracted our attention. The Cu_2O layer plays a role in protecting the inner metallic component from structural change. The enhanced resistance to external oxidation/reduction maintains its original morphology and reactivity. This chapter focuses on the external effects of ECR. Instead of designing various catalysts and comparing their reactivity, the electrolyte, air and even the cell design could have exerted certain influence on the performance. In the future, the understanding to the electrode surface related with the reaction kinetics would be an interesting topic to discuss.

4.2. Results and Discussion

Synthesis methods and notations of the materials involved in this chapter can be found in previous sections 2.3.5 and 2.3.6. *In-situ* XAS measurements were described in section 2.3.16.

4.2.1. XRD

The XRD patterns in **Figure 4.1** shows the lattice composition of Cu nanoparticles with different synthetic duration from 1 hour to 6 hours at 250 ºC. The facets in these samples were similar, with Cu(111) as the dominant facet accompanied by Cu(200) and Cu(220). All samples were slightly oxidized after the exposure to air, which led to the formation of Cu_2O(111). This Cu(I) phase was likely to exist on the surface, forming a protection layer

to the Cu(0) in the bulk particles[23]. Due to the limited amount of oxidation species on the surface, it is believed that the oxidation caused by air would not affect the reduction reaction performance. The peaks were broadened due to the small particle sizes (<25 nm). The intensity of peaks in each sample varies due to the loading amount of sample onto the XRD holder, whereas the relative intensity of peaks from the same sample remains the same.

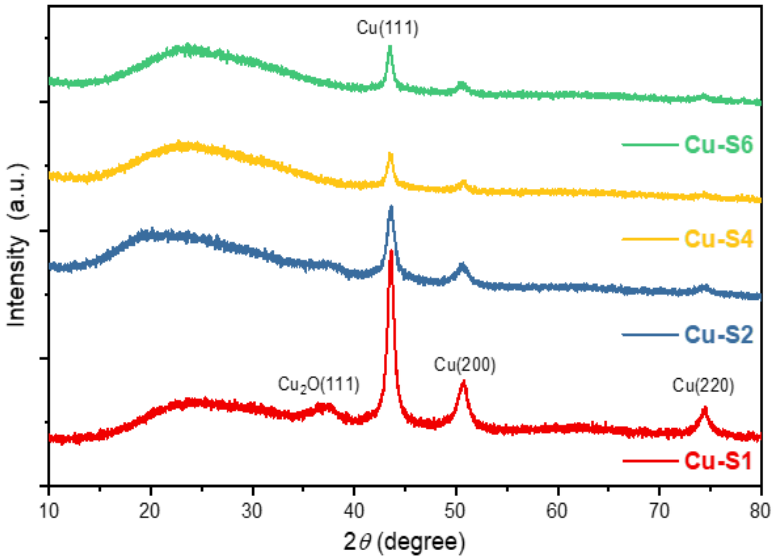


Figure 4.1 XRD patterns of Cu particle samples Cu-S1, S2, S4 and S6.

For comparison, controlled CuO_x samples with larger grain sizes were synthesized. By calcining at 400 ºC, cupric oxalate decomposed and released CO_2 and CO, which resulted in the formation of copper oxides[24]. Under inert gas, Cu(0) was the main composition with Cu(111), (200) and (220) exposed. Cu(I) phase was also generated during this process as the oxygen atoms could remain in the Cu lattice when CO molecules removed. Under the air condition, only CuO was detected. The XRD patterns of these CuO_x samples was shown in **Fig. 4.2**. Same as the Cu particle samples shown in **Fig. 4.1**, the dominant Cu(0) facet was the (111) plane and the major Cu(I) was the Cu_2O (111). As the calcination temperature of the CuO_x samples were much higher than the reduction

method for Cu particles, the crystallinity of CuO_x was much better. The shape of the peaks in **Fig. 4.2** are sharper than those in **Fig. 4.1**, which also indicates that the grain sizes of CuO_x were likely to be larger than Cu nanoparticles synthesized previously.

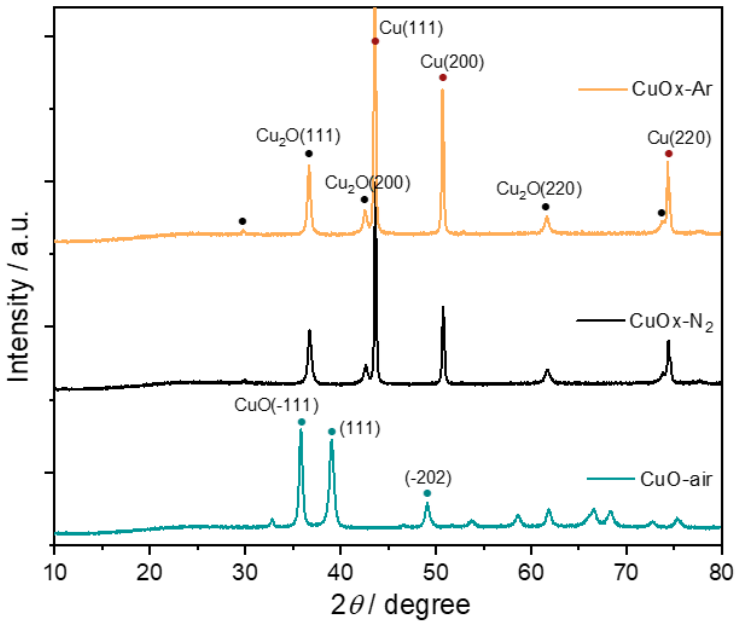


Figure 4.2 XRD patterns of commercial Cu oxalate calcined under different gas atmospheres.

4.2.2. TEM

TEM images were captured both before and after the reaction with Cu-S1 electrocatalysts. The images show that the copper particle size was around 20 nm (**Fig. 4.3a**) and lattice distance measured from the HRTEM images was about 0.23 Å (**Fig. 4.3b, c**). This value was higher than the d space of (111) plane in copper metal (0.208 Å) while slightly lower than that of Cu_2O (0.246 Å). Such findings agree with the observation from XRD patterns, where the existence of Cu_2O was also confirmed. The existence of surface oxygen leading to the expansion of Cu lattice could explain such deviation[25].

The Cu NPs after the ECR reaction were collected from the electrode and TEM images indicated the aggregation of particles happening during the reaction (**Fig. 4.4a**). Interestingly, the aggregation of particles did not eliminate the lattice defects. It could be confirmed from the inset SAED and inverse FFT that polycrystalline Cu formed near the interface of two aggregated particles. The creation of such grain boundaries could, in turn, serve as active sites for ECR[26]. Furthermore, there are particles that could preserve the defects on the surface, including a line defect shown in **Fig. 4.4b**. It is, however, still uncertain whether the forced depletion of oxygen from surface by applying negative potentials would assist the preservation of such defects due to a lack of operando characterisation during the reactions in this current project.

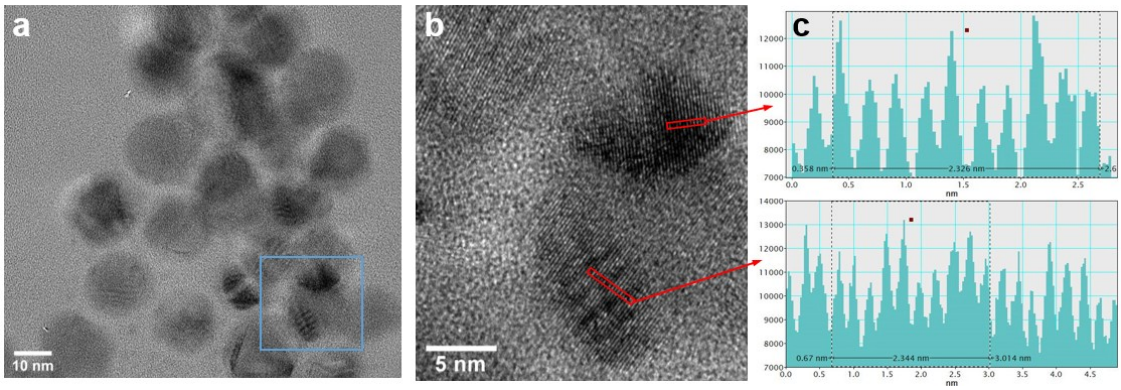


Figure 4.3 (a) HRTEM image of Cu-S1; blue box marked the enlarge area in **(b)**; red boxes and arrows marked **(c)** the line profile area.

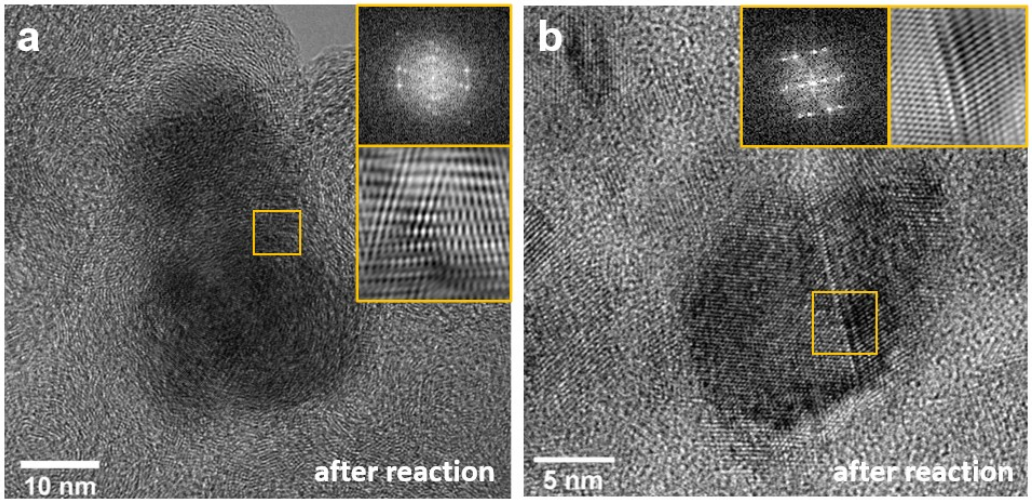


Figure 4.4 (a) and **(b)** HRTEM images of Cu-S1 aggregated particles after reaction. Yellow boxes highlight the area for selected area electron diffraction (SAED) and inverse FFT showing different types of defects.

4.2.3. Electrode Morphologies

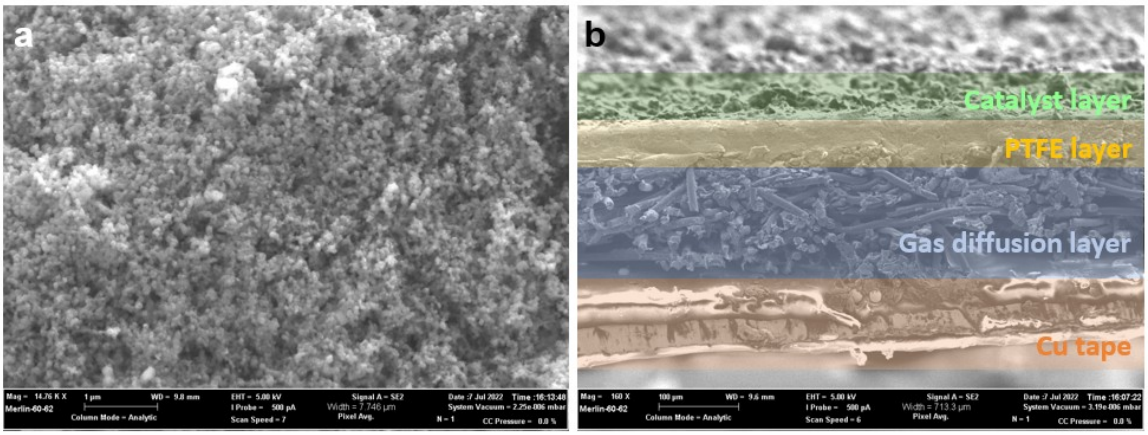


Figure 4.5 (a) SEM images and **(b)** cross-section SEM images of Cu-S1 samples sprayed on a carbon GDE.

From the SEM images of GDE loaded with catalysts Cu-S1, the electrode surface was not completely uniform (**Fig. 4.5a**) within the catalysts layer. The cross-section images indicate the thickness of catalyst layer ranging from a few to ten micrometres (**Fig. 4.5b**). Considering this, the manufacture of working electrodes used in this project added an extra carbon layer made of graphite and carbon black to protect and interconnect the catalyst layer. With this protection, it is believed that the hydrophobicity of electrode surface would increase, and benefit the overall performance of ECR[27].

4.2.4. ECR Performance

In 1M KOH, Cu particles selectively reduced CO_2 into C_2H_4 with the FE up to 35% in a wide potential window from -0.8 V to -1.0 V (**Fig. 4.6a**). In contrast, the selectivity to CH_4 was significantly higher than ethylene in 0.5M K_2SO_4 on the same Cu catalyst, peaking at -1.56 V with the FE of methane to nearly 40% (**Fig. 4.6b**).

The ECR performance of CuO_x samples were also tested in the same setup. The CuO_x-N_2 sample showed high CO selectivity from -0.9 V. The CO selectivity decreased and C_2H_4 selectivity increased as the potential became more negative, indicating the transformation from CO into C_2 products. The overall gas efficiency also decreased to less than 90% at -1.12 V, which implies the formation of liquid products in the electrolyte. Compared to Cu particle samples, the overpotential of CuO_x-N_2 sample was 0.3V higher targeting at ethylene due to a lack of grain boundaries. For CuO_x-Ar sample, the gas phase products had a limited efficiency less than 65% across the measured potential range. Although the C_2 selectivity were at the same level as the Cu-S1 sample at around -1.0 V, this sample favoured the production of liquid products dominant by formic acid.

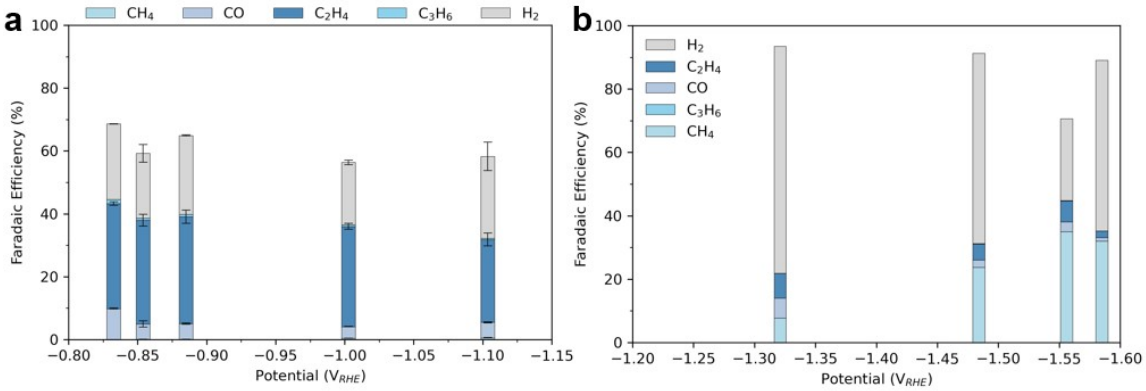


Figure 4.6 Gas products distribution of ECR on Cu NPs in **(a)**1M KOH and **(b)** 0.5M K_2SO_4.

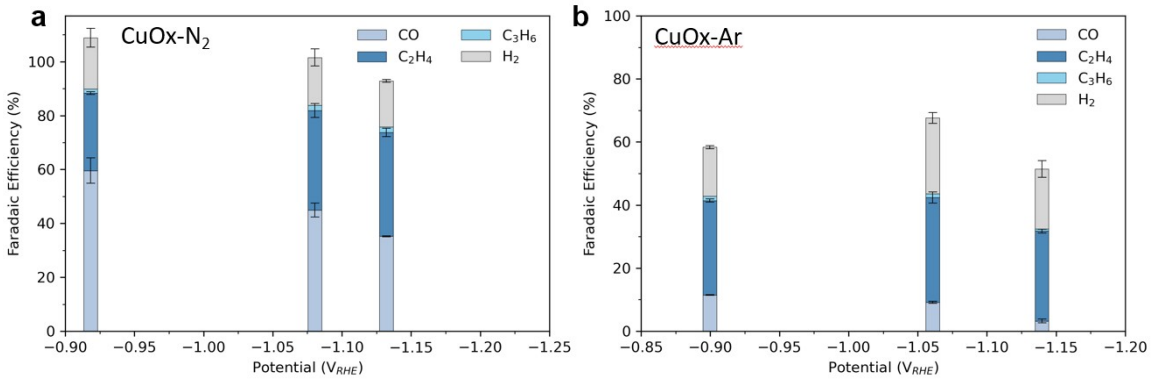


Figure 4.7 Gas products distribution of ECR on **(a)** CuO_x-N_2 and **(b)** CuO_x-Ar in 1 M KOH.

4.2.5. EIS Scans

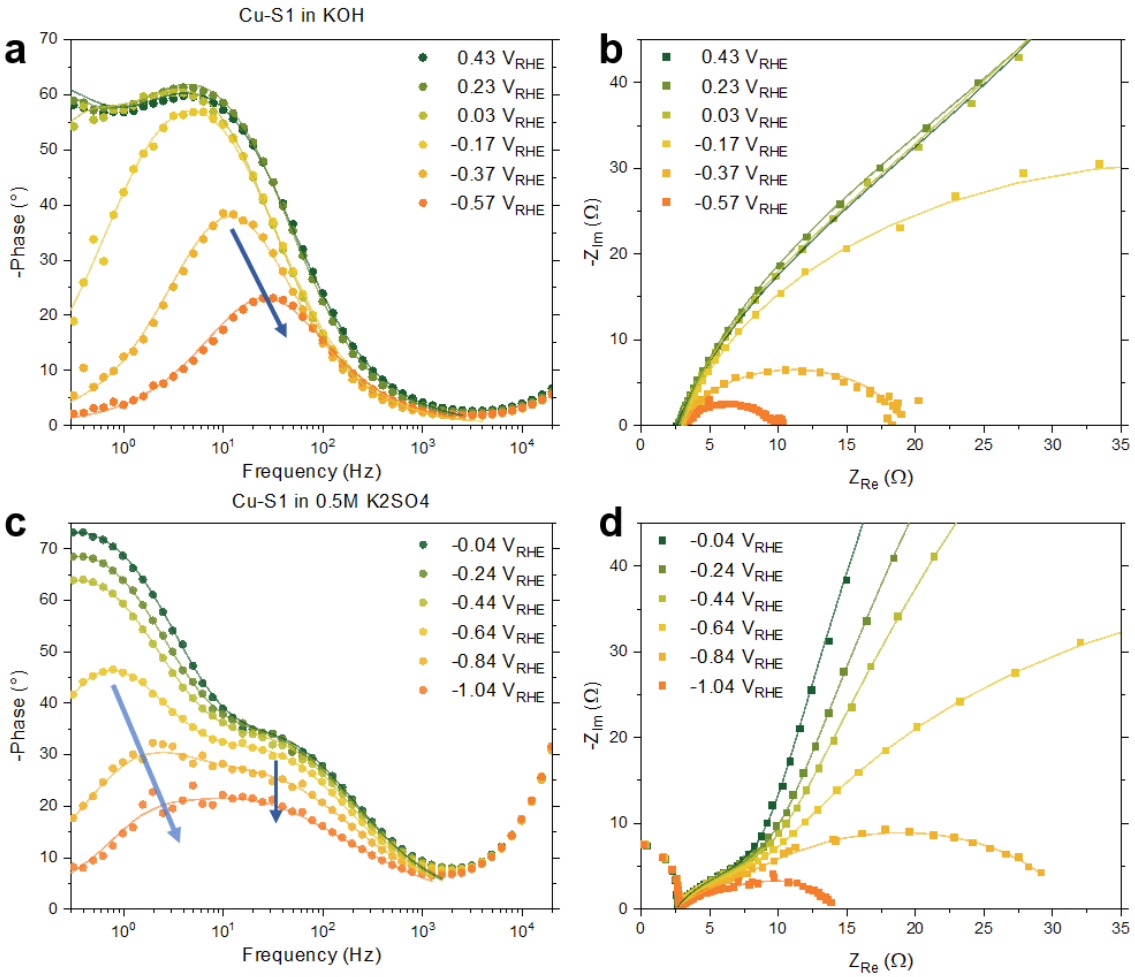


Figure 4.8 (a) Bode plot in phase angle and **(b)** Nyquist plot of EIS spectra on Cu NPs in 1M KOH. **(c)** Bode plot in phase angle and **(d)** Nyquist plot of EIS spectra on Cu NPs in 1M K_2SO_4. Bode plot in total impedance can be found in **Fig. A4**

The EIS in 1M KOH was measured at different potentials from 0.4 V to -0.4 V, covering the current density ranging from 1 $mA \cdot cm^{-2}$ to 30 $mA \cdot cm^{-2}$. The first three scans shown in Bode plot (**Fig. 4.8a**) had frequency distribution similarly to the EIS under OCP condition indicating that the potentials have not reached the onset point. From the fourth scan (yellow dots and line), a charge transfer step is identified, and the characteristic frequency increases as the applied potential becomes more negative. In the neutral electrolyte, however, the EIS scans from 0 V to -1 V (same current range) are composed

of two separated charge transfer processes (**Fig. 4.8c**). The lower frequency step behaved similarly to the one in alkaline environment. The step with higher frequency showed much less response to potential changes compared to the low frequency step. So far, it could be concluded that the high frequency step related with carbon species essential to produce ethylene and methane; while the low frequency step resulted more from the proton diffusion or protonation that favours methane or H_2 production when flooding happens.

The Nyquist plot provides information on the magnitude of impedance. The alkaline plot in **Fig. 4.8b** shows a charge transfer resistance smaller than 20 Ω under polarization (current density > 20 $mA \cdot cm^{-2}$ at -0.37V), while the neutral electrolyte results in the resistance of over 30 Ω at a similar current density (**Fig. 4.8d**). It is also clear that the alkaline condition showed a single semi-circle arc, which agrees with the existence of only one charge transfer steps related to carbon species with a characteristic frequency of 15.8 Hz at -0.57 V. In comparison, the neutral condition has a curved composed of at least two semi-circles in the Nyquist plot implying a multi-step charge transferring steps taking place. It is still controversial to identify process according to their characteristic frequencies for now[28]. And the reported frequencies on electrocatalytic electrodes fall in the range of 10^0 to 10^2Hz, in consistent with our observations[29].

The two parallel resistors and constant phase elements (R||CPE) in the model circuit were chosen and identified by the shapes of Nyquist which composed of at least two depressed semicircles. Though it was possible to achieve a better fitting result by adding more R|| CPE circuits, the excessive units usually could not be explained accurately and would not have specific physical meanings. Resistance values in **Fig. 4.8 a, c** share a similar trend that decreased from 10^3 to 10^0 Ω for resistor R1 as the potential decreased to -1.0V. This indicated polarization reactions with similar kinetics taking place on the electrodes in

KOH and K_2SO_4 electrolyte. The calculated capacitance of CPE1 in alkaline environment, however, was around ten times smaller than that of neutral electrolyte, which was due to the limited proton-related adsorption sites on the electrode surface under alkaline environment compared to neutral one.

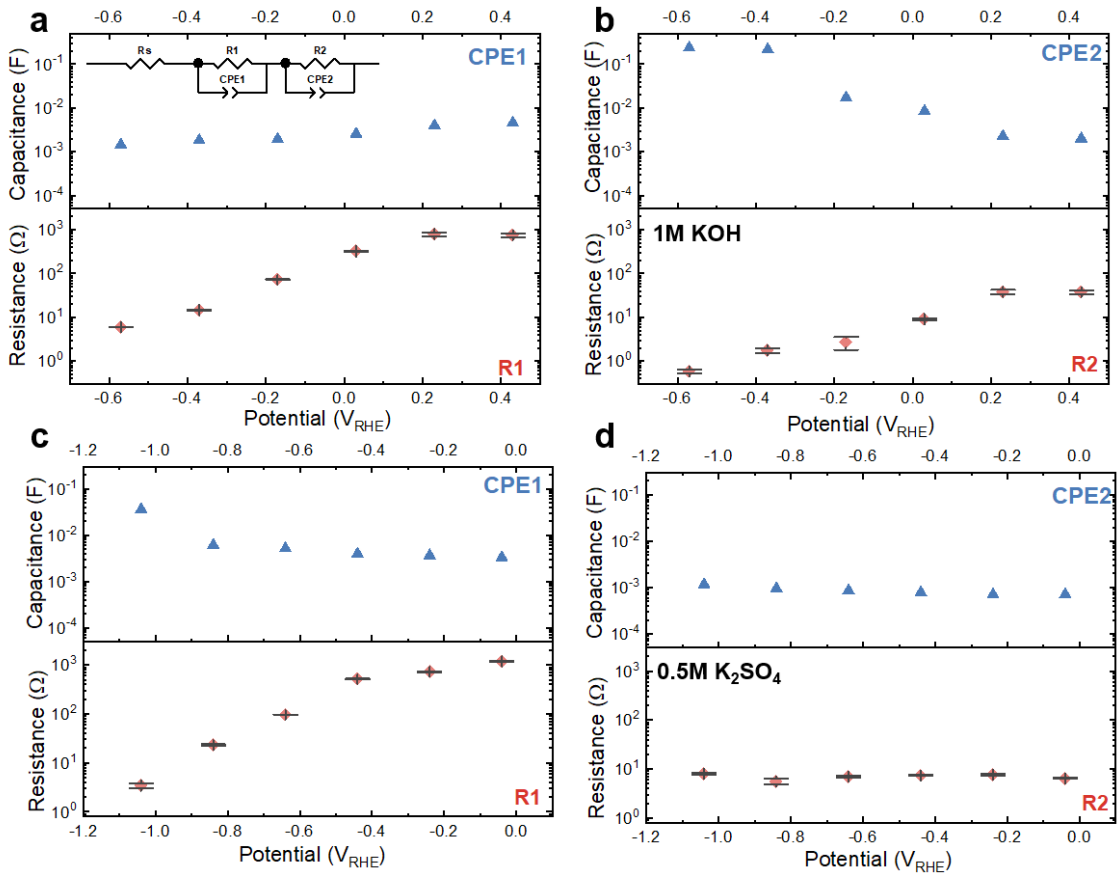


Figure 4.8 Capacitance and resistance values calculated from the fitting results of **(a)** CPE1 and R1, **(b)** CPE2 and R2 for Cu-S1 ECR electrocatalysts in 1M KOH. The model circuit for fitting was shown as an inset, where Rs represented the solution resistance between WE and RE. Capacitance and resistance values calculated from the fitting results of **(c)** CPE1 and R1, **(d)** CPE2 and R2 for Cu-S1 ECR electrocatalysts in 0.5M K_2SO_4.

The second R||CPE unit in **Fig. 4.8b**, **d** shows different behaviours in both the resistance and capacitance. The alkaline condition allowed another polarization process on the electrode as indicated by the decreased resistance of R2 in **Fig. 4.8b**. In the neutral electrolyte, the resistance hardly changed with the potentials and the capacitance values

also remained at the same magnitude. It could, therefore, be concluded that this R||CPE unit in neutral electrolyte represented a step independent from applied potentials. In the perspective of capacitance, the CPE2 in KOH exhibited an increasing capacitance up to 10^{-1} F magnitude, whereas the K_2SO_4 remained in the10^{-3} F level. The increased capacitance implies a charging process to the electrode in alkaline condition, which was a non-faradaic process that could be related to the adsorption of carbon intermediates on the surface of electrodes. The absence of this process in neutral electrolyte with limited C_2 efficiency suggested its relationship with C-C coupling. As the calculations have pointed out that certain C_2 intermediates with large dipole moments were sensitive to electric fields on the interface[30], the higher capacitance induced by potentials in alkaline electrolyte from EIS studies could explain the selectivity difference between C_1 and C_2[31].

4.2.6. Cu Coordination Environment

To further obtain the structural information from material on electrodes, XAS measurements were performed on the GDE with catalysts layer and carbon layer. EXFAS confirms the formation of Cu-O bond with a CN number of around 2 (**Table 4.1**), consistent with Cu_2O structure with linear O-Cu-O bond that was proposed to form on the surface of Cu particles in section 4.2.1. The Cu-Cu path had a supressed fist-shell coordination with only 4 Cu atoms. This was due to the small size of the particles and the varieties of defects that have been observed by TEM in **Fig. 4.4**.

Table 4.1 Fitting Parameters of Cu-S1 sample on GDE.

Sample	**Scattering Path**	**R (Å)**	**CN**	**σ^2 (Å^2)**
Cu-S1	Cu-O	1.895(6)	2.2(2)	0.008(1)
	Cu-Cu	2.561(2)	4.5(1)	0.010(1)

The EXAFS results in R-space of Cu-S1 on GDE sample show a clear first shell Cu-Cu bonding at around 2.56 Å as well as the second coordination shell belonging to metallic copper (**Fig. 4.9**), which confirms the existence of Cu(0) as the major component. A closer look through the wavelet transformation results in **Fig. 4.10** indicate the Cu-O bonding with lower intensity compared to Cu-Cu, which agrees with the surface Cu_2O phase that protects the Cu particles from further oxidation.

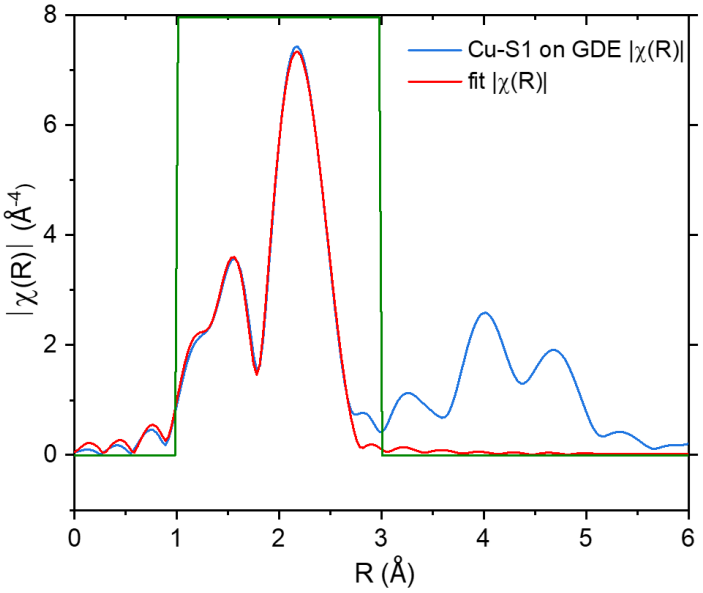


Figure 4.9 EXAFS of Cu K edge in R space of Cu-S1 on GDE.

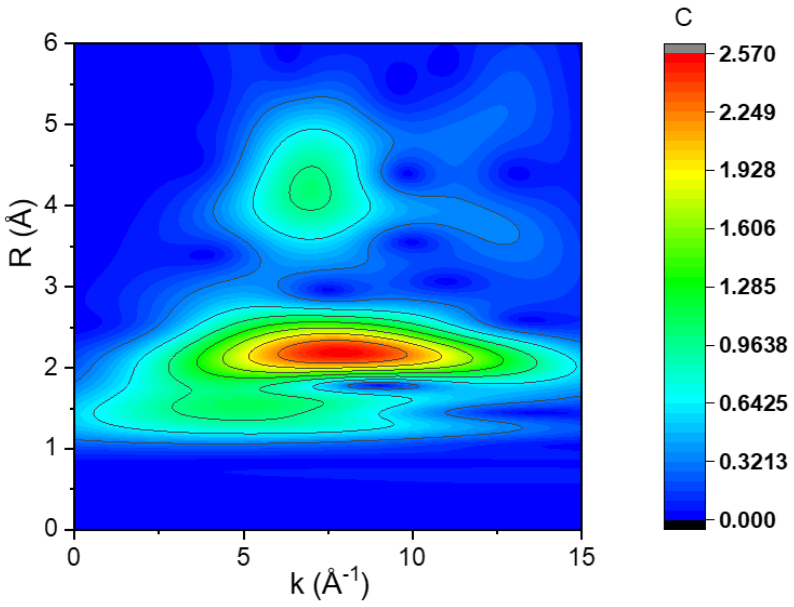


Figure 4.10 Wavelet transform of Cu K edge of Cu-S1 on GDE.

Compared with the intrinsic protected Cu(0) nanoparticles, the calcined CuO_x samples showed less resistance to air oxidation. The as-synthesized CuO_x-N_2 powder has a small portion of Cu-O bond intensity shown in **Fig. 4.11a, c**. After the loading of catalysts onto GDE, the oxidation progressed and a significant increment on the first shell Cu-O scattering in **Fig. 4.11b, d** suggests the further oxidation of the materials. Such vulnerability to air could result in the elimination of surface defects formed in the original Cu lattice via calcination. During the insertion of oxygen atoms into the Cu lattice, the grain boundaries might be destroyed, and the aggregation of defects was separated. The increasing distance among possible active sites led to the high CO selectivity in contrast to the Cu particles samples which possessed a better resistance to air to retain its intrinsic C_2 activity.

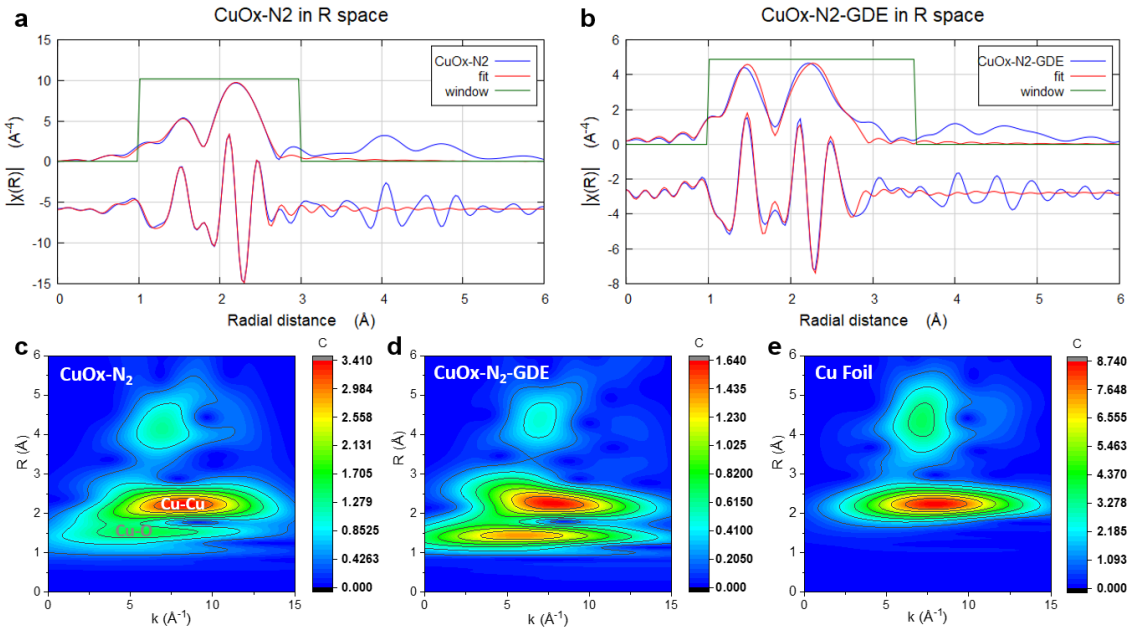


Figure 4.11 EXAFS of Cu K edge in R space of **(a)** CuO_x-N_2 and **(b)** after sprayed on GDE. Wavelet transform of Cu K edge of **(c)** CuO_x-N_2 and **(d)** after sprayed GDE and **(e)** Cu Foil.

4.3. Conclusion

In Chapter 4, the effects of electrolyte and air interference in ECR were investigated through the model catalysts Cu particles with XRD, TEM, SEM, EIS and XAS. Comparing with the neutral electrolyte, alkaline electrolyte exhibited a higher capacity of intermediates adsorption on the electrode surface. The EIS studies unveiled the possible origin of such ability by applying a small potential perturbation to the ECR cell. The effective capacitance of CPE in the model circuit was extracted to explain the difference. A more than 10^2 magnitude higher capacitance was observed under alkaline conditions in the carbon-related electrode process. With such capacity, the concentration of adsorbed carbon intermediates was increased, which was reflected by the higher selectivity to C_2 than C_1 products in alkaline electrolytes.

The air interference of Cu particles was relieved by the formation of surface Cu_2O layer in Cu NPs. Without such oxide layer, the oxidation of Cu would be further oxidised during the GDE preparation steps and affected the performance. The lack of uniform Cu_2O layer on the CuO_x catalysts studied in this chapter had a C_2 selectivity less than 25% in alkaline condition, whereas the protected Cu particles sample showed a much higher selectivity of up to 40% with a lower overpotential. Therefore, the oxide passivation layer assisted the preservation of intrinsic structure of as synthesized catalysts from changes during the post manufacturing steps.

Overall, the role of electrolyte and air in ECR were explored in this project. A further investigation should include the calculations on theoretical models as another evidence to support the existing conclusions. Future work could focus on the structural changes of catalysts during the reactions and the remove of oxygen atoms from the catalysts during the electrochemical reduction. The influence from the external electric fields could either be illustrated by *in-situ* measurements or theoretical calculations on the model Cu slab.

4.4. References

1. A. Loiudice, P. Lobaccaro, E. A. Kamali, T. Thao, B. H. Huang, J. W. Ager and R. Buonsanti, Tailoring Copper Nanocrystals towards C_2 Products in Electrochemical CO_2 Reduction, *Angew. Chem. Int. Ed.*, 2016, **55**, 5789-5792.
2. K. Rossi and R. Buonsanti, Shaping Copper Nanocatalysts to Steer Selectivity in the Electrochemical CO_2 Reduction Reaction, *Acc. Chem. Res.*, 2022, **55**, 629-637.
3. X. K. Lu, B. Lu, H. Li, K. Lim and L. C. Seitz, Stabilization of Undercoordinated Cu Sites in Strontium Copper Oxides for Enhanced Formation of C2+ Products in Electrochemical CO_2 Reduction, *ACS Catal.*, 2022, **12**, 6663-6671.
4. H. Lv, F. Lv, H. Qin, X. Min, L. Sun, N. Han, D. Xu, Y. Li and B. Liu, Single-Crystalline Mesoporous Palladium and Palladium-Copper Nanocubes for Highly Efficient Electrochemical CO_2 Reduction, *CCS Chemistry*, 2022, **4**, 1376-1385.
5. M. R. Singh, Y. Kwon, Y. Lum, J. W. Ager, III and A. T. Bell, Hydrolysis of Electrolyte Cations Enhances the Electrochemical Reduction of CO_2 over Ag and Cu, *J. Am. Chem. Soc.*, 2016, **138**, 13006-13012.
6. L. D. Chen, M. Urushihara, K. Chan and J. K. Nørskov, Electric Field Effects in Electrochemical CO_2 Reduction, *ACS Catal.*, 2016, **6**, 7133-7139.
7. D. Gao, F. Scholten and B. Roldan Cuenya, Improved CO_2 Electroreduction Performance on Plasma-Activated Cu Catalysts via Electrolyte Design: Halide Effect, *ACS Catal.*, 2017, **7**, 5112-5120.
8. J. Resasco, Y. Lum, E. Clark, J. Z. Zeledon and A. T. Bell, Effects of Anion Identity and Concentration on Electrochemical Reduction of CO_2, *ChemElectroChem*, 2018, **5**, 1064-1072.
9. I. V. Chernyshova, P. Somasundaran and S. Ponnurangam, On the origin of the elusive first intermediate of CO_2 electroreduction, *Proc. Natl. Acad. Sci.*, 2018, **115**, E9261-E9270.
10. Y. Kim, S. Park, S.-J. Shin, W. Choi, B. K. Min, H. Kim, W. Kim and Y. J. Hwang, Time-resolved observation of C–C coupling intermediates on Cu electrodes for selective electrochemical CO_2 reduction, *Energy Environ. Sci.*, 2020, **13**, 4301-4311.
11. N. J. Firet, T. Burdyny, N. T. Nesbitt, S. Chandrashekar, A. Longo and W. A. Smith, Copper and silver gas diffusion electrodes performing CO_2 reduction studied

through operando X-ray absorption spectroscopy, *Catal. Sci. Technol.*, 2020, **10**, 5870-5885.

12. A. A. Permyakova, J. Herranz, M. El Kazzi, J. S. Diercks, M. Povia, L. R. Mangani, M. Horisberger, A. Pătru and T. J. Schmidt, On the Oxidation State of $_{Cu}2O$ upon Electrochemical CO_2 Reduction: An XPS Study, *ChemPhysChem*, 2019, **20**, 3120-3127.
13. P. K. Jones, U. Stimming and A. A. Lee, Impedance-based forecasting of lithium-ion battery performance amid uneven usage, *Nat. Commun.*, 2022, **13**, 4806.
14. U. Tröltzsch, O. Kanoun and H.-R. Tränkler, Characterizing aging effects of lithium ion batteries by impedance spectroscopy, *Electrochim. Acta*, 2006, **51**, 1664-1672.
15. M. J. Jørgensen, S. Primdahl and M. Mogensen, Characterisation of composite SOFC cathodes using electrochemical impedance spectroscopy, *Electrochim. Acta*, 1999, **44**, 4195-4201.
16. Q.-A. Huang, R. Hui, B. Wang and J. Zhang, A review of AC impedance modeling and validation in SOFC diagnosis, *Electrochim. Acta*, 2007, **52**, 8144-8164.
17. Y. Wu, Q. Meyer, F. Liu, L. Rasha, J. I. S. Cho, T. P. Neville, J. Millichamp, R. Ziesche, N. Kardjilov, P. Boillat, H. Markötter, I. Manke, M. Cochet, P. Shearing and D. J. L. Brett, Investigation of water generation and accumulation in polymer electrolyte fuel cells using hydro-electrochemical impedance imaging, *J. Power Sources*, 2019, **414**, 272-277.
18. V. A. Paganin, C. L. F. Oliveira, E. A. Ticianelli, T. E. Springer and E. R. Gonzalez, Modelisticinterpretation of the impedance response of a polymer electrolyte fuel cell1Presented in part at the 192nd Meeting of The Electrochemical Society, Paris, France, 1997.1, *Electrochim. Acta*, 1998, **43**, 3761-3766.
19. S. Anantharaj and S. Noda, Appropriate Use of Electrochemical Impedance Spectroscopy in Water Splitting Electrocatalysis, *ChemElectroChem*, 2020, **7**, 2297-2308.
20. F. Bienen, D. Kopljar, A. Löwe, S. Geiger, N. Wagner, E. Klemm and K. A. Friedrich, Revealing Mechanistic Processes in Gas-Diffusion Electrodes During CO_2 Reduction via Impedance Spectroscopy, *ACS Sustainable Chemistry & Engineering*, 2020, **8**, 13759-13768.

21. S. Wang, J. Zhang, O. Gharbi, V. Vivier, M. Gao and M. E. Orazem, Electrochemical impedance spectroscopy, *Nature Reviews Methods Primers*, 2021, **1**, 1-21.
22. A. R. C. Bredar, A. L. Chown, A. R. Burton and B. H. Farnum, Electrochemical Impedance Spectroscopy of Metal Oxide Electrodes for Energy Applications, *ACS Appl. Energy Mater.*, 2020, **3**, 66-98.
23. S. Uk Son, I. Kyu Park, J. Park and T. Hyeon, Synthesis of Cu_2O coated Cu nanoparticles and their successful applications to Ullmann-type amination coupling reactions of aryl chlorides, *Chem. Commun.*, 2004, DOI: 10.1039/B316147A, 778-779.
24. E. Lamprecht, G. M. Watkins and M. E. Brown, The thermal decomposition of copper(II) oxalate revisited, *Thermochim. Acta*, 2006, **446**, 91-100.
25. G. Zhou, L. Luo, L. Li, J. Ciston, E. A. Stach and J. C. Yang, Step-Edge-Induced Oxide Growth During the Oxidation of Cu Surfaces, *Phys. Rev. Lett.*, 2012, **109**, 235502.
26. Q. Wu, R. Du, P. Wang, G. I. N. Waterhouse, J. Li, Y. Qiu, K. Yan, Y. Zhao, W.-W. Zhao, H.-J. Tsai, M.-C. Chen, S.-F. Hung, X. Wang and G. Chen, Nanograin-Boundary-Abundant Cu_2O-Cu Nanocubes with High C2+ Selectivity and Good Stability during Electrochemical CO_2 Reduction at a Current Density of 500 mA/cm2, *ACS Nano*, 2023, **17**, 12884-12894.
27. C.-T. Dinh, T. Burdyny, M. G. Kibria, A. Seifitokaldani, C. M. Gabardo, F. P. García de Arquer, A. Kiani, J. P. Edwards, P. De Luna, O. S. Bushuyev, C. Zou, R. Quintero-Bermudez, Y. Pang, D. Sinton and E. H. Sargent, CO_2 electroreduction to ethylene via hydroxide-mediated copper catalysis at an abrupt interface, *Science*, 2018, **360**, 783-787.
28. H. Warkentin, C. P. O'Brien, S. Holowka, B. Maxwell, M. Awara, M. Bouman, A. S. Zeraati, R. Nicholas, A. H. Ip, E. S. Elsahwi, C. M. Gabardo and D. Sinton, Early Warning for the Electrolyzer: Monitoring CO_2 Reduction via In-Line Electrochemical Impedance Spectroscopy, *ChemSusChem*, 2023, e202300657.
29. F. Bienen, D. Kopljar, S. Geiger, N. Wagner and K. A. Friedrich, Investigation of CO_2 Electrolysis on Tin Foil by Electrochemical Impedance Spectroscopy, *ACS Sustainable Chemistry & Engineering*, 2020, **8**, 5192-5199.

30. J. H. Montoya, C. Shi, K. Chan and J. K. Nørskov, Theoretical insights into a CO dimerization mechanism in CO_2 electroreduction, *Journal of Physical Chemistry Letters*, 2015, **6**, 2032-2037.

31. X. Liu, P. Schlexer, J. Xiao, Y. Ji, L. Wang, R. B. Sandberg, M. Tang, K. S. Brown, H. Peng, S. Ringe, C. Hahn, T. F. Jaramillo, J. K. Nørskov and K. Chan, pH effects on the electrochemical reduction of CO_2 towards C_2 products on stepped copper, *Nat. Commun.*, 2019, **10**, 32.

Chapter 5 Ethylene Production in Neutral Electrolyte on Pd-doped Cu

5.1 Introduction

Alkaline electrolyte is believed to be essential for efficient CO_2-to-C_{2+} conversion in ECR[1, 2]. The trade-off lies in the significantly limited theoretical conversion of CO_2 that becomes a barrier when upscaling for practical applications. Concentrated OH^- ions will react with CO_2 directly and form (bi)carbonate ions in the electrolyser, which could diffuse to anode chamber via AEM (crossover) before being turned back into CO_2 and released into air. It has been estimated that the highest single conversion rate of ECR to ethylene in alkaline electrolyte is less than 50% even at 100% selectivity[3]. Moreover, the alkaline solution causes carbonate precipitation that could block the flow tunnel leading to an undersupply of CO_2 reactant[4].

To circumvent the system loss of CO_2, a straightforward strategy is to replace the alkaline catholyte with a neutral solution. The carbonate formation might still exist but only exhibits influence after a long-term measurement due to the equilibrium of CO_2/HCO_3^-. Most importantly, CO_2 loss caused by electrolyte absorption could be prevented as much as possible. The downside of neutral environment for ECR is the promotion of competing reaction HER due to a higher proton concentration in the bulk electrolyte.

To avoid sacrificing the efficiency of ethylene production, an appropriate catalyst should be developed to fit the scene. We focused on the surface properties, *i.e.*, the adsorption of *CO, to tune the catalysts for neutral ECR with higher C_2 efficiency. Being the key intermediate of ECR, *CO coverage has been proved both theoretically and experimentally that it plays the crucial role in C-C coupling (**Fig. 1.4**)[2, 5, 6]. A moderate *CO coverage with the matching rate of protonation steps is the optimal way for multi-carbon production. For transition metals like Ag[7, 8] and Au[9-12], carbon monoxide is the

main products in ECR as the *CO bonding strength on their surface are limited. On the contrary, Ni[13-15], Pt[16, 17] and Pd[18, 19] tend to be poisoned by CO, among which Pt is the worst ECR catalyst as its surface sites will be quickly blocked by *CO and its HER active sites usually exhibit ultrahigh turnover frequency. It is unrealistic to switch from copper catalysts to other transition metals for hydrocarbon production.

There were strategies applied such as shaping and controlling morphologies of Cu oxides to preserve the $Cu^{\delta+}$ active site[20]. Yet these modifications on the oxide states of Cu were vulnerable to the negative potentials in the long run[21, 22]. Dopants/alloy was, therefore, considered to engineer the Cu surface. While researchers have studies alloys such as CuNi[23, 24], CuSn[25], CuAg[26] and CuAu[27, 28] in alkaline catholyte, it was discovered that their selectivities towards C_{2+} were not as good as pure copper counterparts. Pd became our choice based on the report that a CuPd electrocatalyst showed self-cleaning of carbonaceous species during ECR[29]. Recent work on CO electroreduction also demonstrated the ordered CuPd particles showing high acetate selectivity[30]. These studies revealed that the introduction of Pd to Cu enhanced surface affinity of *CO to an appropriate level beneficial to C-C coupling.

Herein, in this chapter, CuPd catalysts were selected for ECR in neutral electrolyte to explore the reaction under milder conditions. The foreign Pd atoms effectively altered the Cu particle performance to an ethylene favoured state. *In-situ* characterisations including EIS and PTR-TOF-MS were applied to understand the real-time behaviours on the surface of electrode. Carbon-related process was proved to be faster than protonation steps, which provided evidence that Pd induced higher carbon intermediates coverage could promote C-C coupling. XAS was measured to analyse the coordination environment of Cu and Pd sites and capture the local changes on the Cu sites.

From this project, high efficiency of CO_2-to-C_2H_4 was achieved under neutral conditions. The underlying mechanism was proposed that high *CO affinity by controlling Pd-doping level could tune the performance of catalysts to reach an efficiency of hydrocarbons comparable to the traditional alkaline conditions.

5.2 Results and Discussion

Synthesis methods and notations of the materials involved in this chapter can be found in previous section 2.3.7. Ex-situ measurements were described in sections 2.3.11, 2.3.13 and 2.3.14. *In-situ* measurements were described in sections 2.3.16 and 2.3.17.

5.2.1 CuPd Catalysts Properties

To understand the Pd-doped Cu materials, *ex-situ* characterisations were first applied including XRD, TEM and XPS. Measurements were mostly performed with catalysts prepared on the GDE to exclude any influence caused by electrode fabrication. While the *ex-situ* characterisation could not fully explain the behaviour of CuPd catalysts under electrochemical conditions, a primary understanding to their initial structures and morphologies is essential for further *in situ* experiments.

5.2.1.1 TEM

TEM images (**Fig. 5.1a**) of CuPd2 sample shows that the round particles have a size of 16-18 nm in diameter, close to the Cu particles synthesized in Chapter 4. The doping of Pd at around 2 wt.% has little effect on the size of the particles The lattice fringe could be seen in HRTEM images (**Fig. 5.1b**), where each particle has different orientations of lattice. Like the Cu particles introduced in Chapter 4, the Pd doping also created the defective surface of CuPd2 particles. The overall morphology of CuPd2 resembled the

undoped Cu particles. EDX mapping of Cu and Pd confirms the existence of Pd and indicates that no significant aggregation of Pd within the particles.

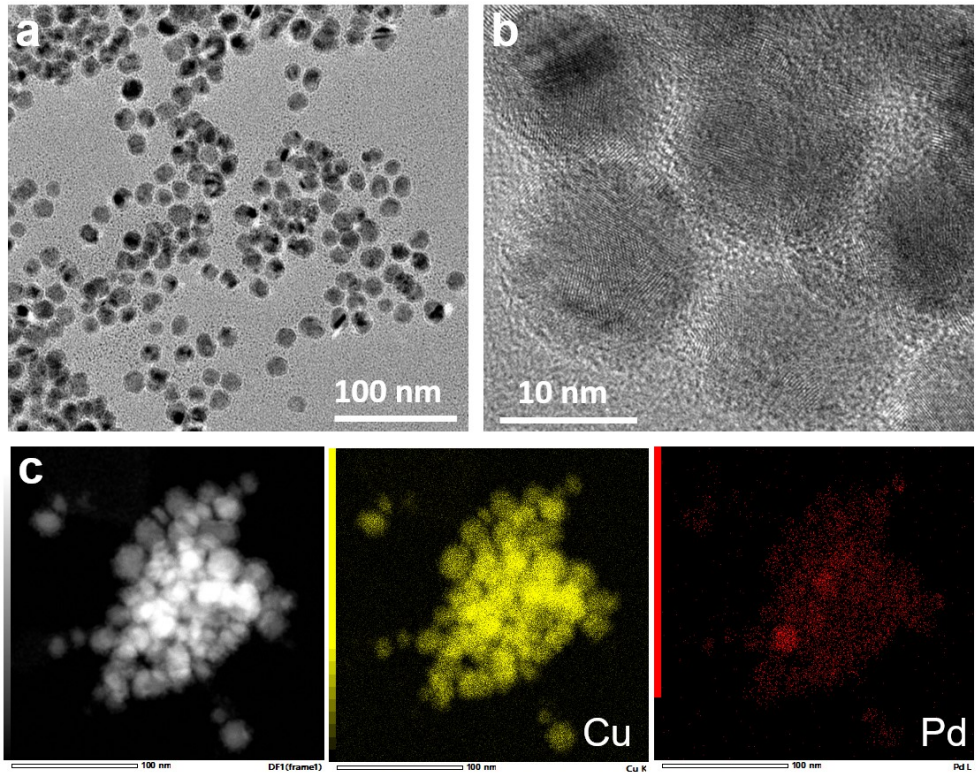


Figure 5.1 (a) TEM image of CuPd2 particles; **(b)** HRTEM image of CuPd2 particles; **(c)** EDX mapping of Cu (yellow) and Pd (red) of CuPd2 particles.

5.2.1.2 XRD

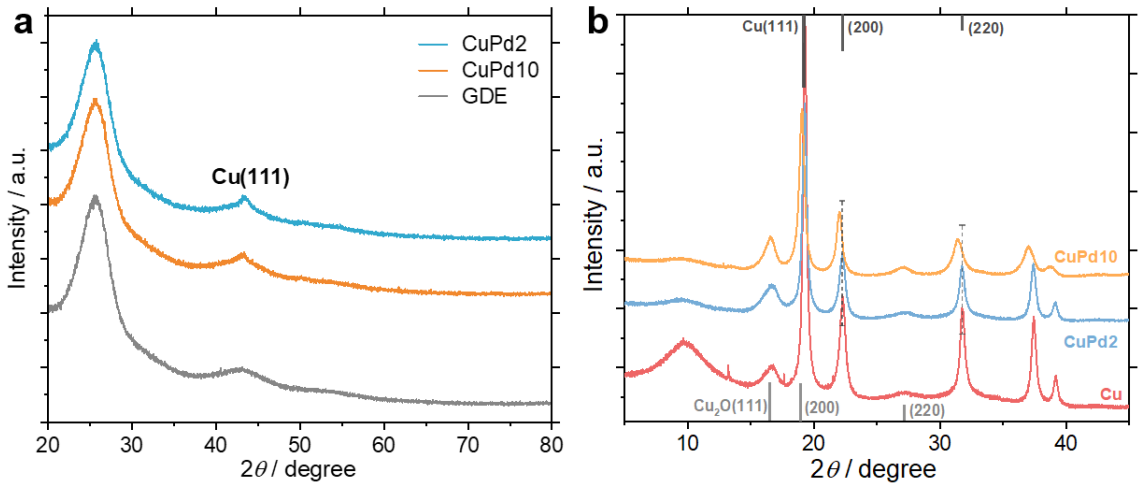


Figure 5.2 (a) XRD patterns of CuPd catalysts on GDE and bare GDE substrate. **(b)** synchrotron XRD (λ=0.7003 Å) patterns of undoped and doped Cu catalysts.

Comparing the XRD patterns in **Fig. 5.2a**, Cu (111) facet is the only visible peak in both CuPd2 and CuPd10 samples. Due to the limited thickness of catalysts layer (below 1 μm), the size of the grain in the particles and the capacity of the XRD instrument, the signal resolution and intensity was not high enough to distinguish other Cu species. Synchrotron XRD were then measured for better resolution to distinguish the components in the particles. Both Cu and Cu_2O phase are detected in the doped and undoped particles (**Fig. 5.2b**). As the Pd amount increasing, peaks assigned to Cu facets shows broadening and shifting to lower 2θ while the Cu_2O facets remained similar. The dopant Pd with a larger atomic radius brought disorder to the original Cu lattice and increased *d* spacing induced by compressive strain[31].

5.2.1.3 XPS

As metallic copper tends to be oxidised after air exposure, Cu 2p XPS spectra were measured with samples on Si wafer (**Fig. 5.3a, c**) and GDE (**Fig. 5.3b, d**) to capture this change. The binding energy of Cu $2p_{3/2}$ peak in both samples slightly shifted towards higher binding energy after sprayed onto GDE indicating the oxidation of Cu. The peaks at around 934 eV (light blue area) that belong to Cu(II) species show increments in the ratio of total peak area, representing the continuous formation of Cu(II) during the electrode fabrication. This is also proved by the intensified satellite peaks between 940-945 eV on samples with GDE substrates compared to ones with Si wafer.

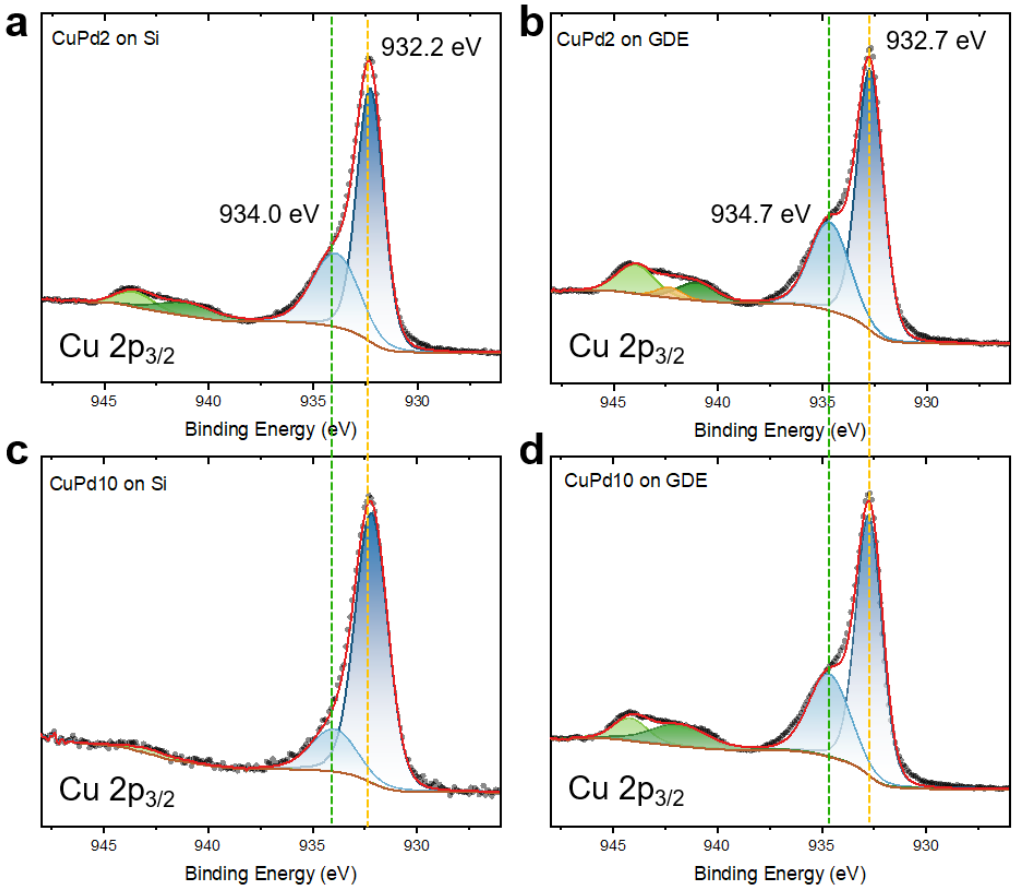


Figure 5.3 High-resolution XPS spectra of Cu $2p_{3/2}$ CuPd2 on **(a)** Si wafer and **(b)** GDE; CuPd10 on **(c)** Si wafer and **(d)** GDE. Green dash lines stand for Cu(II) species; yellow dash lines stand for Cu(0)/Cu(I) species.

Pd was also studied by XPS as plotted in **Fig. 5.4**. By calculating the peak intensity of Cu $2p_{3/2}$ and Pd $3d_{5/2}$ corrected with relative sensitivity factor (RSF), the atomic percentage of Pd in the surface layers was obtained. The percentage of Pd in CuPd2 sample was around 1.6% in accordance with the amount of Pd precursors, while in CuPd10 sample, the Pd percentage was around 6.7%, slightly lower than the theoretical content. In the Pd XPS, a shift of Pd 3d peaks from 335.4 to 335.8 eV was detected in CuPd2 sample after the particles were loaded onto the GDE (**Fig. 5.4a, b**). In contrast, the peaks remained at the same position in CuPd10 sample. As the higher binding energy usually indicated a higher oxidation state, in this case, the shift could be resulted from the incorporation of oxygen atoms to the particles during electrode preparation. It is likely that CuPd2 was more

vulnerable to oxygen in the air according to the satellite peaks in **Fig. 5.3 a, b**, which led to the Pd 3d peaks shifting. Whereas for CuPd10, the sample was less influenced by oxygen that maintained the Pd valence state. The underlying reason for the different behaviours requires further understanding of the CuPd structures and interactions between the atoms. XAS was used to explain this and will be introduced in section 5.2.4.

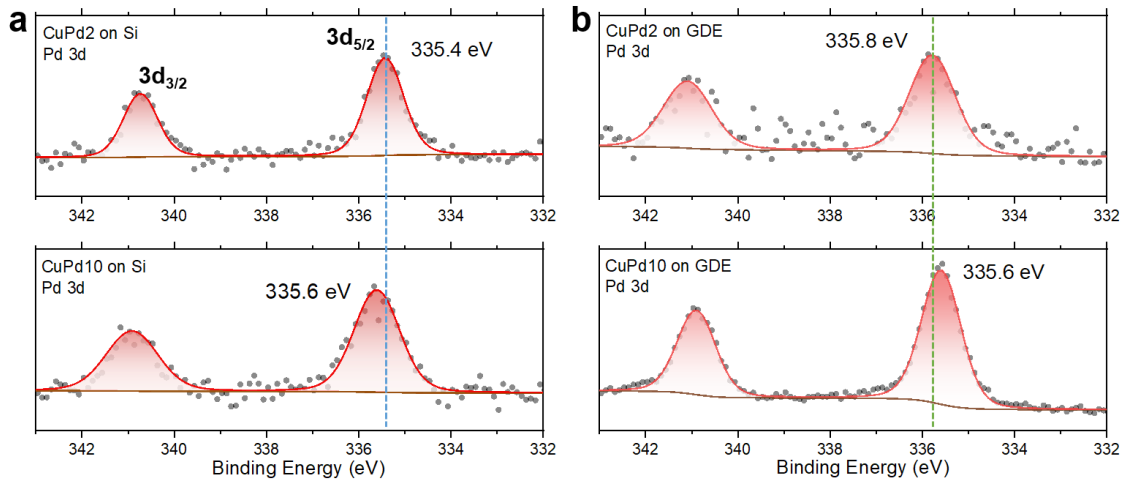


Figure 5.4 High-resolution XPS spectra of Pd 3d from CuPd2 and CuPd10 loaded **(a)** on Si wafer and **(b)** on GDE.

5.2.2 Electrochemical Performance

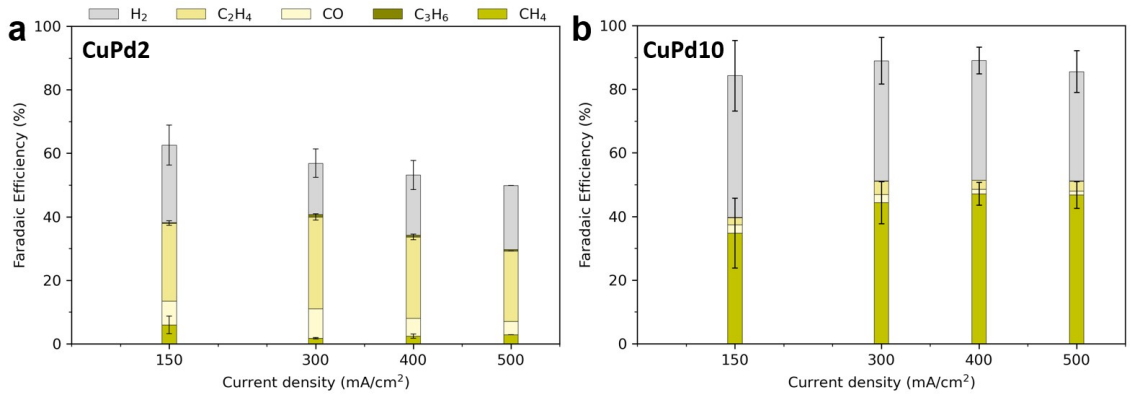


Figure. 5.5 Products distribution of ECR on **(a)** CuPd2 and **(b)** CuPd10 particles in 0.5M K_2SO_4.

Electrochemical performance of the samples was evaluated in 0.5 M K_2SO_4 at different current densities in a two-gap flow cell. For the CuPd2 sample, ethylene is the main

product in gas phase with over 30% FE at 300 $mA \cdot cm^{-2}$ (**Fig. 5.5a**). C_3 product, propene, was also detected by the GC though the selectivity was below 5%. The decreasing of total FE as current density rising indicates the accumulation of liquid phase products including ethanol and acetic. For the CuPd10 sample, the selectivity to ethylene is greatly suppressed and methane dominates the carbon products (**Fig. 5.5b**). Such distribution indicates that the C-C coupling is not taking place on the surface of CuPd10 as much as CuPd2. Methane and hydrogen take up over 85% of the total products and liquid products such as formic acid and ethanol could hardly be detected.

5.2.3 EIS Studies

EIS potential scan was measured and is shown in Nyquist (**Fig. 5.6a, c**) and Bode plot (**Fig. 5.6b, d**). Like the pure Cu in KOH introduced in Chapter 4, the high frequency step dominates when the potential is more negative (**Fig. 5.6b**) with sample CuPd2. However, the slow step which accounts for the methane selectivity as explained previously is also visible in the impedance spectra of CuPd2, consistent with the production of methane at a higher efficiency compared to Cu in KOH condition as shown in **Fig 4.8**.

CuPd10 has a different behaviour (**Fig. 5.6c**) from CuPd2 as shown in the Nyquist plot. Another depressed semicircle appears at the lower frequency region which indicates a new charge transfer step. This also causes a larger total resistance of overall charge transfer process reflected by the intersection point with the Z_{Re} axis at a higher value. The Bode plot shows a more distinct phase change at low frequency than the CuPd2 (**Fig. 5.6d**), implying the enhancement of proton transferring steps. Correspondingly, the relative high frequency step that representing for the carbon-intermediate related process is supressed, in agreement with the low efficiency of ethylene production.

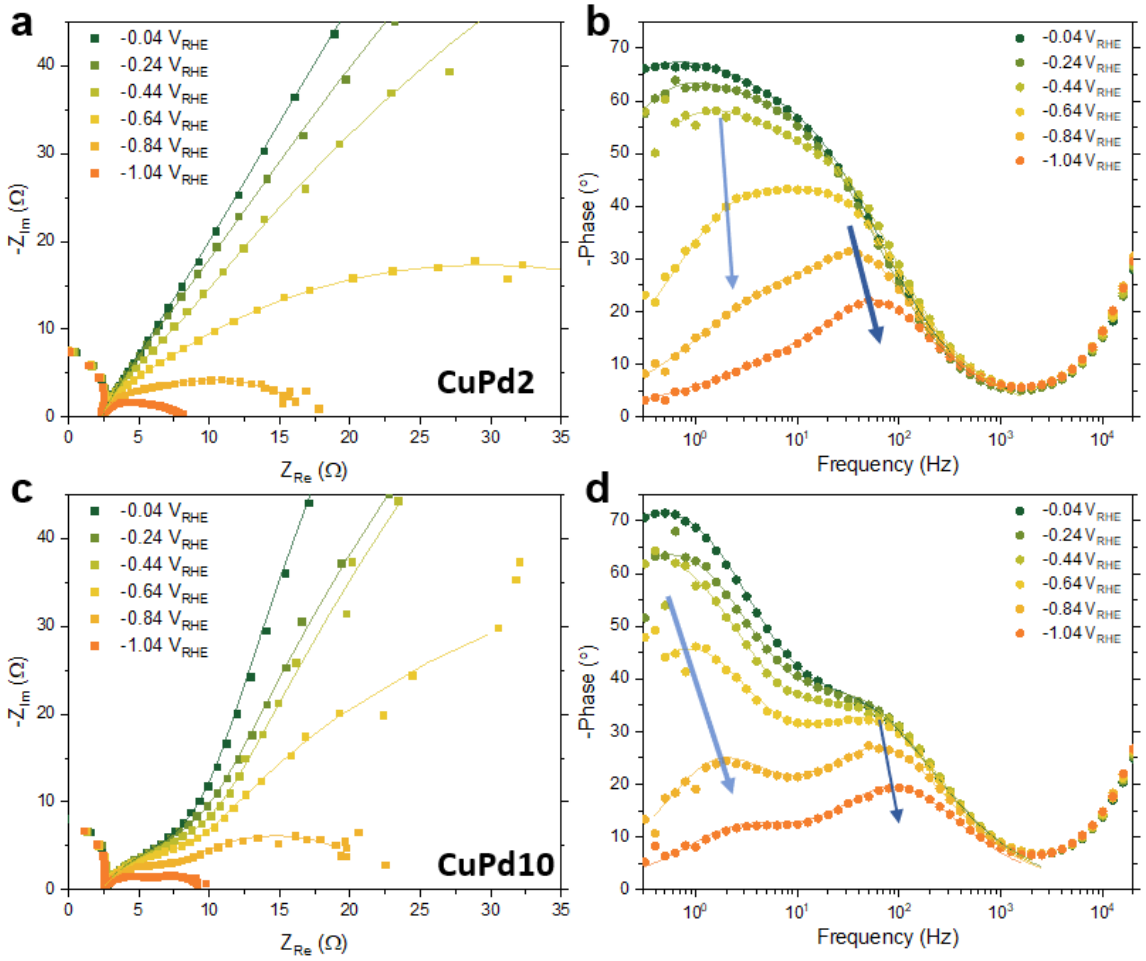


Figure 5.6 (a) Nyquist plot and **(b)** Bode plot in phase angle of EIS spectra on CuPd2 NPs; **(c)** Nyquist plot and **(d)** Bode plot of EIS spectra on CuPd10 NPs. Spectra were measured in 0.5M K_2SO_4 under applied potentials on cathode. Bode plot in total impedance can be found in **Fig. A5.**

Circuit fitting of EIS was carried out to gain insight into the kinetics on the electrode. An equivalent circuit model consisting of two R||CPE components was used to fit the spectra (**Fig. 5.7a**, inset). The CPE in parallel with a resistor (R||CPE) represents a charge transfer step and the resistor connected in series stands for the solution/electrolyte resistance (Rs). The capacitance of CPE1 slightly decreased from 10^{-2} to 10^{-3} F as the applied potentials became more negative in sample CuPd2 and this decreasing trend was absent in CuPd10. The CPE2 also exhibits different behaviours in terms of the effective capacitance. It fluctuates at around 1.5×10^{-3} F across the potential range tested in sample

CuPd2 (**Fig. 5.7a**). In contrast, the CuPd10 showed an increasing capacitance of CPE2 up to 10^{-2} F at around -1 V (**Fig. 5.7b**). As the capacitance of the double layer on the electrode-electrolyte interface could represent the adsorption of ions/intermediates, the high capacitance of CPE2 can be attributed to *CO-related species adsorption on the electrode surface caused by high Pd doping level. It may have caused CO poisoning on the electrode surface where *CO intermediates blocked most ECR active sites. The increment of capacitance is not apparent on CuPd2 sample due to the matching rate of *CO formation and the followed protonation/coupling steps. Therefore, a matching rate between the proton activation and *CO formation should be achieved to allow the production of ethylene at a higher efficiency for the less Pd-doped sample.

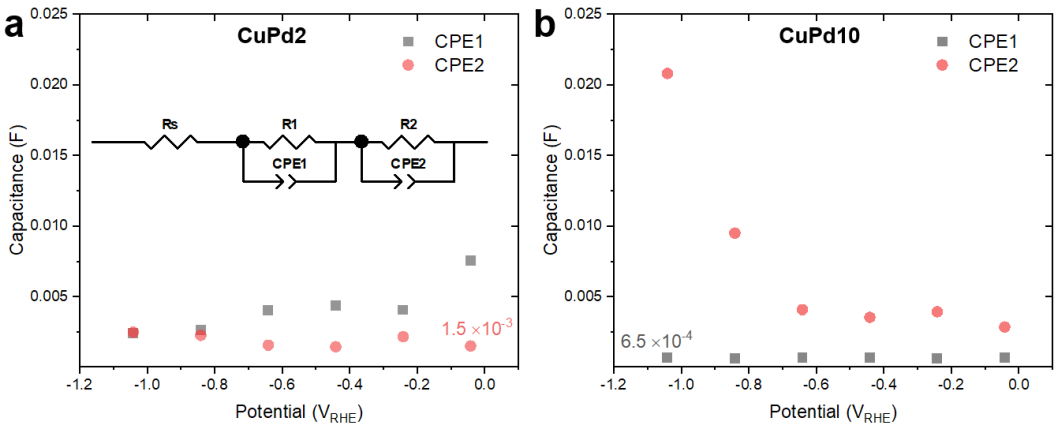


Figure 5.7 Capacitance value extracted from circuit fitting of CPE and their correlation with potentials from samples **(a)** CuPd2 and **(b)** CuPd10. The circuit used for fitting is shown as an inset in plot.

Resistance values of both samples shared a similar trend with R1 tending to be relatively small and constant while R2 decreasing across the measured 0 to -1V potential range (**Fig 5.8**). This indicates that the R1||CPE1 was related to a process insusceptible to the external electric field, likely the activation of hydrogen atoms from water molecules on the electrode surface with a smaller overpotential below 200mV compared to ECR[32]. The R2||CPE2 represents the polarization step which could be the activation of CO_2 and the

followed *CO formation as both require a higher applied potential to drive. Combining the results from both the capacitance and resistance aspects, it is concluded that R1||CPE1 unit is related to the surface adsorbed *H generated from proton activation and then consumed by protonation of carbon species as explained by the decreasing capacitance value and the constant resistance, whereas R2||CPE2 involves the carbon-related steps including the protonation of carbon intermediates and C-C coupling steps.

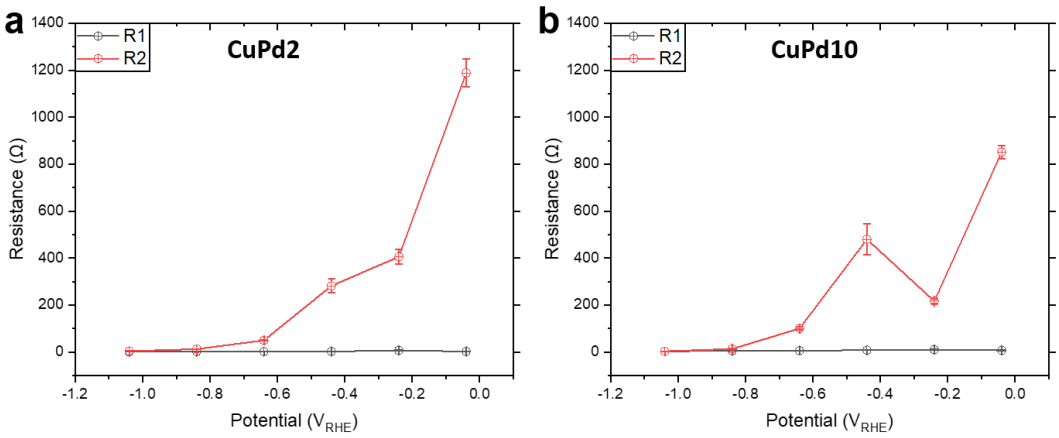


Figure 5.8 Resistance value extracted from circuit fitting of CPE and their correlation with potentials from samples **(a)** CuPd2 and **(b)** CuPd10.

5.2.4 XAS

5.2.4.1 *Ex-situ* XAS on GDE

The XANES spectra were collected to understand the state of Cu and Pd in the particles loaded on GDE substrate. The Cu K-edge of CuPd2 and CuPd10 samples (**Fig. 5.9a**, red and blue curves, respectively) have a peak at the rising absorption edge at around 8981 eV close to the Cu and Cu_2O standard (cyan dashed line), which is attributed to the $1s \rightarrow 4p$ transition in Cu(0) and the $1s \rightarrow 4p_{xy}$ transition in Cu(I). The existence of both Cu(0) and Cu(I) is also confirmed by the $1s \rightarrow 4p_z$ transition in Cu(I) at around 8995 eV (orange dashed line) and the following white line peak from Cu(0) at around 9002 eV (yellow dashed line) in the spectra of CuPd2 and CuPd10.

The Pd K-edge of CuPd particle samples shows a completely different pattern from the Pd foil standard (**Fig. 5.9b**), which indicates the absence of Pd metallic phase within the bulk of particles. The edge position of the Pd K-edge spectra (red and blue curves) is slightly higher than the Pd(0) standard (grey curve) suggesting a higher oxidation state of Pd in both CuPd particles. Further analysis on the EXAFS data provided information on the coordination environment of Pd atoms with the surrounding Cu atoms.

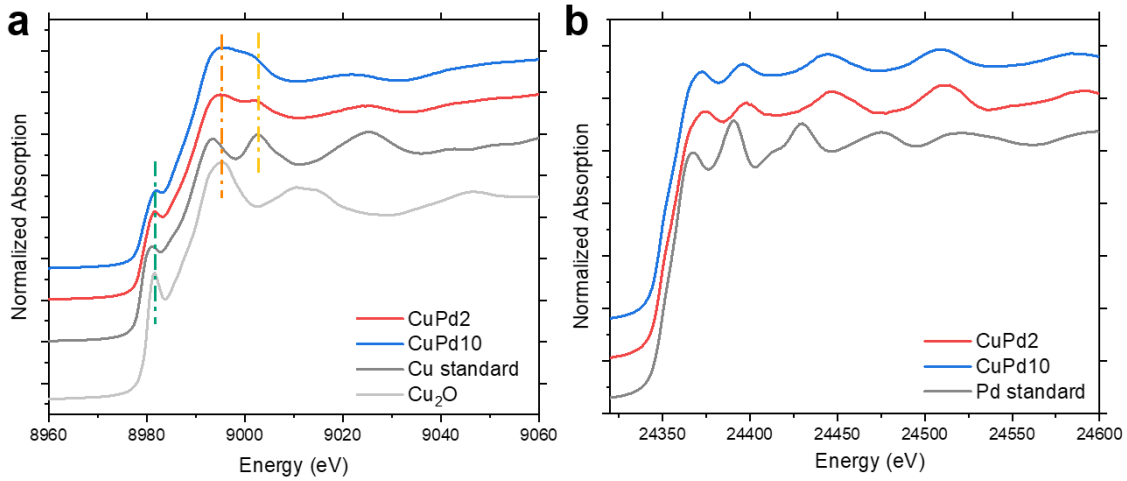


Figure 5.9 (a) Cu K-edge and **(b)** Pd K-edge XANES of CuPd2 and CuPd10 with standards.

Table 5.1 Fitting Parameters of Cu K-edge EXAFS data for CuPd2 and CuPd10 on GDE

Sample	Scattering Path	R (Å)	CN	σ^2 (Å^2)
CuPd2	Cu-O	1.85(2)	0.7(1)	0.008(1)
	Cu-Cu	2.54(2)	6.1(5)	0.008(1)
CuPd10	Cu-O	1.89(5)	2.2(4)	0.010(2)
	Cu-Cu	2.58(5)	4.7(9)	0.010(2)
	Cu-Pd	2.63(5)	0.5(4)	0.002(1)

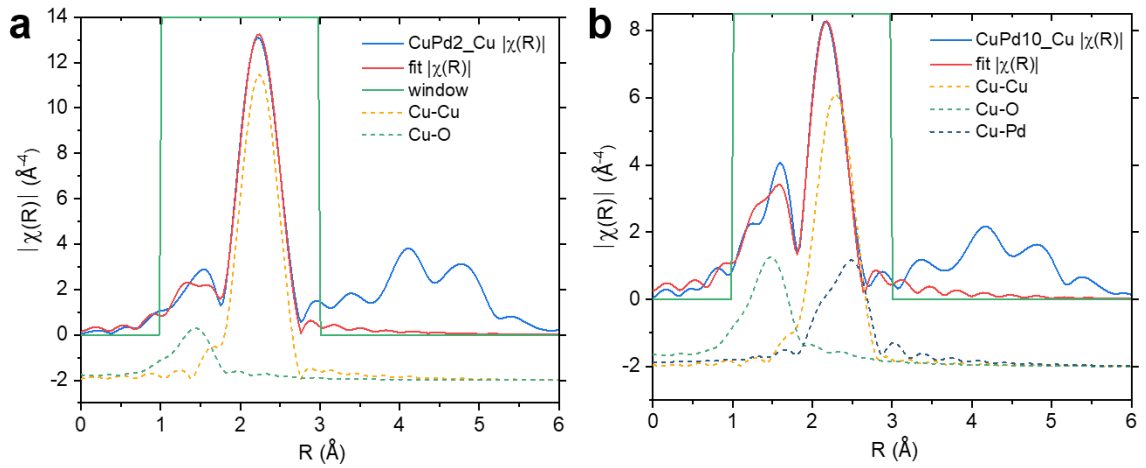


Figure 5.10 R space k^3 Cu K-edge Fourier-transformed EXAFS data (blue curve) and first shell fitting results (red curve) of **(a)** CuPd2 and **(b)** CuPd10.

Structural information was extracted from the EXAFS by first shell fitting. To fit the shell, a Cu(111) slab model containing 64 atoms was built with one Pd substituted the surface Cu (**Fig. A6**). The fitting results are shown in **Table 5.1**. Distance of Cu-O and Cu-Cu scattering in both samples is similar, yet the coordination numbers (CN) vary. CuPd2 has a Cu-Cu CN up to 6 and the Cu-O less than 1 (each component's contribution plotted in **Fig 5.10a**, dashed lines). Comparing with the CuPd10 sample which is higher in Cu-O C. N. and lower in Cu-Cu, CuPd2 preserves Cu atoms in more closely packed structures with less distortion. Nevertheless, a Cu atom on the perfect Cu(111) surface should have a CN of 9. A CN lower than 9 indicates that the Pd-doped Cu particles in this study have a defective surface. The high level of Pd dopants further create more defects via inducing the lattice expansion reflected by the CN below 5. The observation of the particles with stacked facet and polycrystallinity from TEM images agrees with the unsaturated coordination fitting results (**Fig. 4.4**, **Fig. 5.1**).

Contribution from Cu-Pd in R space is deconvoluted from the CuPd10 sample (**Fig 5.10b**, navy dashed lines) apart from the Cu-Cu and Cu-O pathways. The CN of Cu-Pd is, however, below 1, implies a random distribution of individual Pd atom in the particles. A

further investigation on the Pd K-edge was carried out to explain the structural environment of Pd atoms better. A Pd-Cu scattering path from the Pd-substituted Cu(111) model fits well with both EXAFS data for sample CuPd2 and CuPd10 (**Fig. 5.11**). The coordination environment of Pd, however, differs from each other. CuPd2 shows a saturated Pd coordination with CN up to 12 implying that Pd atoms are restricted within the particles, whereas CuPd10 has unsaturated Pd sites likely to appear on the surface (**Table 5.2**). A CN of 8-9 is found in Pd atoms in CuPd10. The increased Pd dopant amount promotes the diffusion of Pd atoms to the surface of nanoparticles.

Table 5.2 Fitting Parameters of Pd K-edge EXAFS data for CuPd2 and CuPd10 on GDE

Sample	**Scattering Path**	**R (Å)**	**CN**	**σ^2 (Å^2)**
CuPd2	Pd-Cu	2.59(1)	12.0(4)	0.006(1)
CuPd10	Pd-Cu	2.58(1)	8.5(9)	0.005(1)

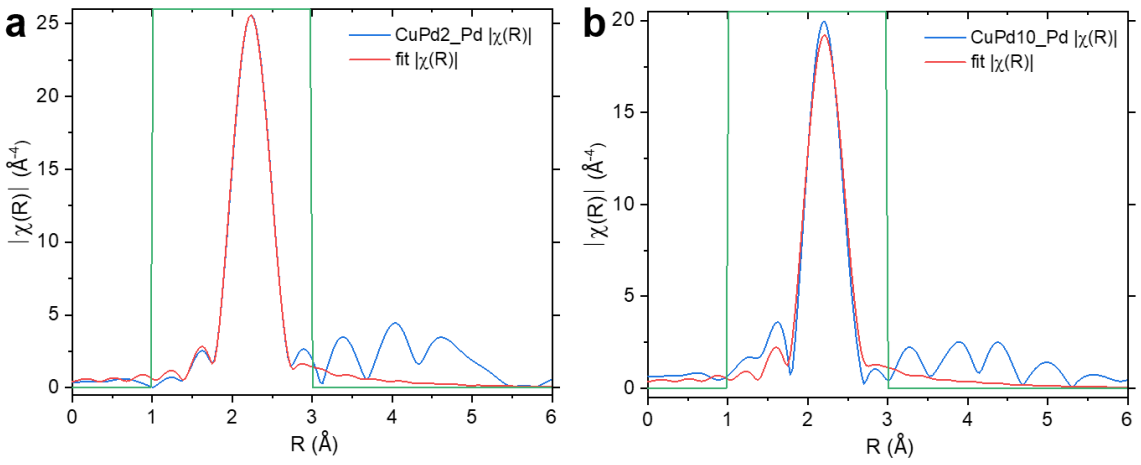


Figure 5.11 R space k^3 Pd K-edge Fourier-transformed EXAFS data (blue curve) and first shell fitting results (red curve) of **(a)** CuPd2 and **(b)** CuPd10. Fitting window is plotted in green from 1-3 Å.

5.2.4.2 *In-situ* XAS in Neutral Electrolyte

In-situ XAS of Cu K-edge were measured in static electrolyte at different current densities. Undoped Cu particles were first tested in 0.5M K_2SO_4 to understand the pure Cu behaviours. The peaks at the adsorption edge at near 8980 eV originated from the 1s→ 4p transition could be attributed to the co-existence of Cu(0) and Cu(I) (**Fig. 5.12a**). The white lines shape at *ca.*8995 and 9002 eV matches with both Cu_2O and Cu standards indicating the existence of both phases with the metal component dominating the bulk of particles. The 1st derivative spectra imply the disappearance of Cu_2O phase under 10mA condition (**Fig. 5.12b**, blue curve) with the narrowed peak close to 8980 eV representing the formation of a pure Cu(0) state.

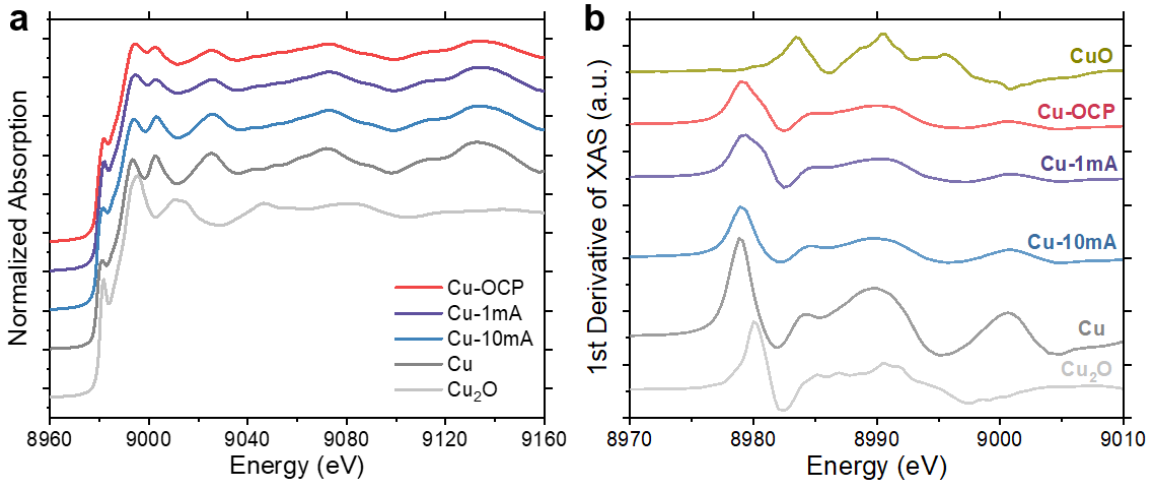


Figure 5.12 (a) Cu K-edge XANES of Cu-S1 particles in 0.5M K_2SO_4 electrolyte as a function of current density with standards. **(b)** 1st derivative of Cu K-edge XANES of Cu-S1 with standards.

Based on the undoped-Cu results, the effects of Pd doping could be analysed. The contribution from Cu(I) species becomes stronger after Pd doping as shown by the higher peak at 8995 eV under open circuit conditions (**Fig. 5.13a**, **c**, red curve) compared to the pure Cu sample (**Fig. 5.12a**, red curve). From the derived XANES, a narrower peak at 8978.9 eV for samples measured at 1mA·cm^{-2} (purple curves) could be found in contrast with the broad peak for Cu particles (**Fig. 5.12b**), which results from the shift of spectra towards a lower energy region consistent with the electroreduction process. The reduction

current exerted significant influence on both CuPd2 and CuPd10, as the component of Cu(I) was promptly removed even at a current density as low as 1 mA·cm^{-2}. No further changes were observed under 10 mA·cm^{-2}.

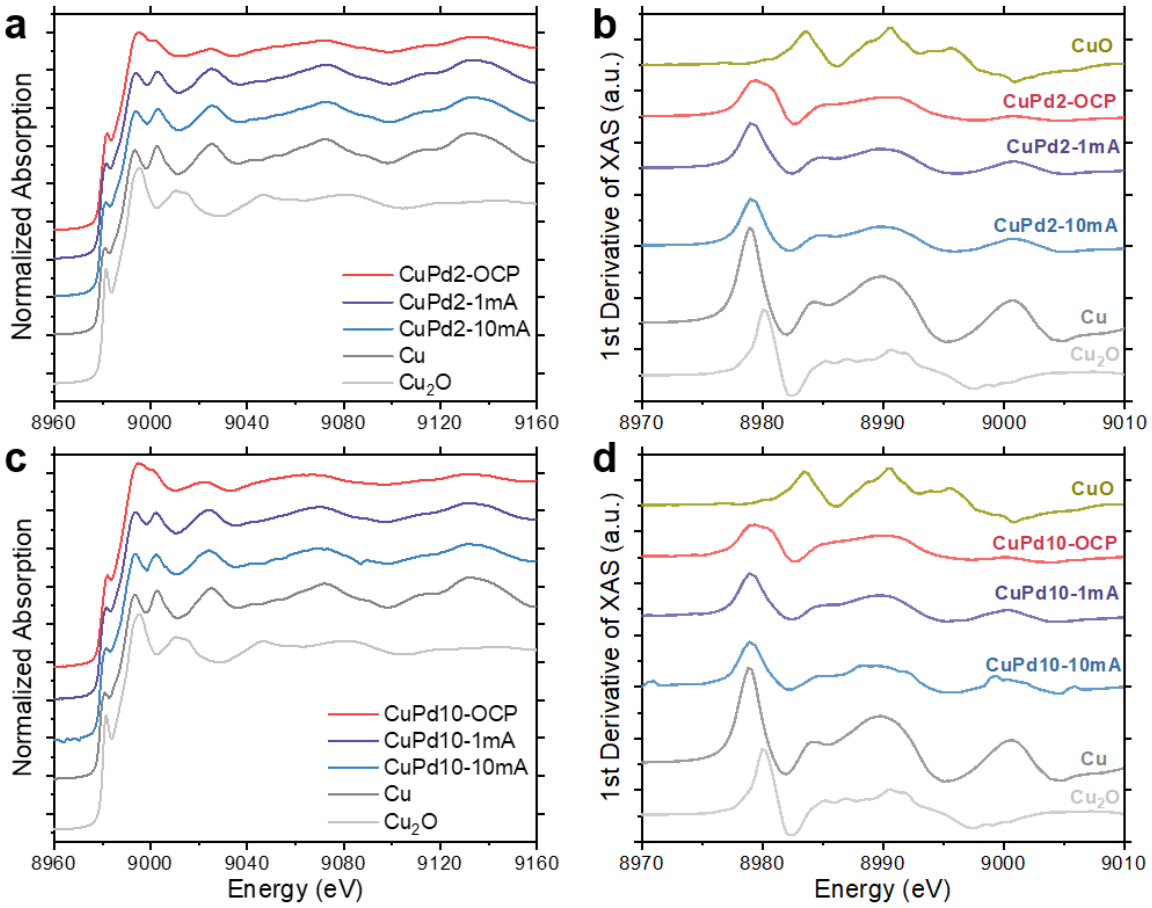


Figure 5.13 (a) Cu K-edge XANES of CuPd2 particles in 0.5M K_2SO_4 electrolyte as a function of current density with standards. **(b)** 1st derivative of Cu K-edge XANES of CuPd2 with standards. **(c)** Cu K-edge XANES of CuPd10 particles in 0.5M K_2SO_4 electrolyte as a function of current density with standards. **(d)** 1st derivative of Cu K-edge XANES of CuPd10 with standards.

Table 5.3 Fitting Parameters of Cu K-edge EXAFS data for CuPd2 in neutral electrolyte

Sample	Scattering Path	R (Å)	CN	σ^2 (Å^2)
CuPd2-ocp	Cu-O	1.86(2)	1.1(3)	0.005(4)
	Cu-Cu	2.54(2)	5.2(7)	0.009(1)

CuPd2-1mA	Cu-Cu	2.54(1)	9.9(5)	0.008(1)
CuPd2-10mA	Cu-Cu	2.54(1)	10.1(3)	0.009(1)

Table 5.4 Fitting Parameters of Cu K-edge EXAFS data for CuPd10 in neutral electrolyte

Sample	**Scattering Path**	**R (Å)**	**CN**	**σ^2 (Å^2)**
CuPd10-ocp	Cu-O	1.87(3)	1.6(4)	0.010(2)
	Cu-Cu	2.55(3)	4.4(8)	0.010(2)
	Cu-Pd	2.61(3)	0.9(6)	0.010(2)
CuPd10-1mA	Cu-O	1.85(1)	0.2(2)	0.009(1)
	Cu-Cu	2.53(1)	8.3(6)	0.009(1)
	Cu-Pd	2.59(1)	0.4(5)	0.009(1)
CuPd10-10mA	Cu-O	1.85(1)	0.0(2)	0.009(1)
	Cu-Cu	2.53(1)	8.6(6)	0.009(1)
	Cu-Pd	2.59(1)	0.4(6)	0.009(1)

The first-shell fitting parameters are listed out in **Table 5.3** and **Table 5.4**, and the contributions of each scattering path are plotted in **Fig. 5.14**. The Cu-O scattering could not be fitted into any reducing CuPd2 samples confirming a complete depletion of oxygen from the catalyst at an early stage of reduction (**Table 5.3**). The CN of Cu-Cu increases from around 5 to 10 as the reduction progressing. The number is larger than the *ex-situ* results from CuPd2 sample with a Cu-Cu CN of 6, which provides a clue of particle aggregation. No significant change of Cu-Cu bond distance can be extracted from the EXAFS data of CuPd2. For sample CuPd10, three scattering paths were used to accomplish the fitting, as the Cu-Pd could hardly be ignored with a higher Pd amount. A decreasing in CN of Cu-O from 2 to almost 0 can be found marking the complete removal of oxygen as the reduction current increasing. The rate of this process is, however, much

slower than the CuPd2 sample. The latter one showed trivial Cu-O contribution as soon as a reductive current was deployed. Correspondingly, the Cu-Cu distance decreased, and the CN increased during to the oxygen depletion. The CN of Cu-Cu in the CuPd10 sample does not leap to 10 but stabilizes at around 8 which is likely due to the doping of Pd that creates a disordered structure with more unsaturated Cu sites. The Cu-Pd scattering path has a CN less than one across the measured current window suggesting a well-dispersed Pd in the CuPd10 particles.

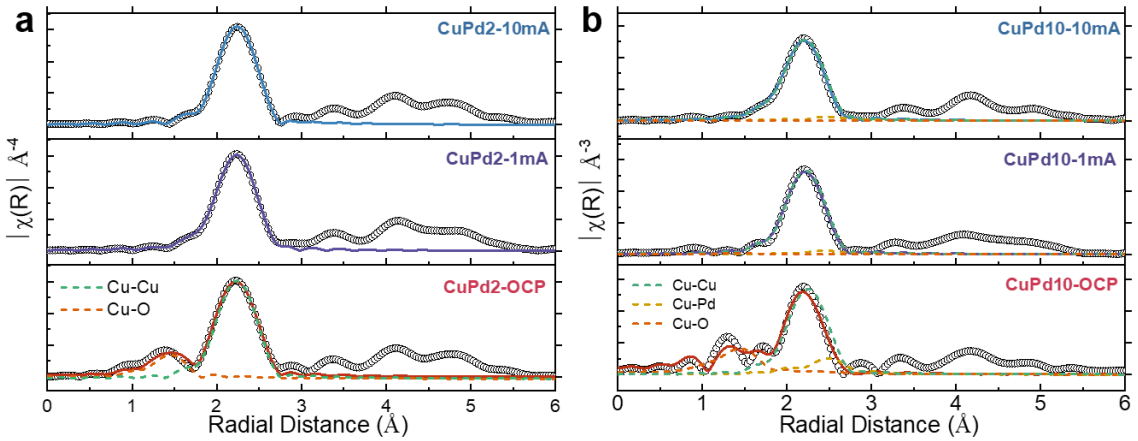


Figure 5.14 (a) R space k^3 Pd K-edge Fourier-transformed EXAFS data (scatter) and first shell fitting results (solid curve) of CuPd2; and **(b)** R space k^2 Pd K-edge Fourier-transformed EXAFS data (scatter) and first shell fitting results (solid curve) of CuPd10. Fitting window is from 1-3 Å.

5.2.5 Operando PTR-TOF-MS

It is important to study the mechanism of C_1 products in neutral electrolyte as the efficiency of CO_2-to-C_{2+} can be significantly affected when C_1 production dominates the ECR. While CO and methane cannot be directly detected by PTR-MS, formaldehydes and methanol can be monitored to understand the C_1 mechanism[33]. The formation of C_1 products except formic acid in ECR requires deoxygenation from the CO_2 molecules followed by steps of protonation as introduced previously (**Fig. 1.3**). For formaldehydes (HCHO), *CO intermediates are firstly protonated with the carbon atoms bonding to

hydrogens (*CHO). In contrast, the methanol (CH_3OH) formation undergoes one protonation step on oxygen atoms (*COH). With the assumption that each protonation step to a carbon atom has a similar reaction rate under the same H^+ concentration, the HCHO and CH_3OH molecules were used to semi-quantitatively represent the formation of *CHO and *COH intermediates, respectively. A linear scan of current was applied to study the products distribution trends under increasing current density (**Fig. A7**).

Starting from the undoped Cu particles in K_2SO_4 which has been investigated in Chapter 4 with a methane FE at 40% (**Fig. 4.6b**), a continuously increasing of HCHO signal is captured by MS and did not reach saturation at 100 $mA \cdot cm^{-2}$ (**Fig. 5.15,** blue curve). The increment of signal intensity from CH_3OH is an order of magnitude smaller than that of HCHO (**Fig. 5.15,** orange curve). Therefore, it is anticipated that the formation of *CHO is at a higher rate compared to *COH and likely to achieve a higher surface coverage. As the Cu appeared to produce methane as the main carbon-related product and the liquid products were at limited efficiency (<20%), it is rational to conclude that the methane formation may follow the steps of which the protonation to carbon atoms is in prior to oxygen atoms in the case of the neutral condition.

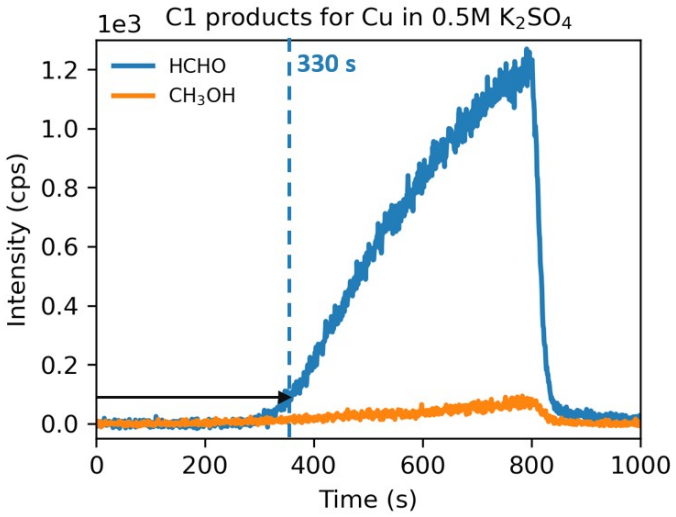


Figure 5.15 C_1 products measured from PTR–TOF–MS on pure Cu particles at a scan rate of 0.15 mA·s^{-1} from 0 to 100 mA. The scan started at 100 s and stopped at 770 s. A reference line for onset time in parallel with x-axis marks the intensity of 100 counts.

With Pd doping, the HCHO reached saturation under high current density condition (**Fig. 5.16**, blue curves). The onset point of HCHO was brought forward compared to the undoped Cu which had an onset of around 330 s. For CuPd2 sample, the appearance of HCHO was greatly forwarded to around 240 s (**Fig. 5.16a**, blue dashed line), which could be explained by the higher affinity to *CO after Pd-doping. After the saturation of HCHO, there was a decreasing trend marking the suppression of *CHO to HCHO process (600-800 s, with a corresponding current density ranging 75-100 mA·cm^{-2}). This phenomenon agrees with the high C_{2+} selectivity for CuPd2 that *CHO intermediates participates in the C-C coupling steps at higher current density[2]. Interestingly, a surge of CH_3OH can be observed on CuPd10 at 330 s (**Fig. 5.16b**, orange curve) which, considering the high doping level of Pd, is caused by the *CO being stabilized for a longer period on the surface allowing a higher chance of multi-protonation steps beneficial to the formation of CH_3OH.

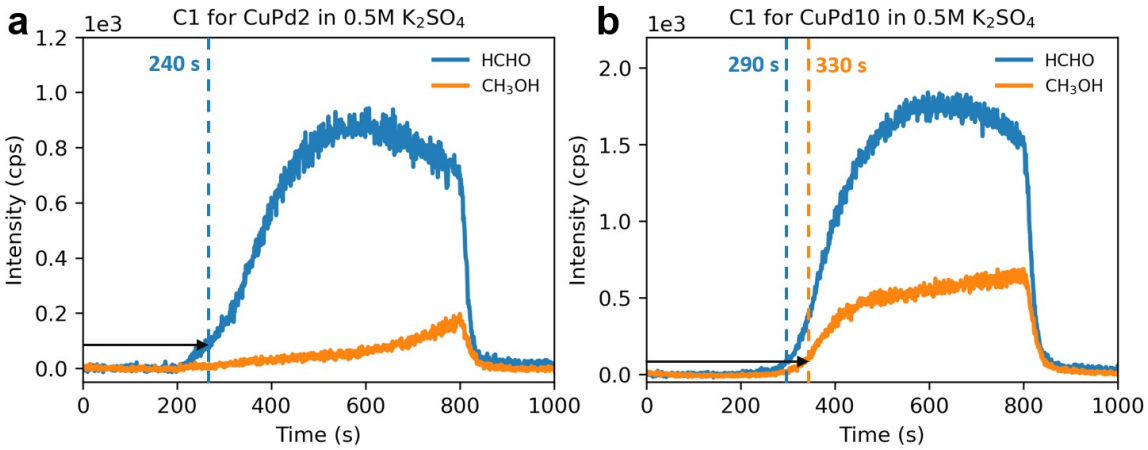


Figure 5.16 C_1 products measured from PTR–TOF–MS on **(a)** CuPd2 and **(b)** CuPd10 at a scan rate of 0.15 mA·s^{-1} from 0 to 100 mA. The scan started at 100 s and stopped at 770 s. A reference line in parallel with x-axis marks the intensity of 100 counts.

Multi-carbon products are produced following complicated pathways. The products discussed here are focused on C_2 and C_3 products. The counter-intuitive finding is that the C_{2+} molecules were detected no later than C_1 (**Fig. 5.17**, black arrow marked onset time) indicating that C-C coupling steps are not the rate-determine step (RDS) of ECR in neutral electrolyte at the beginning of the reactions[34]. Instead, the protonation steps after the C-C coupling and before the final desorption from surface should be the RDS.

Among the C_{2+} products, the onset point does not differ greatly from each component, but they show varied patterns despite under the same current density. The CuPd2 started with an upsurge of CH_3CHO before C_3 prevailed and reached saturation (**Fig. 5.17a, b**). At high current density range (after 600 s, current density >75 $mA \cdot cm^{-2}$), the C_3 signals declined in intensity (brown and purple curve), while the C_2 signals continued to increase (green and red curve). The decreasing in C_3 and increasing in C_2 demonstrates that excessive C_1 intermediates cannot react with the C_2 intermediates to generate C_3 products and that the C_2 formation dictates the surface reaction. Such behaviours are not significant in CuPd10 (**Fig. 5.17c,d**). With the Pd exposed on the surface of particle at high doping level, C_1 intermediates are stabilised on certain Pd sites for longer time which allows higher chance for C_3 formation, as it can be reflected in the plot where the saturation point of propionaldehyde (CH_3CH_2CHO, **Fig. 5.17c**, brown curve) for CuPd10 is after 600 s, much later than that of CuPd2. In addition, the appearance of all C_{2+} signals are slightly shifted forward (**Fig. 5.17d**) though increasing at a lower rate compared to CuPd2. It worth noting that the sharp increment of acetaldehyde (red curve) is not observed in CuPd10, which explains the lower C_2 efficiency in CuPd10 (**Fig. 5.5b**).

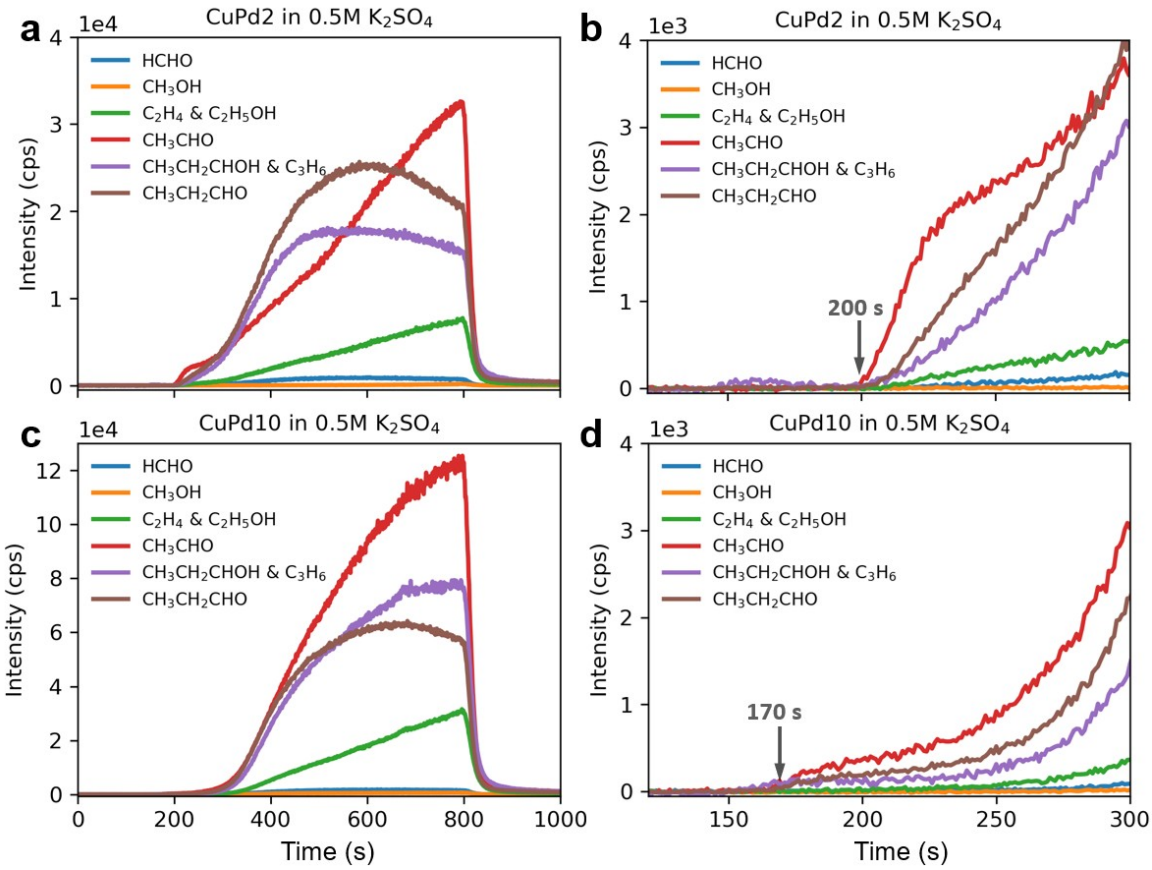


Figure 5.17 C_{2+} products measured from PTR–TOF–MS measurements on **(a)** CuPd2 and **(c)** CuPd10 at a scan rate of 0.15 $mA \cdot s^{-1}$ from 0 to 100 mA. The scan started at 100 s and stopped at 770 s. An enlarged plot at the beginning of the scan is shown for each sample in **(b)** and **(d)** from 100 to 300 s, respectively.

Further investigation on Cu was also conducted to complete the studies. Alkaline electrolyte indeed favours the multi-carbon production to the largest scale with the portion of C_3 being the highest (**Fig. 5.18a**). The fast accumulation of CH_3CHO at the beginning was detected (**Fig. 5.18b**) similar to the CuPd2 sample in neutral electrolyte. In comparison, the neutral electrolyte supresses the C_2 formation with less C_3 molecules detected by the MS and the absence of surging in acetaldehyde (**Fig. 5.18c,d**).

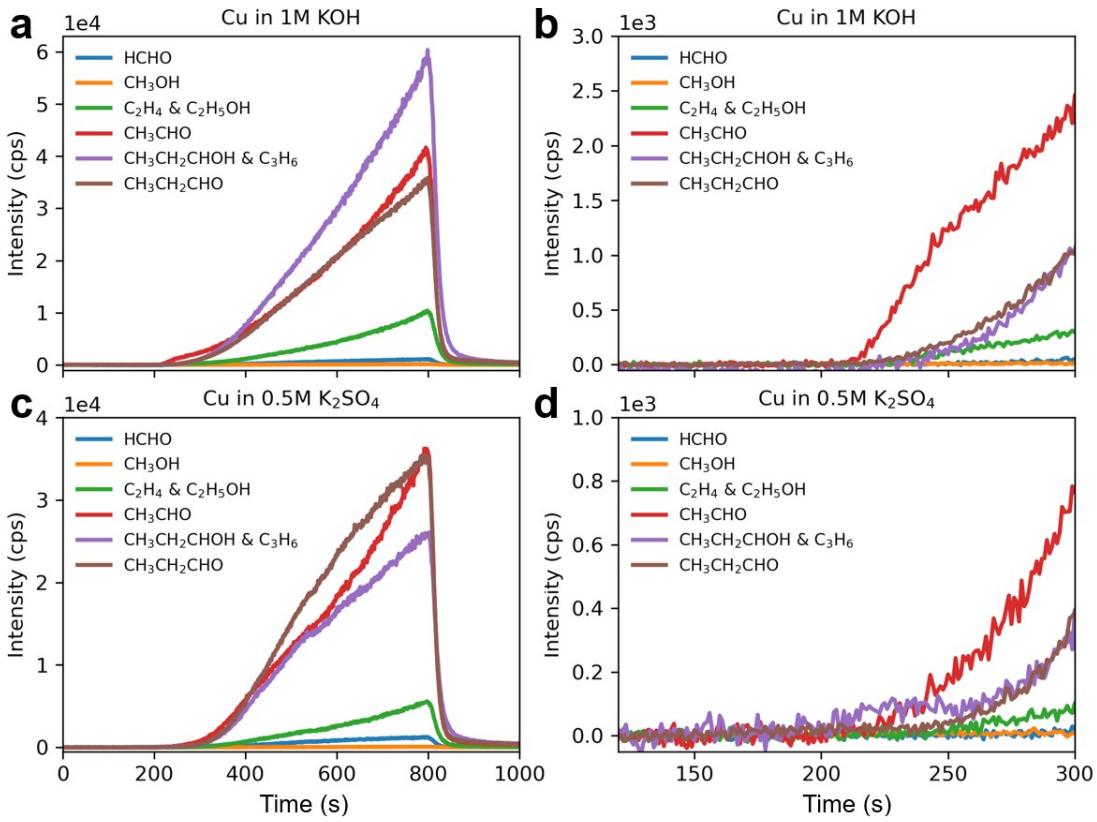


Figure 5.18 C_{2+} products measured from PTR–TOF–MS measurements on Cu in **(a)** 1M KOH and **(c)** 0.5M K_2SO_4 at a scan rate of 0.15 $mA \cdot s^{-1}$ from 0 to 100 mA. The scan started at 100 s and stopped at 770 s. An enlarged plot at the beginning of the scan is shown for each sample in **(b)** and **(d)** from 100 to 300 s, respectively.

5.3 Conclusion

Overall, in Chapter 5, a comprehensive study on Pd-doped Cu particles was carried out. The goal of efficient ethylene production in neutral electrolyte was achieved. Insight of electrocatalysts under reaction conditions was gained through *in-situ* measurements of EIS, XAS and PTR-TOF-MS. It was found that with appropriate amount of Pd-doping had modified the surface properties of Cu particles capable for higher selectivity of ECR versus HER. Such transformation of catalysts was not only reflected in the electrochemical performance but also proved through the change of local environment and the different route of intermediates/products formation.

The Pd doping created a higher double layer capacitance as illustrated by EIS, which led to higher coverage of carbon intermediates. Through the analysis to MS data, it is believed that C-C coupling did not necessarily determine the reaction rate in consistence with the EIS data in which the carbon-related process was located at high-frequency region. The coordination environment of Cu used to be driven into metallic structure soon after the reduction started, yet the doping of Pd introduced defects and unsaturated sites to the surface maintaining the reactivity under high current density.

From the basic characteristics of materials to the advanced techniques for real-time detection, the understanding to the catalysts has been significantly improved. For future studies, there are two possible directions. The first and most straightforward approach is to test CuPd2 with an MEA setup under industrial conditions in neutral electrolyte or pure water. The other direction is to dig into the mechanism to clarify the complicated reaction pathways of C_{2+} on CuPd catalysts with techniques such as DEMS and *in-situ* Raman.

5.4 Reference

1. C.-T. Dinh, T. Burdyny, M. G. Kibria, A. Seifitokaldani, C. M. Gabardo, F. P. García de Arquer, A. Kiani, J. P. Edwards, P. De Luna, O. S. Bushuyev, C. Zou, R. Quintero-Bermudez, Y. Pang, D. Sinton and E. H. Sargent, CO_2 electroreduction to ethylene via hydroxide-mediated copper catalysis at an abrupt interface, *Science*, 2018, **360**, 783-787.
2. W. Ma, S. Xie, T. Liu, Q. Fan, J. Ye, F. Sun, Z. Jiang, Q. Zhang, J. Cheng and Y. Wang, Electrocatalytic reduction of CO_2 to ethylene and ethanol through hydrogen-assisted C–C coupling over fluorine-modified copper, *Nat. Catal.*, 2020, **3**, 478-487.
3. M. Ma, E. L. Clark, K. T. Therkildsen, S. Dalsgaard, I. Chorkendorff and B. Seger, Insights into the carbon balance for CO_2 electroreduction on Cu using gas diffusion electrode reactor designs, *Energy Environ. Sci.*, 2020, **13**, 977-985.
4. U. O. Nwabara, A. D. Hernandez, D. A. Henckel, X. Chen, E. R. Cofell, M. P. De-Heer, S. Verma, A. A. Gewirth and P. J. A. Kenis, Binder-Focused Approaches to

Improve the Stability of Cathodes for CO_2 Electroreduction, *ACS Appl. Energy Mater.*, 2021, **4**, 5175-5186.

5. F. Calle-Vallejo and M. T. M. Koper, Theoretical Considerations on the Electroreduction of CO to C_2 Species on Cu(100) Electrodes, *Angew. Chem. Int. Ed.*, 2013, **52**, 7282-7285.
6. Y. Kim, S. Park, S.-J. Shin, W. Choi, B. K. Min, H. Kim, W. Kim and Y. J. Hwang, Time-resolved observation of C–C coupling intermediates on Cu electrodes for selective electrochemical CO_2 reduction, *Energy Environ. Sci.*, 2020, **13**, 4301-4311.
7. H. Mistry, Y.-W. Choi, A. Bagger, F. Scholten, C. S. Bonifacio, I. Sinev, N. J. Divins, I. Zegkinoglou, H. S. Jeon, K. Kisslinger, E. A. Stach, J. C. Yang, J. Rossmeisl and B. Roldan Cuenya, Enhanced Carbon Dioxide Electroreduction to Carbon Monoxide over Defect-Rich Plasma-Activated Silver Catalysts, *Angew. Chem. Int. Ed.*, 2017, **56**, 11394-11398.
8. Y. Hori, H. Ito, K. Okano, K. Nagasu and S. Sato, Silver-coated ion exchange membrane electrode applied to electrochemical reduction of carbon dioxide, *Electrochim. Acta*, 2003, **48**, 2651-2657.
9. R. G. Mariano, M. Kang, O. J. Wahab, I. J. McPherson, J. A. Rabinowitz, P. R. Unwin and M. W. Kanan, Microstructural origin of locally enhanced CO_2 electroreduction activity on gold, *Nat. Mater.*, 2021, **20**, 1000-1006.
10. M. Liu, Y. Pang, B. Zhang, P. De Luna, O. Voznyy, J. Xu, X. Zheng, C. T. Dinh, F. Fan, C. Cao, F. P. G. de Arquer, T. S. Safaei, A. Mepham, A. Klinkova, E. Kumacheva, T. Filleter, D. Sinton, S. O. Kelley and E. H. Sargent, Enhanced electrocatalytic CO_2 reduction via field-induced reagent concentration, *Nature*, 2016, **537**, 382-386.
11. G. Marcandalli, A. Goyal and M. T. M. Koper, Electrolyte Effects on the Faradaic Efficiency of CO_2 Reduction to CO on a Gold Electrode, *ACS Catal.*, 2021, **11**, 4936-4945.
12. R. G. Mariano, K. McKelvey, H. S. White and M. W. Kanan, Selective increase in CO_2 electroreduction activity at grain-boundary surface terminations, *Science*, 2017, **358**, 1187-1192.
13. H. B. Yang, S.-F. Hung, S. Liu, K. Yuan, S. Miao, L. Zhang, X. Huang, H.-Y. Wang, W. Cai, R. Chen, J. Gao, X. Yang, W. Chen, Y. Huang, H. M. Chen, C. M.

Li, T. Zhang and B. Liu, Atomically dispersed Ni(I) as the active site for electrochemical CO_2 reduction, *Nat. Energy*, 2018, **3**, 140-147.

14. T. Möller, W. Ju, A. Bagger, X. Wang, F. Luo, T. Ngo Thanh, A. S. Varela, J. Rossmeisl and P. Strasser, Efficient CO_2 to CO electrolysis on solid Ni–N–C catalysts at industrial current densities, *Energy Environ. Sci.*, 2019, **12**, 640-647.
15. M. Gong, W. Zhou, M.-C. Tsai, J. Zhou, M. Guan, M.-C. Lin, B. Zhang, Y. Hu, D.-Y. Wang, J. Yang, S. J. Pennycook, B.-J. Hwang and H. Dai, Nanoscale nickel oxide/nickel heterostructures for active hydrogen evolution electrocatalysis, *Nat. Commun.*, 2014, **5**, 4695.
16. J. N. Hansen, H. Prats, K. K. Toudahl, N. Mørch Secher, K. Chan, J. Kibsgaard and I. Chorkendorff, Is There Anything Better than Pt for HER?, *ACS Energy Lett.*, 2021, **6**, 1175-1180.
17. R. J. Bellows, E. P. Marucchi-Soos and D. T. Buckley, Analysis of Reaction Kinetics for Carbon Monoxide and Carbon Dioxide on Polycrystalline Platinum Relative to Fuel Cell Operation, *Ind. Eng. Chem. Res.*, 1996, **35**, 1235-1242.
18. X. Min and M. W. Kanan, Pd-Catalyzed Electrohydrogenation of Carbon Dioxide to Formate: High Mass Activity at Low Overpotential and Identification of the Deactivation Pathway, *J. Am. Chem. Soc.*, 2015, **137**, 4701-4708.
19. R. Kortlever, C. Balemans, Y. Kwon and M. T. M. Koper, Electrochemical CO_2 reduction to formic acid on a Pd-based formic acid oxidation catalyst, *Catal. Today*, 2015, **244**, 58-62.
20. J. Li, K. Xu, F. Liu, Y. Li, Y. Hu, X. Chen, H. Wang, W. Xu, Y. Ni, G. Ding, T. Zhao, M. Yu, W. Xie and F. Cheng, Hollow Hierarchical Cu_2O-Derived Electrocatalysts Steering CO2 Reduction to Multi-Carbon Chemicals at Low Overpotentials, *Adv. Mater.*, 2023, **35**, 2301127.
21. A. A. Permyakova, J. Herranz, M. El Kazzi, J. S. Diercks, M. Povia, L. R. Mangani, M. Horisberger, A. Pătru and T. J. Schmidt, On the Oxidation State of Cu_2O upon Electrochemical CO_2 Reduction: An XPS Study, *ChemPhysChem*, 2019, **20**, 3120-3127.
22. Y. Lum and J. W. Ager, Stability of Residual Oxides in Oxide-Derived Copper Catalysts for Electrochemical CO_2 Reduction Investigated with 18O Labeling, *Angew. Chem. Int. Ed.*, 2018, **57**, 551-554.

23. L. Zhang, J. Feng, S. Liu, X. Tan, L. Wu, S. Jia, L. Xu, X. Ma, X. Song, J. Ma, X. Sun and B. Han, Atomically Dispersed Ni–Cu Catalysts for pH-Universal CO_2 Electroreduction, *Adv. Mater.*, 2023, **35**, 2209590.
24. T. Adit Maark and B. R. K. Nanda, CO and CO_2 Electrochemical Reduction to Methane on Cu, Ni, and Cu_3Ni (211) Surfaces, *J. Phys. Chem. C*, 2016, **120**, 8781-8789.
25. W. Ren, X. Tan, J. Qu, S. Li, J. Li, X. Liu, S. P. Ringer, J. M. Cairney, K. Wang, S. C. Smith and C. Zhao, Isolated copper–tin atomic interfaces tuning electrocatalytic CO_2 conversion, *Nat. Commun.*, 2021, **12**, 1449.
26. E. L. Clark, C. Hahn, T. F. Jaramillo and A. T. Bell, Electrochemical CO_2 Reduction over Compressively Strained CuAg Surface Alloys with Enhanced Multi-Carbon Oxygenate Selectivity, *J. Am. Chem. Soc.*, 2017, **139**, 15848-15857.
27. D. Kim, J. Resasco, Y. Yu, A. M. Asiri and P. Yang, Synergistic geometric and electronic effects for electrochemical reduction of carbon dioxide using gold–copper bimetallic nanoparticles, *Nat. Commun.*, 2014, **5**, 4948.
28. M. B. Ross, C. T. Dinh, Y. Li, D. Kim, P. De Luna, E. H. Sargent and P. Yang, Tunable Cu Enrichment Enables Designer Syngas Electrosynthesis from CO_2, *J. Am. Chem. Soc.*, 2017, **139**, 9359-9363.
29. Z. Weng, X. Zhang, Y. Wu, S. Huo, J. Jiang, W. Liu, G. He, Y. Liang and H. Wang, Self-Cleaning Catalyst Electrodes for Stabilized CO_2 Reduction to Hydrocarbons, *Angew. Chem. Int. Ed.*, 2017, **56**, 13135-13139.
30. Y. Ji, Z. Chen, R. Wei, C. Yang, Y. Wang, J. Xu, H. Zhang, A. Guan, J. Chen, T.-K. Sham, J. Luo, Y. Yang, X. Xu and G. Zheng, Selective CO-to-acetate electroreduction via intermediate adsorption tuning on ordered Cu–Pd sites, *Nat. Catal.*, 2022, **5**, 251-258.
31. E. Westsson, S. Picken and G. Koper, The effect of lattice strain on catalytic activity, *Chem. Commun.*, 2019, **55**, 1338-1341.
32. X. Liu, S. Cui, Z. Sun and P. Du, Robust and highly active copper-based electrocatalyst for hydrogen production at low overpotential in neutral water, *Chem. Commun.*, 2015, **51**, 12954-12957.
33. H. Ren, M. Kovalev, Z. Weng, M. Z. Muhamad, H. Ma, Y. Sheng, L. Sun, J. Wang, S. Rihm, W. Yang, A. A. Lapkin and J. W. Ager, Operando proton-transfer-reaction time-of-flight mass spectrometry of carbon dioxide reduction electrocatalysis, *Nat. Catal.*, 2022, **5**, 1169-1179.

34. X. Chang, J. Li, H. Xiong, H. Zhang, Y. Xu, H. Xiao, Q. Lu and B. Xu, C−C Coupling Is Unlikely to Be the Rate-Determining Step in the Formation of C_{2+} Products in the Copper-Catalyzed Electrochemical Reduction of CO, *Angew. Chem. Int. Ed.*, 2022, **61**, e202111167.

Chapter 6 Conclusions and Outlook

6.1 Conclusions

This thesis explores Cu-based electrocatalysts for CO_2 conversion to various hydrocarbon products to address the influence of metal-support interaction, electrolyte, and doping on the efficiency of electrochemical CO_2 reduction (ECR). Cu-related materials have been the focus in ECR field due to their unique selectivity to multi-carbons (C_{2+}) including methane, ethylene, and alcohols[1]. Combining with traditional heterogenous catalysis, these products can be used as chemicals and feedstocks for industry with lower CO_2 emission. Challenges and opportunities in the industrial chain that hamper the scale-up deployment of the ECR technology have been reviewed by our group and collaborators[2] The bottleneck of this field is the low selectivity towards target molecules and the harsh reaction conditions in high pH electrolytes[3]. Therefore, the objective of the thesis is to demonstrate how catalysts design would benefit the selectivity and efficiency of ECR through microscopic engineering of interface and local environment. Starting with the construction of metal-oxide interfaces, this thesis introduces the interaction between Cu and oxide support during the reaction and illustrates the role of support in CO_2 capture and activation for enhanced methane selectivity. After clarifying the support effects for C_1 production, C_2H_4 is targeted in the studies by exploring the electrode surface process in different electrolytes. While high pH enables higher C_{2+} selection among all carbon products, doping of Pd into Cu achieves comparable C_{2+} selectivity in neutral electrolyte. *In-situ* characterisations confirms the altering of product distribution and supports CuPd as a candidate for efficient CO_2-to-C_{2+} conversion in mild conditions.

Following the introduction of research background and experimental methods in Chapter 1 and 2, respectively, proton-conductive supports are studied with Cu loading in Chapter

3 to deal with proton activation barriers of ECR. MgO is selected as a support for efficient methane production with an optimal copper loading at around 10%. Interface between Cu species and MgO is proved by EPR to assist the accumulation of oxygen vacancies which could act as the active sites of the CO_2-to-CH_4 reaction. Raman reveals that MgO supports attracts carbonates and facilitates C=O bond breakage under applied potentials. It is also confirmed that the MgO support after surface hydration serves as a reservoir of chemically adsorbed carbonates apart from a proton conductor. Drawbacks of the MgO support are also noticed including the short lifetime caused by corrosion/carbonation on the surface. A transient technique, impedance spectra, identify the working states of the electrodes, and a hydrogen related process from HER is captured in the spectra thanks to the unwanted electrode flooding. *In-situ* XAS extracts the coordination environment surrounding the Cu sites which maintain a positive valence state even at −1 V. The synergy of CO_2 activation and $Cu^{\delta+}$ preservation during the reactions guarantee a high methane Faradaic efficiency (FE) of more than 50%.

Chapter 4 digs into the environment influence on Cu catalysts. Supported Cu is discarded to simplify the system and electrode surface, and Cu nanoparticles are sprayed onto the electrode for ECR measurements. Instead of focusing on designing novel materials, this section explored deeper into the external factors of electrolysis process and electrodes. Alkaline and neutral electrolytes are tested to understand the reaction of Cu particles to proton concentrations, and enhancement of ethylene and methane selectivity are found, respectively. Impedance spectroscopy monitoring the electrode process provides clues on the reason of such differences. Alkaline solution with limited proton concentration shows low H^+ coverage and retarded transfer process, while the adsorption of carbon species is less hindered, and the C-C coupling process takes place driven by electric fields. Neutral electrolyte, on the contrary, has sufficient proton supply and therefore, shows a strong

proton-related process that leads to higher CH_4 and H_2 selectivity. Besides the influence generated by electrolytes, air also plays a role in electrode manufacture as Cu is sensitive to air. The Cu particles with smaller grain sizes shows better resistance to oxidation owning to the surface Cu_2O covering, while the calcined Cu with large grain sizes is significantly oxidized during the spray casting process. The incorporation of oxygen atoms into the original Cu lattice may be removed eventually under reducing current, yet their influence on the surface electronic states is huge.

Chapter 5 targets at the C_{2+} selectivity in neutral electrolyte, a more practical study on electrocatalysts for possible industrial applications. The replacement of alkaline electrolyte with neutral one brings new issues on higher proton concentrations. To neutralize the excessive H^+ on the surface that increases the HER efficiency, surface engineering to Cu particles is applied via doping. Pd, as the dopant, has stronger bonding with CO*, which was chosen to assist the ECR over HER. Lattice expansion is induced by Pd insertion as expected and by controlling the doping level, Pd atoms remain in the bulk of Cu particles without aggregation. Selectivity to C_2H_4 is improved to a comparable level to pure Cu in alkaline conditions. Furthermore, operando analysis by mass spectroscopy (MS) confirms the effectiveness of Pd doping by observing faster C_1 formation in response to linear current scans. It is counterintuitive that C_{2-3} products appear earlier than all C_1 molecules and accumulate faster on the surface within the low current density range, which concludes that C-C coupling is unlikely to be the rater-determine step (RDS) of multi-carbon formation in neutral electrolyte. Nevertheless, a high concentration of Pd doping forces Pd atoms to diffuse to the particle surface and overcompensate the adsorption of carbon species, by which methane dominates the ECR products.

Overall, the thesis demonstrates strategies of designing electrocatalysts towards different hydrocarbons and explains the underlying reasons through *in-situ* experiments. It also offers a better understanding of the cathode electrodes under working conditions and applied EIS as a tool to diagnose and identify the flooding that causes deactivation of ECR electrolyser. Combining catalysts designing with the electrochemical cell management brings the development of ECR one step closer to its applications in real life scenarios.

6.2 Outlook

While this thesis has involved some strategies of designing electrocatalysts, the development of nanomaterials never stops and requires more rational thoughts. It can be anticipated that researchers will continue to synthesize catalysts with higher ECR efficiency at lower cost. To achieve this, a wise way is taking the advantage of computational methods. The appearance of artificial intelligence (AI) has been proved to accelerate development in all walks of life. Training the AI model with proper dataset would be a 'shortcut' to reach the final answer of ECR catalysts. There has been an example of combing density functional theory and active machine learning to select a Cu-Al electrocatalysts which was claimed to have the highest CO_2-to-C_2H_4 selectivity[4]. The accuracy of this model still needs examination as recent studies on CuAl nanowires showed that formic acid was preferred instead of ethylene[5]. Nonetheless, the introduction of AI models into an experiments-dominated subject like catalysis would be quite a breakthrough.

However, for further improvement to the overall efficiency of ECR, the real challenges are not lying in the catalyst itself. The design of electrolyser and the manufacture of electrodes all require extra attention with engineering and materials expertise. The current

flow cell setups for ECR are built up based on fuel cell[6]. While it has eliminated mass transportation and avoided static electrolyte in a batch reactor, the flow cell still suffers from many aspects that affect the lifetime of ECR cells including imbalanced pressure between cathode and anode chamber, flooding of cathode and carbonate crossover. Recently, researchers have started to pay attention to these issues by examining various flow cell configurations as well as adaptions to the membrane structures. Using pure water as catholyte could be one of the promising solutions to circumvent carbonate formation and crossover, and a good ethylene efficiency was achieved at the ampere level[7]. Additionally, replacing CO_2 with CO as the reactant could also be a strategy to tackle with the low conversion issue. Integrating a solid oxide electrochemical cell (SOEC) to first decompose CO_2 into CO with the aqueous electrochemical CO reduction reactions was also proved to be a viable alternative[182]. Besides the ECR reactions, the polymer membrane that separates the electrodes and provides ion conductivity is of great significance to the operation of CO_2 electrolysers. Functionalization to the existing Nafion® and Sustanion® ionomers or designing new ion conductive polymers is a challenging issue to tackle with[9].

Based on the common goal of decarbonisation, the conversion of CO_2 into valuable chemicals and fuels driven by renewable electricity is bound to be a promising solution for a cleaner and better future.

6.3 Reference

1. A. A. Peterson, F. Abild-Pedersen, F. Studt, J. Rossmeisl and J. K. Nørskov, How copper catalyzes the electroreduction of carbon dioxide into hydrocarbon fuels, *Energy Environ. Sci.*, 2010, **3**, 1311-1315.
2. X. She, Y. Wang, H. Xu, S. Chi Edman Tsang and S. Ping Lau, Challenges and Opportunities in Electrocatalytic CO_2 Reduction to Chemicals and Fuels, *Angew. Chem. Int. Ed.*, 2022, **61**, e202211396.

3. C.-T. Dinh, T. Burdyny, M. G. Kibria, A. Seifitokaldani, C. M. Gabardo, F. P. García de Arquer, A. Kiani, J. P. Edwards, P. De Luna, O. S. Bushuyev, C. Zou, R. Quintero-Bermudez, Y. Pang, D. Sinton and E. H. Sargent, CO_2 electroreduction to ethylene via hydroxide-mediated copper catalysis at an abrupt interface, *Science*, 2018, **360**, 783-787.
4. M. Zhong, K. Tran, Y. Min, C. Wang, Z. Wang, C.-T. Dinh, P. De Luna, Z. Yu, A. S. Rasouli, P. Brodersen, S. Sun, O. Voznyy, C.-S. Tan, M. Askerka, F. Che, M. Liu, A. Seifitokaldani, Y. Pang, S.-C. Lo, A. Ip, Z. Ulissi and E. H. Sargent, Accelerated discovery of CO_2 electrocatalysts using active machine learning, *Nature*, 2020, **581**, 178-183.
5. I. M. Badawy, G. E. Khedr, A. Hafez, E. A. Ashour and N. K. Allam, Boosting selectivity towards formate production using CuAl alloy nanowires by altering the CO_2 reduction reaction pathway, *Chem. Commun.*, 2023, **59**, 7974-7977.
6. C. Delacourt, P. L. Ridgway, J. B. Kerr and J. Newman, Design of an Electrochemical Cell Making Syngas ($CO + H_2$) from CO_2 and H_2O Reduction at Room Temperature, *J. Electrochem. Soc.*, 2008, **155**, B42.
7. W. Li, Z. Yin, Z. Gao, G. Wang, Z. Li, F. Wei, X. Wei, H. Peng, X. Hu, L. Xiao, J. Lu and L. Zhuang, Bifunctional ionomers for efficient co-electrolysis of CO_2 and pure water towards ethylene production at industrial-scale current densities, *Nat. Energy*, 2022, **7**, 835-843.
8. A. Ozden, Y. Wang, F. Li, M. Luo, J. Sisler, A. Thevenon, A. Rosas-Hernández, T. Burdyny, Y. Lum, H. Yadegari, T. Agapie, J. C. Peters, E. H. Sargent and D. Sinton, Cascade CO_2 electroreduction enables efficient carbonate-free production of ethylene, *Joule*, 2021, **5**, 706-719.
9. R. B. Kutz, Q. Chen, H. Yang, S. D. Sajjad, Z. Liu and I. R. Masel, Sustainion Imidazolium-Functionalized Polymers for Carbon Dioxide Electrolysis, *Energy Technol.*, 2017, **5**, 929-936.

Appendix

I. Appendix Tables

Table A1. FE of CO_2-to-CH_4 from literatures over the recent years.

Catalysts	FE_{CH4} (%)	Total current ($mA \cdot cm^{-2}$)	Potential (V_{RHE})	Electrolyte	Cell type	Ref.
Cu-MgO	53	400	-1.15	1 M KOH	Flow cell (2 gap)	Chapter 3
Cu-supported Fe SAC	64	200	-1.1	1 M $KHCO_3$	Flow cell (2 gap)	[1]
Cu-Ce-O_x	67.8	200	-0.82	1 M KOH	Flow cell (2 gap)	[2]
Carbon NPs confined CuPc	62	220	-4 (full cell)	N/A	Flow cell (0 gap)	[3]
Cu_3Pd_xN nanocrystals	57.5	20	-1.25	0.5 M $KHCO_3$	H-cell	[4]
Nafion-modified Cu	88	2.5	-0.38	0.1 M $NaHCO_3$	One chamber cell	[5*]
200 nm sputtered Cu	48	120	-0.98	0.1 M $NaHCO_3$	Flow cell	[6]
$Cu_{68}Ag_{32}$	60	50	-1.17	0.5M $KHCO_3$	H-cell	[7]
Cu NPs from Cu MOF-74	50	10	-1.3	0.1 M $KHCO_3$	One chamber cell	[8]
Polydopamine-Cu nanowires	29	60	-0.93	1 M $NaHCO_3$	H-cell	[9]
Copper-porphyrin complex	27	15	-0.976	0.5 M $KHCO_3$	H-cell	[10]

* Low data reliability due to the extremely low current density.

Table A2. Atomic force microscope (AFM) measured thickness data.

Sample	Thickness (average of 5 measurements)/nm	Standard Deviation (of 5 measurements)/nm
MgO	91.23	78.18
$Mg(OH)_2$	105.92	72.20

II. Appendix Figures

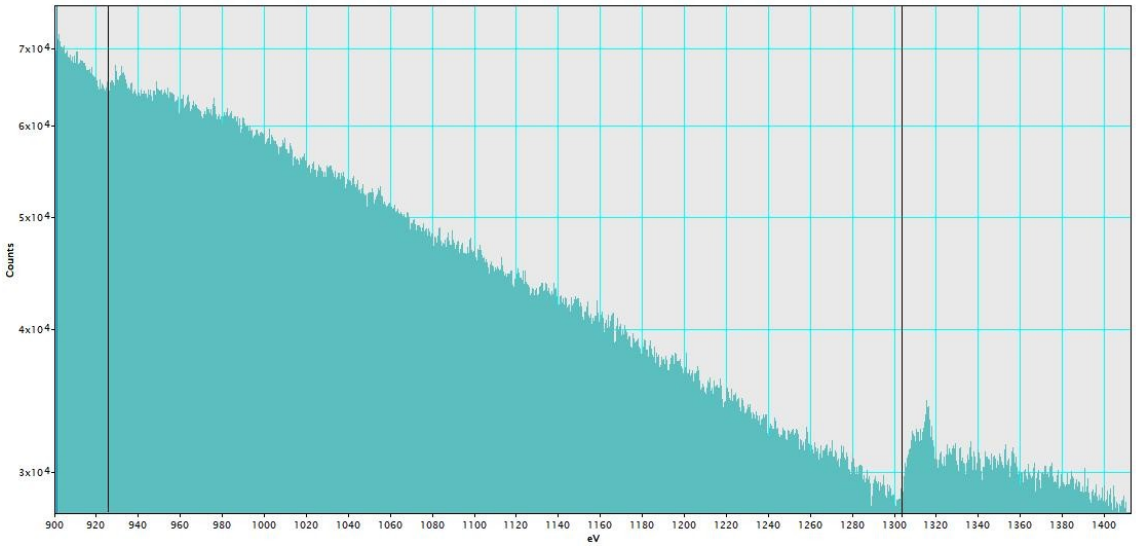


Figure A1. EELS of Cu-$Mg(OH)_2$ with the black line marking L-edge of Cu at around 931 eV and K-edge of Mg at around 1305 eV. Thickness of sample derived by mean-free-path is 98 nm.

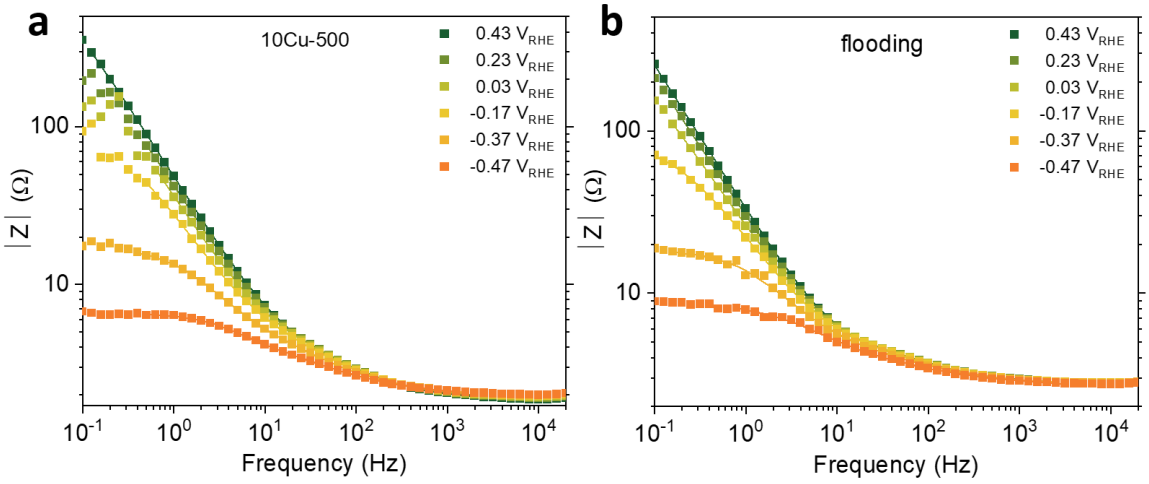


Figure A2. Bode plot with total impedance Z of sample 10Cu-500 **(a)** under normal working condition and **(b)** under flooding condition.

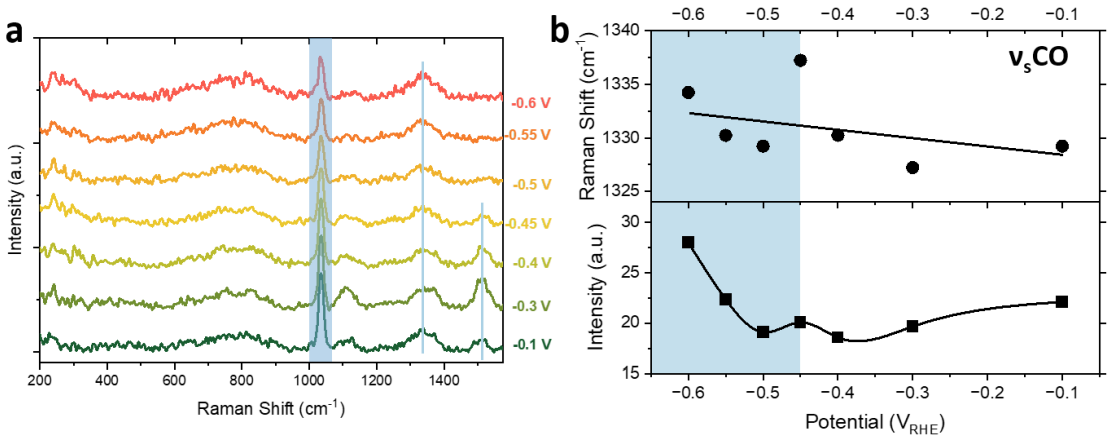


Figure A3. (a) Full Raman spectrum; **(b)** symmetric stretching of C-O.

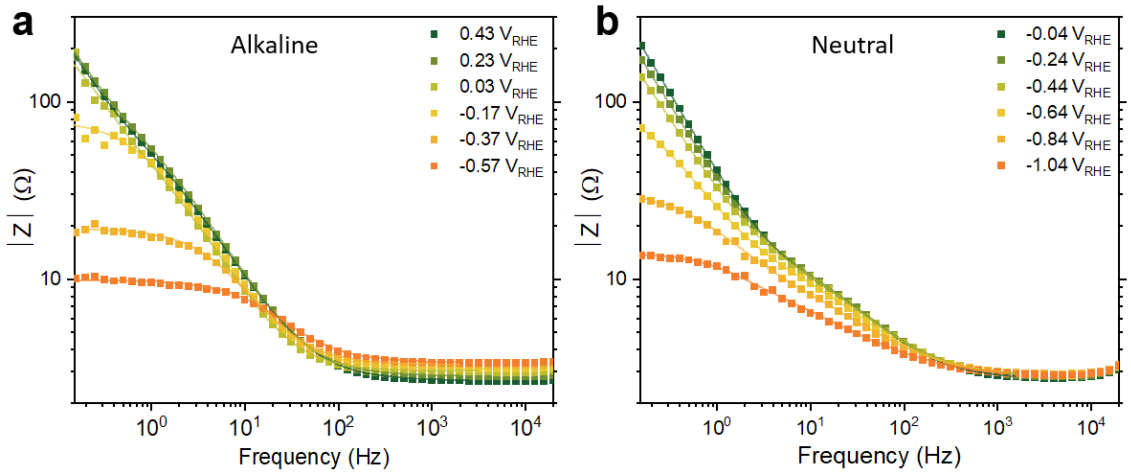


Figure A4. Bode plot with total impedance Z of Cu particle **(a)** in 1M KOH electrolyte and **(b)** in 0.5M K_2SO_4 electrolyte.

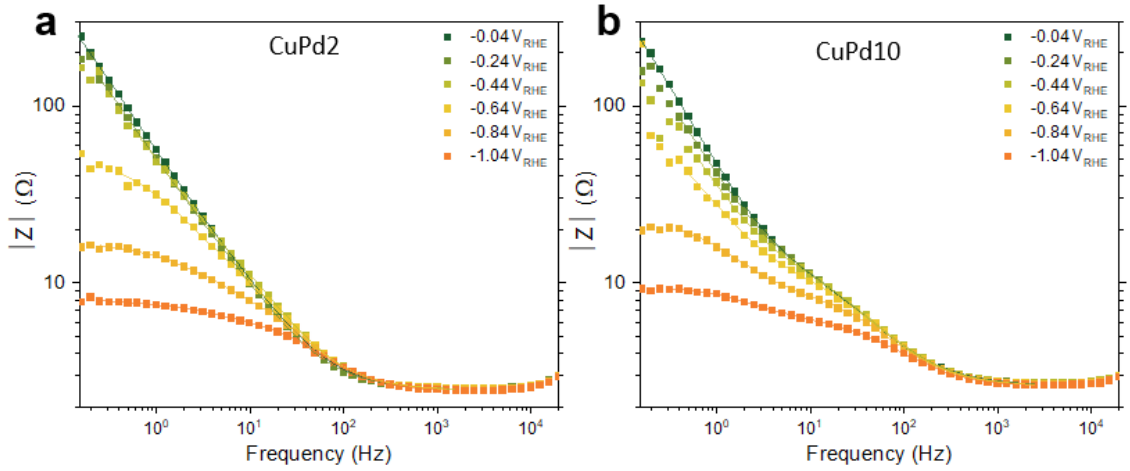


Figure A5. Bode plot with total impedance Z of **(a)** CuPd2 and **(b)** CuPd10 samples.

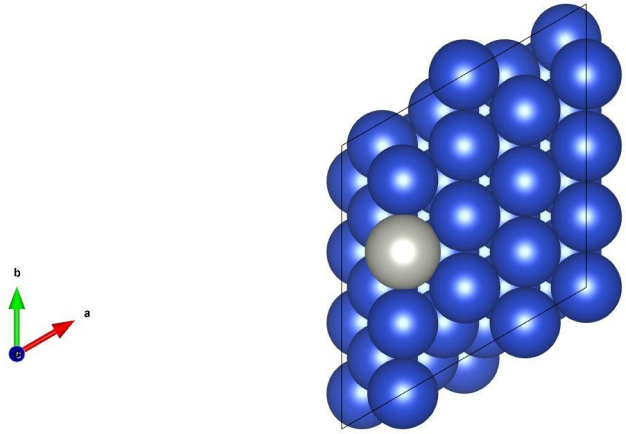


Figure A6. Pd on Cu(111) surface model for EXAFS first-shell fitting.

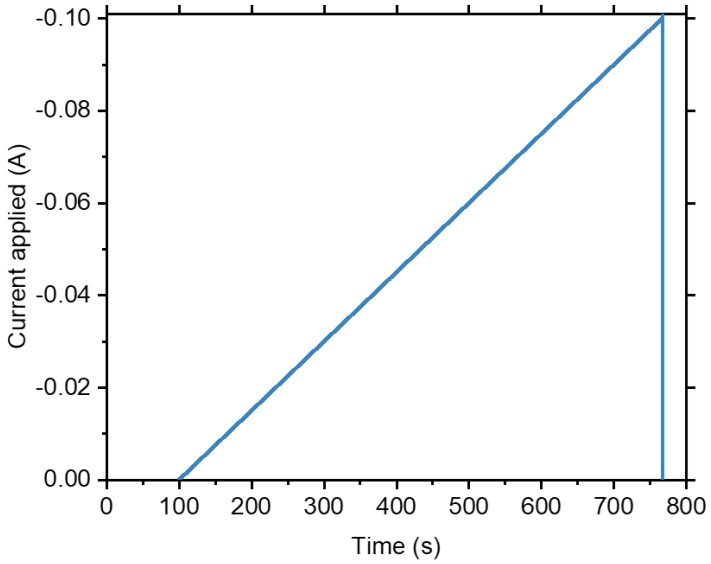


Figure A7. Linear current scan method: current applied as a function of time on the WE at a rate of 0.15 $mA \cdot s^{-1}$ for PTR-TOF-MS measurements.

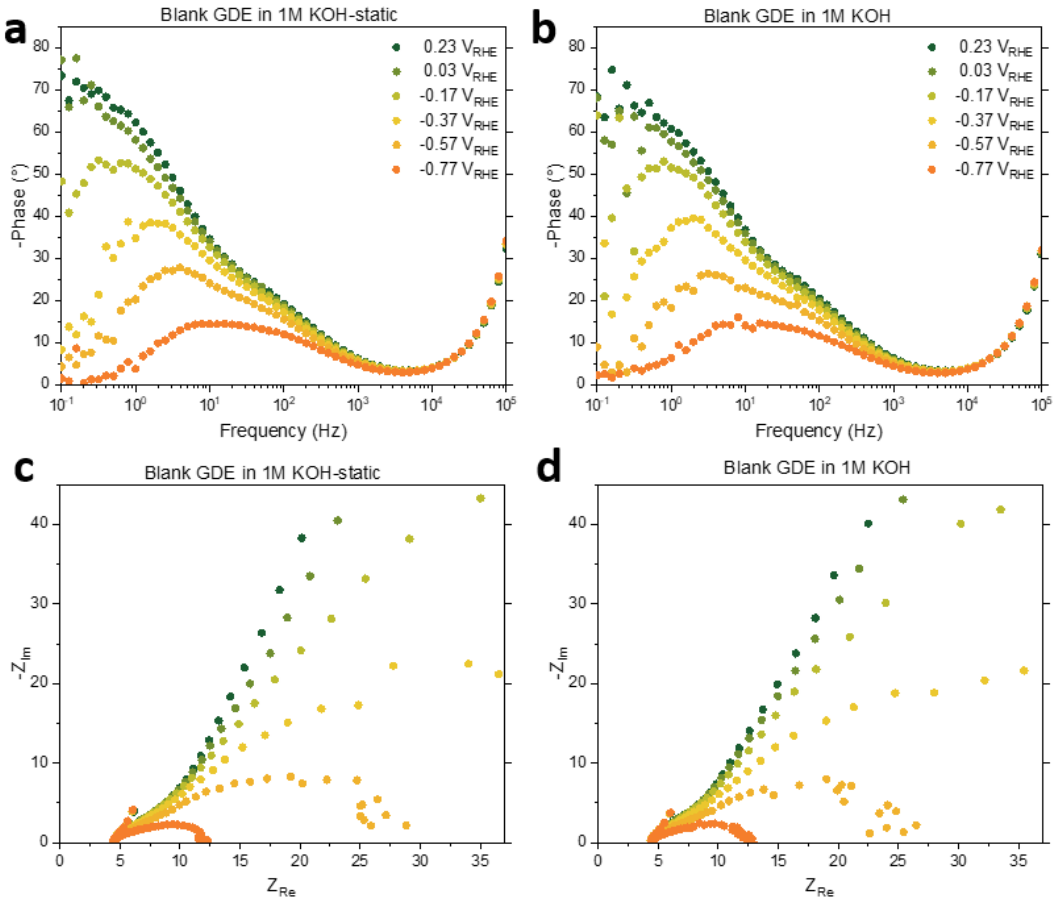


Figure A8. EIS of Blank GDE**.** Bode plot in **(a)** static KOH electrolyte, **(b)** constant flow of KOH electrolyte; Nyquist plot in **(c)** static KOH electrolyte, **(d)** constant flow of KOH electrolyte.

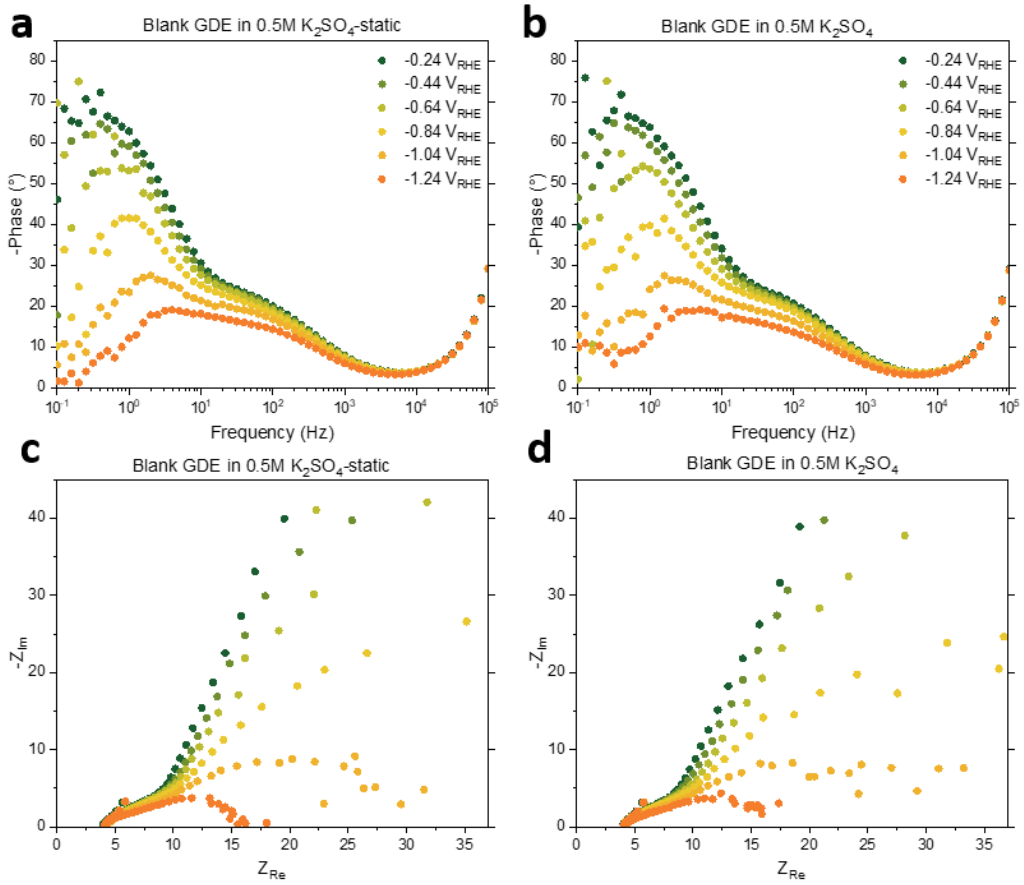


Figure A9. EIS of Blank GDE**.** Bode plot in **(a)** static K_2SO_4 electrolyte, **(b)** constant flow of K_2SO_4 electrolyte; Nyquist plot in **(c)** static K_2SO_4 electrolyte, **(d)** constant flow of K_2SO_4 electrolyte.

Estimation of systematic CO_2 loss in cathode chamber:

Taking ethylene as the example, for each ethylene molecule produced:

Alkaline electrolyte:

$$2CO_2 + 8H_2O + 12e^- \rightarrow C_2H_4 + 12OH^-$$

Hydroxide ions from last equation stay in cathode side:

$$OH^- + CO_2 \rightarrow HCO_3^-$$

$$HCO_3^- + OH^- \rightleftharpoons CO_3^{2-} + H_2O$$

Each CO_2 molecule reacts with at most two OH^- ions. Therefore, for the OH^- ions produced simultaneously with one ethylene molecule, at least 6 CO_2 molecules will be

consumed by them. In total, only 2 out of 8 CO_2 molecules take part in the reduction to ethylene and ¾ CO_2 will be consumed by hydroxide ions.

III. Reference

1. S.-F. Hung, A. Xu, X. Wang, F. Li, S.-H. Hsu, Y. Li, J. Wicks, E. G. Cervantes, A. S. Rasouli, Y. C. Li, M. Luo, D.-H. Nam, N. Wang, T. Peng, Y. Yan, G. Lee and E. H. Sargent, A metal-supported single-atom catalytic site enables carbon dioxide hydrogenation, *Nat. Commun.*, 2022, **13**, 819.
2. X. Zhou, J. Shan, L. Chen, B. Y. Xia, T. Ling, J. Duan, Y. Jiao, Y. Zheng and S.-Z. Qiao, Stabilizing Cu2+ Ions by Solid Solutions to Promote CO_2 Electroreduction to Methane, *J. Am. Chem. Soc.*, 2022, **144**, 2079-2084.
3. Y. Xu, F. Li, A. Xu, J. P. Edwards, S.-F. Hung, C. M. Gabardo, C. P. O'Brien, S. Liu, X. Wang, Y. Li, J. Wicks, R. K. Miao, Y. Liu, J. Li, J. E. Huang, J. Abed, Y. Wang, E. H. Sargent and D. Sinton, Low coordination number copper catalysts for electrochemical CO_2 methanation in a membrane electrode assembly, *Nat. Commun.*, 2021, **12**, 2932.
4. T. Li, J. Wang, S. Zhu, E. P. Delmo, F. Sun, L. Zhang, M. Gu and M. Shao, Cu3PdxN nanocrystals for efficient CO_2 electrochemical reduction to methane, *Electrochim. Acta*, 2021, **371**, 137793.
5. H. Pan and C. J. Barile, Electrochemical CO_2 reduction to methane with remarkably high Faradaic efficiency in the presence of a proton permeable membrane, *Energy Environ. Sci.*, 2020, **13**, 3567-3578.
6. A. Sedighian Rasouli, X. Wang, J. Wicks, G. Lee, T. Peng, F. Li, C. McCallum, C.-T. Dinh, A. H. Ip, D. Sinton and E. H. Sargent, CO_2 Electroreduction to Methane at Production Rates Exceeding 100 mA/cm2, *ACS Sustain. Chem. Eng.*, 2020, **8**, 14668-14673.
7. C.-J. Chang, S.-C. Lin, H.-C. Chen, J. Wang, K. J. Zheng, Y. Zhu and H. M. Chen, Dynamic Reoxidation/Reduction-Driven Atomic Interdiffusion for Highly Selective CO_2 Reduction toward Methane, *J. Am. Chem. Soc.*, 2020, **142**, 12119-12132.
8. M. K. Kim, H. J. Kim, H. Lim, Y. Kwon and H. M. Jeong, Metal–organic framework-mediated strategy for enhanced methane production on copper

nanoparticles in electrochemical CO_2 reduction, *Electrochim. Acta*, 2019, **306**, 28-34.

9. H. Liu, K. Xiang, Y. Liu, F. Zhu, M. Zou, X. Yan and L. Chai, Polydopamine Functionalized Cu Nanowires for Enhanced CO_2 Electroreduction Towards Methane, *ChemElectroChem*, 2018, **5**, 3991-3999.
10. Z. Weng, J. Jiang, Y. Wu, Z. Wu, X. Guo, K. L. Materna, W. Liu, V. S. Batista, G. W. Brudvig and H. Wang, Electrochemical CO_2 Reduction to Hydrocarbons on a Heterogeneous Molecular Cu Catalyst in Aqueous Solution, *J. Am. Chem. Soc.*, 2016, **138**, 8076-8079.